Integrated Nanoscale Tools for Interrogating Living Cells

Integrated Nanoscale Tools for Interrogating Living Cells

A dissertation presented

by

Marsela Jorgolli

to

The Department of Physics
in partial fulfillment of the requirements
for the degree of
Doctor of Philosophy
in the subject of
Physics

Harvard University
Cambridge, Massachusetts
May 2015

Dissertation Advisor:
Prof. Hongkun Park

Author
Marsela Jorgolli

Integrated Nanoscale Tools for Interrogating Living Cells

Abstract

The development of next-generation, nanoscale technologies that interface biological systems will pave the way towards new understanding of such complex systems. Nanowires – one-dimensional nanoscale structures – have shown unique potential as an ideal physical interface to biological systems. Herein, we focus on the development of nanowire-based devices that can enable a wide variety of biological studies. First, we built upon standard nanofabrication techniques to optimize nanowire devices, resulting in perfectly ordered arrays of both opaque (Silicon) and transparent (Silicon dioxide) nanowires with user defined structural profile, densities, and overall patterns, as well as high sample consistency and large scale production. The high-precision and well-controlled fabrication method in conjunction with additional technologies laid the foundation for the generation of highly specialized platforms for imaging, electrochemical interrogation, and molecular biology.

Next, we utilized nanowires as the fundamental structure in the development of integrated nanoelectronic platforms to directly interrogate the electrical activity of biological systems. Initially, we generated a scalable intracellular electrode platform based on vertical nanowires that allows for parallel electrical interfacing to multiple mammalian neurons. Our prototype device consisted of 16 individually addressable stimulation/recording sites, each

containing an array of 9 electrically active silicon nanowires. We showed that these vertical nanowire electrode arrays could intracellularly record and stimulate neuronal activity in dissociated cultures of rat cortical neurons similar to patch clamp electrodes. In addition, we used our intracellular electrode platform to measure multiple individual synaptic connections, which enables the reconstruction of the functional connectivity maps of neuronal circuits.

In order to expand and improve the capability of this functional prototype device we designed and fabricated a new hybrid chip that combines a front-side nanowire-based interface for neuronal recording with backside complementary metal oxide semiconductor (CMOS) circuits for on-chip multiplexing, voltage control for stimulation, signal amplification, and signal processing. Individual chips contain 1024 stimulation/recording sites enabling large-scale interfacing of neuronal networks with single cell resolution. Through electrical and electrochemical characterization of the devices, we demonstrated their enhanced functionality at a massively parallel scale. In our initial cell experiments, we achieved intracellular stimulations and recordings of changes in the membrane potential in a variety of cells including: HEK293T, cardiomyocytes, and rat cortical neurons. This demonstrated the device capability for single-cell-resolution recording/stimulation which when extended to a large number of neurons in a massively parallel fashion will enable the functional mapping of a complex neuronal network.

Table of Contents

Appendix A: Vertical Nanowire Electrode Arrays for Stimulating and Measuring the Activities of Multiple Mammalian Neurons

Citations to Previously Published Work

Chapter 2 draws partly from two works:

"Vertical silicon nanowires as a universal platform for delivering biomolecules into living cells," A. Shalek, J. T. Robinson, E. S. Karp, J. S. Lee, D-R. Ahn, M-H. Yoon, A. Sutton, M. Jorgolli, R. S. Gertner, T. S. Gujral, G. MacBeath, E. G. Yang, H. Park *Proc. Natl. Acad. Sci. USA* **107**, 1870-1875 (2010).

"Dynamic regulatory network controlling Th17 cell differentiation," N. Yosef, A. K. Shalek, J. T. Gaublomme, H. Jin, Y. Lee, A.Awasthi, C. Wu, K. Karwacz, S. Xiao, M. Jorgolli, D. Gennert, R. Satija, A. Shakya, D. Y. Lu, J. T. Trombetta, M. Pillai, P. J. Ratcliffe, M. L. Coleman, M. Bix, D. Tantin, H. Park, V. K. Kuchroo, A. Regev *Nature* **496,** 461-468 (2013).

Chapter 3 has been published with minor changes as:

"Vertical nanowire electrode arrays as a scalable platform for intracellular interfacing to neuronal circuits," J. T. Robinson*, M. Jorgolli*, A. K. Shalek, M-H. Yoon, R. S. Gertner, H. Park *Nature Nanotech.* **7**, 180-184 (2012).

Chapter 4 draws partly from:

"CMOS-assisted 32 x 32 vertical nanowire electrode array for intracellular recording and stimulation," J. Abbott, L. Qin, M. Jorgolli, T. Ye, R. S. Gertner, H. Park, D. Ham submitted (2015).

Appendix A draws partly from:

"Nanowire electrodes for high-density stimulation and measurement of neural circuits," J. T. Robinson, M. Jorgolli, H. Park *Front. Neural Circuits* **7**, 38 (2013)

Acknowledgements

I am extremely grateful to have had the opportunity to pursue my interests, and would like to take this opportunity to thank all of those who have made this possible. First and foremost, I would like to deeply thank my advisor, Hongkun Park, for putting faith in me, affording me so many opportunities, and supporting my research. Hongkun, I have greatly benefited from your support and advice both scientifically and personally.

I want to extend a profound thank you to the other members of my thesis committee, Adam Cohen and Vinothan Manoharan. Your continuing support, advice, and assistance have made my scientific journey a truly inspiring one. I have truly enjoyed learning with and from you, and appreciate everything that you both have done to help me reach this day. I would also like to thank Sheila Ferguson, Lisa Cacciabaudo, and Jacob Barandes for their amazing support and help in more issues that I thought I had.

To all the members of the Park Lab, from the past and the present, I have sincerely enjoyed interacting with you and greatly appreciate your willingness to help me in so many different ways. First, I would like to thank Alex Shalek, who got me excited about joining the lab, taught to me his amazing skill set, and showed me that everything is doable. To Rona Gertner, my go to person for any question and need of help in biology, special thanks for helping me achieve more, by what you have done to help me get to where I am today, both scientifically and personally through my entire PhD experience. Jacob Robinson, I can't thank you enough, it was a pleasure to work by your side and learn a lot from you. To Youngbin Lim, it was a pleasure to perform research with you, but most importantly it was lots of fun learning Korean from you while teaching Albanian to you. Jiwon Kim, having you around has made everything more pleasurable and the lab prettier. It has been a privilege. Tianyang (Yale) Ye, many thanks

for being a great companion during these last steps of mine. I have truly enjoyed your outstanding collaborative approach, unbelievable excitement, and amazingly hard work. And to everyone else in the Park lab: Alex Sushkov, Jellert, Gaublomme,Jeff Creson, Myung-Han Yoon, Alan Dibos, Nathalie de Leon, Chun Yu, Alex High, Mingzhao Liu, Joseph Park, Mark Polking, Jin Seok Lee, Ruihua Ding, Rob Devlin, Peggy Lo, and Minako Kubo – I greatly value your efforts, advice, and help that made every problem solvable.

Additionally, I would like to acknowledge and thank you my collaborators and mentors, who have made possible for me to experience a wide variety of directions and approaches. Overall, they enabled the progress and improvement of my research: Ling Qin, Jeffrey Abbott, Donhee Ham, Jorg Scholvin, Ed Boyden, Sara A. Jones, Guisheng Zhong, Geoff Lau, Venkatesh Murthy, Sebastian Seung, Mark Tobenking, and Russ Tedrake. Many thanks for helping me extend my horizons into different fields.

To the experts in nano- and micro-fabrication techniques, I have sincerely enjoyed interacting with you and learning from you. Brent Buchine, special thanks for helping me to achieve more, more quickly and more enjoyably, than I thought possible. To the entire Harvard cleanroom team: Jiangdong Deng, Yuan Lu, Ed Macomber, Steve Paolini, Ling Xie, Mac Hathaway, John Tsakirgis, Jason Tresback, Guixiong Zhong, Steve Hickman, Philippe de Rouffignac, Adam Graham, Dave Lange, Andrew Mayar – thank you for making my long hours in your three story underground building enjoyable and effective. Also, I would like to thank the team member of the Lurie Nanofabrication Facility at the University of Michigan and Cornell NanoScale Science & Technology Facility: Brian Vanderelzen, Robert Hower, Sandrine Martin, Katharine Beach, Kevin Owen, Noah Clay, Garry J. Bordonaro and Rob Ilic.

I would also like to thank my friends for their love and support. Amy Sutton – thank you for everything, you have been my closest companion both in my day to day research as well as my personal life. Having you by my side has helped me in every challenge that I had to overcome besides making me enjoy more the pleasurable moments. Amanda, Koli, Albana, Gjergji, Ershela, Bianka, Klodi, Lika,Lori, Mira, Redi, Matilda, and Renas thank you for making possible the amazing fun times we have had together and for being excited on my research to force me to discuss it in lay terms, which is really a challenge. I hope that after many trials I was able to get it across to you guys.

Finally, I would like to thank my family for their love and support. Xhaxhi Shpetim, Sonila, Dionis, Janet, Nicholas, and Stela – thank you for believing in me and supporting me in every imaginable way. I was lucky to have you all by my side giving me courage to moving forward and achieve the end that seemed too far away. Xhaxhi Shpetim, I'm glad that I followed your path as a physicist and approached your outstanding level to the point that we can discuss science as well as life goals together. Gjyshi Koci, thank you for convincing me that everything is possible in any country. Moka ime, I am grateful to have had you next to me in every moment of my life, every commencement and celebration, as well as being there to provide me with all the support and help that I needed to overcome challenges. Ronka, Anka, and Lina – sharing my academic career with you and getting your encouragement to move forward, has been incredibly valuable. Mamka, Bucko, and Nandke, how do I even begin to express my gratitude? Thanks for backing me in all of my pursuits, tirelessly being there for me, and for always being my true home. I'm indebted to you for insisting that I pursue my passion and making the biggest sacrifice of your life to make it possible for me. Bucko, I am proud every moment when I say that I'm like my dad and it is him that has inspired me in every step of my way. Sharing with you first my

challenges and my achievements is what gives me the greatest pleasure. Genci – Zemra Ime – I cannot express my depth of gratitude. Nothing would have been possible without you in my life. Thanks for putting up with my odd hours; giving me advice even when I didn't want to hear it (please continue to do so but at a lower frequency); and putting everything together for me without complaining. Your laughs and hugs make my life complete and everything possible. Thank you for making this period of my life truly enjoyable – and looking forward to do the same in every step we take together in the future. I love you!

To my family

CHAPTER 1

Designing and Developing Complex, Integrated, and Biocompatible Platforms for Studying and Manipulating Biological Systems

1.1 Overview

The function of complex biological systems is an emergent property based on the coordinated activity of large numbers of cells. To date, one of the main open questions in biomedicine is how these individual cells work together to perform system-level functions. Although there have been numerous approaches to address this question, a complete understanding and explanation still remains to be discovered. For example, in the immune system cellular heterogeneity and cell-to-cell communication drive ensemble-level decision-

making is poorly understood, despite extended attempts to uncover these principles. Furthermore, no general theory that describes how individual brain cells and complex neural circuits interact to give rise to brain function has been discovered. Advances in the understanding of such complex biological systems, including immunological systems and neuronal circuits, critically depends on the development of new technologies that would enable studies of the dynamics of individual cell activities as well as integrated communications at the network level.

General platforms for high throughput interrogation of cells have the potential to transform how intra- and inter-cellular processes are studied. Nanomaterials and nanostructures are ideal candidates to form the basis of such technologies because of their sub-cellular dimensions. In particular, vertical nanowires (NWs) stand out for their ability to penetrate the cellular membrane in a minimally invasive fashion and hence provide a multiplexed chemical and electrical interface to the cell's interior. Previous studies have demonstrated that cells cultured on NWs grow and divide over a period of weeks despite penetration. Reverse transcription polymerase chain reaction (RT-PCR) analyses of NW-penetrated human fibroblast cells (also obtained for HeLa S3 cells and rat hippocampal neurons) show that transcripts levels of common housekeeping genes are similar to cells cultured on either black silicon or standard multiwell plates (Fig. 1.1 b). Moreover, as shown in Fig. 1.1 d, NW-penetrated rat hippocampal and cortical neurons after several days in culture display typical electrophysiological signatures when patch-clamped, thus demonstrating the NW potential to be utilized as the building blocks of novel nanoscale technologies.

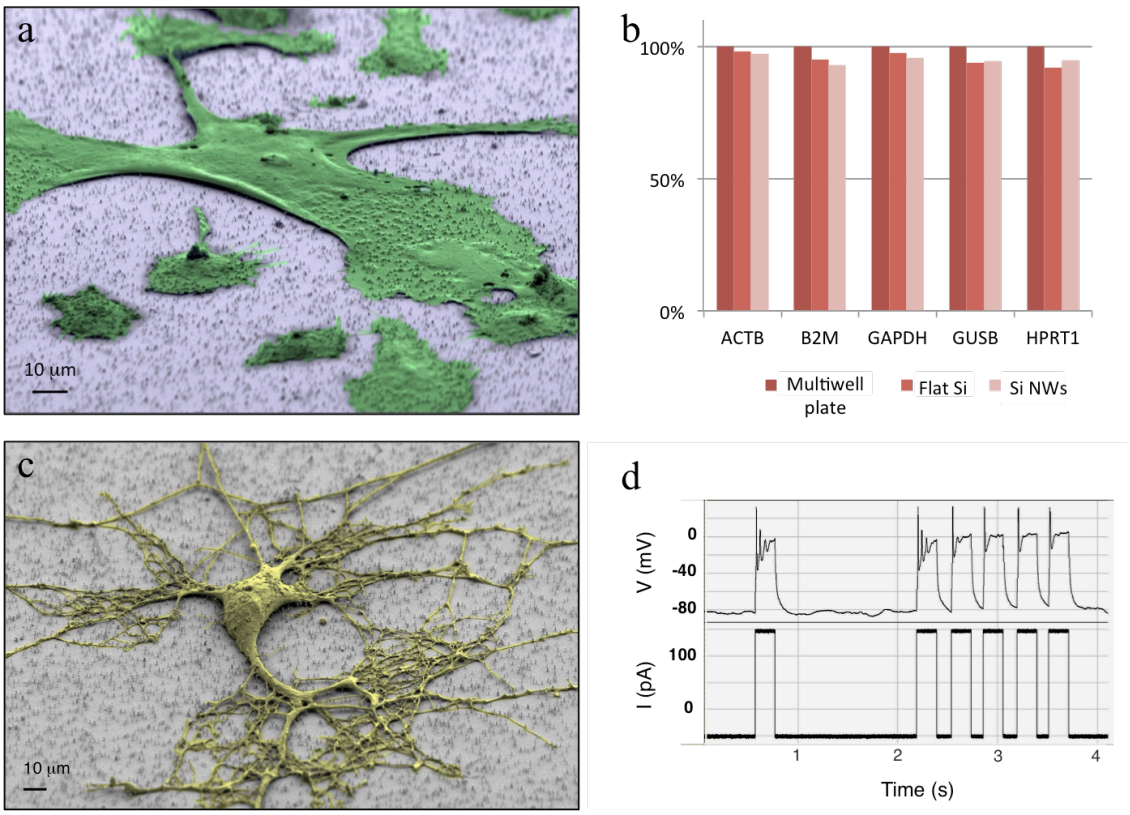

Figure 1.1 | Cells are healthy, despite nanowire penetration. (a) Cells cultured on NWs grow and divide over a period of weeks. SEM shows Human Fibroblasts 1 day after plating. (b) RT-PCR analysis of NW-penetrated cells show that transcript levels of common housekeeping genes are similar to cells cultured on either blank silicon or multiwell plates. (c) Rat hippocampal neurons develop normally on top of NWs, even without the addition of adhesion layer. SEM shows neuron at 7 DIV. (d) After 6 days in culture, NW-penetrated rat hippocampal and cortical neurons display typical electrophysiological signature when patched with a glass micropipette.

The goal of the research described in this dissertation has been to leverage advances in nano- and micro-technology to develop broadly applicable platforms based on nanowire structures for studying and manipulating complex biological systems, particularly neuronal networks. Chapter 2 focuses on our development of novel methods to fabricate perfectly ordered arrays of vertical, opaque or transparent NWs with user defined height, diameter, profile, density, and overall pattern. This well-controlled method enabled the fabrication of NWs with physical dimensions and spacing for optimal delivery to and chemical manipulation of non-adherent primary immune cells such as B-cells and T-cells, which cannot be effectively perturbed with

standard methodologies. Furthermore, the scalability and parallelism associated with these fabrication technologies in combination with the ability to generate compact assay spots can reduce reagent and cell requirements and in turn enable a series of efficient and effective high-throughput screens (e.g., small molecule libraries, genome wide siRNAs, etc.), even with limited numbers of cells and scarce reagents. Besides their utilization for effective chemical perturbations for basic molecular biological studies (e.g., assessing the functional consequences of knocking down a specific gene) and medical applications (e.g., testing the efficacy of a pharmaceutical agent), we have shown their potential for several additional applications. In the next section, we briefly describe the use of nanowire arrays for (1) high-throughput intracellular molecular delivery integrated with super resolution imaging and (2) nanowire-nanodiamond integrated sensors for high-resolution measurements of electrical signals.

Having demonstrated the utility of advanced nanofabrication methodologies to generate highly controllable and effective cell-interfacing platforms, we directed our efforts towards the development of electrically addressable NWs. Chapter 3 and Appendix A depict how this approach allowed us to develop vertical nanowire electrode arrays (VNEA), a step towards a scalable neuro-electronic interface that enables measurement and stimulation of multiple neurons in a massively parallel fashion. Here, we present the device preparation, including system setup and neuronal culture, and describe how the VNEA can be used for intracellular stimulation/recording of neuronal activity. We also describe the characterization of the VNE-cell interface and the two recording modes (Faradaic and capacitive) of this intracellular electrode platform. Furthermore, to illustrate the potential of the multiplexed stimulation and recording capabilities of the VNEA platform and its compatibility with conventional patch-clamp and fluorescence microscopy techniques, we used our VNEA platform to map multiple individual

synaptic connections onto a single postsynaptic neuron. The scalable neuro-electronic interface afforded by the VNEA paves the way for network-level interrogation and modification of large neuronal ensembles, and thus could be used to study the rules by which a neuronal circuit stores and processes information.

To further expand the scale and capability of the VNEA device, we moved towards the development of a hybrid chip with vertical nanoelectrodes directly generated on a CMOS integrated circuit (IC). This work is discussed in Chapter 4; wherein detail the design, fabrication, electrochemical characterization, and biological experiments of our novel CMOS-nanoelectrode array (CNEA). The CMOS architecture enables *in situ* simultaneous, low-noise monitoring of intracellular signals from each electrode with single-cell resolution, and current injection into individual electrodes to stimulate neurons with a broad range of spatiotemporal patterns. The first generation CNEA successfully achieved intracellular measurements and manipulations of membrane potentials in HEK293 cells, cardiomyocytes, and rat cortical neurons. Operating the CNEA in its multiplexed fashion for massively parallel, single-cell-resolution recording/stimulation will (1) facilitate studies of the inner workings of the brain by enabling the generation of functional connectivity maps of neuronal networks and (2) make possible active alteration of the functional connectivity to engineer the network dynamic for cellular neuroprosthesis.

1.2 Nanowires: a fundamental structure for integrated bio-interfacing tools

One-dimensional nanostructures have drawn attention for their utility as building blocks in a wide range of applications. In particular, nanowires (NWs) have emerged as a powerful one-

dimensional nanostructure because of their physical properties and high potential towards integrated devices. NWs (structures characterized by a few nanometers diameter and up to tens of micrometers length) have been studied and used as elements in electronics[1,2], batteries[3-5], photonics[6-9], and biological interrogators/sensors[10-14]. Their advantageous physical properties include small diameter, large surface area, and high aspect ratio. Control over their geometry and chemical composition enables control over electrical, electronic, piezoelectric, magnetic, catalytic, and sensory properties. Besides their physical properties, the ability to generate NWs in a controlled fashion enables excellent control of their dimensions, ordered arrangement, geometrical confinement, and ultimately their integration into complex platforms towards novel devices and applications.

Two different approaches are used to generate nanowires: (1) bottom-up chemical growth and (2) top-down fabrication via lithography and etching. The first approach uses additive nanomaterial growth methods (eg. catalyst-mediated vapor–liquid–solid (VLS)) to tune physical properties. Synthetically realized nanowires have been utilized as building blocks in several nanoscale-based systems, such as nanocircuits and nanoprocessors[1,2,15-18], nanowire assemblies for novel solar cells[19,20], and nano-bio interfaces[11,21-28] (primarily based on nanowire field effect transistors – NWFETs). However, synthetic methods are difficult to scale, limiting applications in complex devices. An alternative approach is to generate vertical nanowires through top-down fabrication methods; thus enabling the generation of high-throughput perfectly ordered arrays of NWs with user defined heights, diameters, densities, and overall patterns. Due to their potential, a wide variety of vertical nanowire-based systems have been developed recently.

NWs are an attractive platform to study cellular phenomena because their nanoscale dimensions allow for minimally invasive, high-resolution interrogation. As such, vertical Silicon

NWs (SiNWs) have been utilized as massively parallel micro-injectors via their direct physical access to cells' interior[29-33]. This platform also allows for systematic perturbation of immune cells, for which there did not previously exist effective delivery methods[34-40], thus enabling a circuit-level understanding of immune cell function once the cellular response resulting from perturbation is measured and analyzed. In addition to their use as a highly effective and universal delivery platform, NWs have been used as building blocks for electronic interfaces that enable the interrogation of bioelectric activity, which underlay major biological communication and functional pathways.

1.3 Studying Signaling Dynamics in Neuronal Networks

Neuronal networks, which consist of a vast number of neurons interconnected via synaptic junctions, are of particular interest and one of the most complex biological systems. Along with forming the physiological basis of many biological organisms' central and peripheral nervous systems, neuronal networks are also the basis of higher order cognitive properties. A central unanswered question in neuroscience is how interactions between neurons give rise to cognition and other high level functionality. Neuronal networks exhibit complex functionality starting at the level of individual neurons. For example, the complexity of the signal dynamics of an individual neuron is seen in action potentials and synaptic potentials, which are dynamic events that involve a complex interplay between the membrane voltage of a neuron and the opening and closing of its ion channels. Fundamentally, it is believed that cognitive processes, such as memory, learning, and logic, result from the coordinated activity of neuronal networks also depicted as bioelectrical circuits. Currently, a thorough understanding of the rules governing these circuits and their functional elements, the neurons, does not exist. Due to this limited

understanding, neurocognitive disorders such as Alzheimer's disease, Autism, and Schizophrenia are particularly difficult to treat and diagnose[41]. Furthermore, a major obstacle to developing accurate descriptions of learning and memory is a lack of experimental tools capable of testing circuit-level theories in neuronal networks.

Recent studies of neuronal circuits[42,43] have been empowered by emerging experimental methods - calcium and voltage sensitive imaging[44-49], genetically-encoded photoactivated ion channels[50], and high-resolution anatomical circuit reconstructions[51-55]. Advances in electron and optical microscopy techniques have made possible to resolve the structural connectome of a small region of an animal's brain down to the level of individual synaptic connections[56]. This structural information, however, does not necessarily provide insight into the network's function. New methods to optically stimulate[50], inhibit[50], and measure[44-47,57] neuronal activity have empowered fluorescence microscopy for interrogation of neuronal circuits[42,58,59]. Optical imaging measures activity-dependent light emissions from neurons, generated by fluorescent indicator proteins (voltage and calcium sensitive dyes). However they provide only a rough approximation of neuronal activity due to due to slow intra-molecular kinetics and indicator saturation at high firing rates. While these methods have significantly expanded our understanding of neuronal networks, they come with significant shortcomings.

While optical techniques are becoming an increasingly powerful and minimally invasive method to interrogate neuronal circuits, electrophysiology remains by far the most accurate method to characterize the activity of ion channels and synaptic currents[60]. Measuring a neuron's membrane potential and its response to the activity of a pre-synaptic cell is one of the few methods (e.g. pathway-focused gene expression analysis) that can determine the strength of their synaptic connection[60-62] (a crucial dynamic quantity long believed to be the basis of learning and

memory). Because whole-cell patch clamp techniques (intracellular electrical recording using a glass micropipette) are the only reliable way to measure and control the cellular membrane potential, they have remained the principle tool in neurobiology for more than 20 years[63]. The general principles of whole-cell patch clamping are summarized in Figure 1.2.

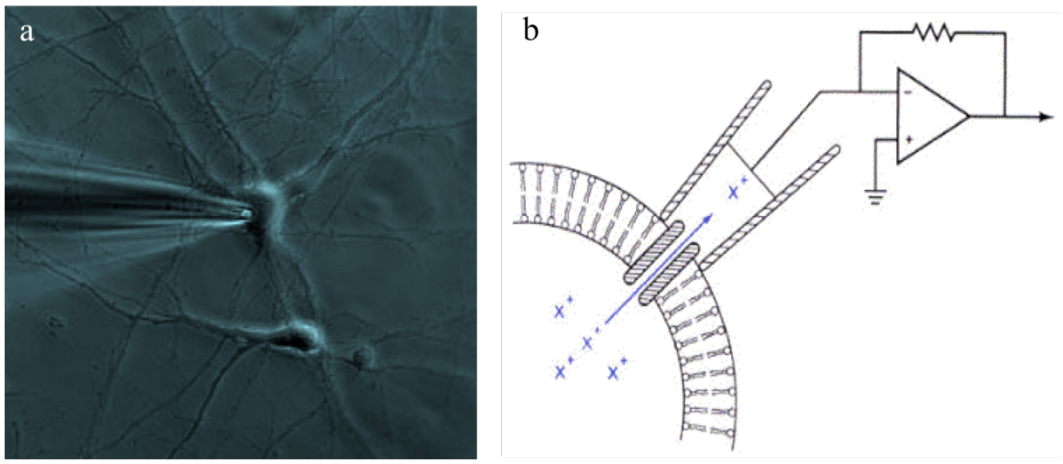

Figure 1.2 | Whole cell patch clamp. (a) Optical micrograph of cultured rat hippocampal neurons and a micropipette interfacing a single neuron in whole-cell mode. (b) Schematic of the general principle of patch-clamp recordings: a glass pipette containing intracellular solution tightly sealed onto the cell membrane and thus isolates a membrane patch electrically. Patch clamping can be run in two modes; (i) Voltage clamp mode: a current is injected into the cell via a negative feedback loop to compensate changes in membrane potential. (ii) Current clamp mode: changes in the membrane potential are tracked by monitoring the patch pipette potential required to maintain a specified command current.

While patch clamp techniques are effective when studying two to three cells at a time for periods up to a few hours[60], they are not scalable to a large network of cells, and long-term recording is an outstanding challenge. New techniques are required to test many theories for learning and memory behavior. Efforts to parallelize this technique via planar patch-clamp chips have not yet been optimized for mammalian neurons, primarily because of difficulties in forming seals to their small neuronal cell bodies[64-68]. For large-scale interrogation of neuronal networks, microelectrode arrays (MEAs) are the tool of choice because they can monitor the neuronal activity from many neurons simultaneously. MEAs measure neuronal signals by detecting the

changes in the extracellular field resulting from the current flows from ionic processes across closest and nearby neurons[69]. A variety of MEAs based on Pt electrodes[64], top-gated[70] and nanowire transistors[13,71-73], etc. have improved the number of neurons which can be measured simultaneously. However, since these measurements are extracellular, they do not provide a clear signal-to-cell registry or information about individual synapses. As a result of these experimental limitations, the principles of neuronal coding – the rules by which neuronal circuits store and processes information – remain among the brain's least understood functionalities[74].

To address some of these issues and pave the way for large-scale neuronal network studies, semiconductor nanofabrication-based approaches have been employed to generate a new class of electrical interfaces to neurons and other electroactive cells. These tools, reviewed in detail elsewhere, rely on nano- and microscale structures that provide a minimally invasive interface to the cell's interior. For example, gold mushroom-shaped microelectrodes can perform multisite 'intracellular-like' recording and stimulation of neuronal activity in *Aplysia* neurons and primary rat cardiomyocytes[75-77]. Similarly, nanoscale structures based on field-effect transistors (FET) or vertical platinum nanowires enable true intracellular recording of action potentials in cardiomyocytes[10,11,72,73]. Each of these methods utilizes nanofabrication approaches to create recording platforms that can be scaled up to interrogate many cells simultaneously without using micromanipulators. A logical next step, then, is a nanofabricated device specifically designed and optimized to stimulate and record the activities of primary mammalian neurons.

CHAPTER 2

Generation of Biomolecular Perturbation and Imaging Platforms through High-Throughput, High-Precision Nanowire Fabrication Methods

2.1 Introduction: Vertical and opaque silicon nanowires

Controlled and specific biomolecular perturbations comprise the basis of the majority of studies that aim to elucidate cellular function[78-83]. A generalized platform for high throughput interrogation and manipulation of living cells could transform investigations of intra- and inter-cellular processes. Vertical silicon nanowires (SiNWs) are a promising foundation for such technology. They are capable of penetrating a cell's membrane in a minimally invasive fashion, providing a multiplexed chemical and electrical interface to the cell's interior[84-88].

Studies in our lab established surface-modified SiNWs as a spatially localized, efficient, and universal biomolecular delivery platform[89]. Surface modification, particularly aminosilane coating of the SiNWs, facilitated noncovalent (electrostatic and/or van der Waals), nonspecific binding of a variety of biomolecules. Cells were subsequently plated on the coated SiNWs and incubated to allow for intracellular nanowire penetration and slow release of the biomolecules. Figure 2.1 summarizes the operational principle of this SiNW perturbation platform.

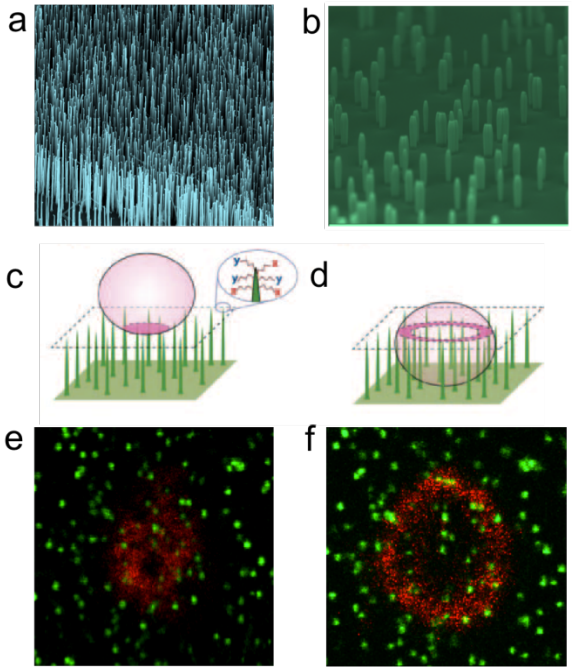

Figure 2.1 | SiNWs: A generalized platform for delivering a large variety of biological effectors. (a) and (b) Scanning electron micrographs of vertical SiNWs fabricated via CVD and reactive ion etching, respectively. Scale bar in (a) and (b), 1 μm. (c) and (d) Schematic renderings of cells (pink) on SiNWs (green) at early and late stages of penetration, respectively. Molecules of interest (X & Y) are non-specifically tethered to the SiNW surface via alkoxysilane treatment. Upon penetration and delivery, those molecules can alter the cell's behavior. (e) and (f) Confocal microscope sections (corresponding to the dashed boxes in c and d) of a HeLa cell in the process of being penetrated. Scale bar in E and F, 10 μm. (e) After 15 minutes, the cell membrane, labeled with DiD, sits atop the tips of the wires that are coated with cystamine and Alexa Fluor 488 SE (as shown in c). (f) Within one hour, the same plane shows a red circle, the cell's circumference, surrounding green-labeled wires, indicating NW penetration into the cell (as shown in d). Regardless of the molecular coating, the majority of cells are penetrated within one hour.

Direct access to the cells' interiors enables NWs to efficiently deliver a broad range of exogenous materials into multiple cell types, without the need for chemical or viral packaging protocols required by other methods. Fluorescence images in Fig 2a to d show immortalized (HeLa) and primary cells (human fibroblasts, rat neural progenitor cells (NPCs), and rat hippocampal neurons) expressing fluorescent proteins encoded by plasmid DNAs that were administered using SiNWs, whereas Fig. 2.2e to h demonstrates the delivery of various biomolecule, (siRNAs, peptides, DNAs, and proteins). Moreover, different types of biomolecules can be introduced into the same cell simultaneously by simply codepositing them onto the NWs, as illustrated in Fig. 2.2i to l. The fluorescence images in Fig. 2.2e to l were obtained by culturing human fibroblasts on Si NWs to which diverse fluorescently labeled molecules were attached. Because the vertical NW platform is compatible with live-cell cultures and common imaging protocols, phenotypic responses to exogenous biological effectors can be assayed directly using standard microscopy techniques.

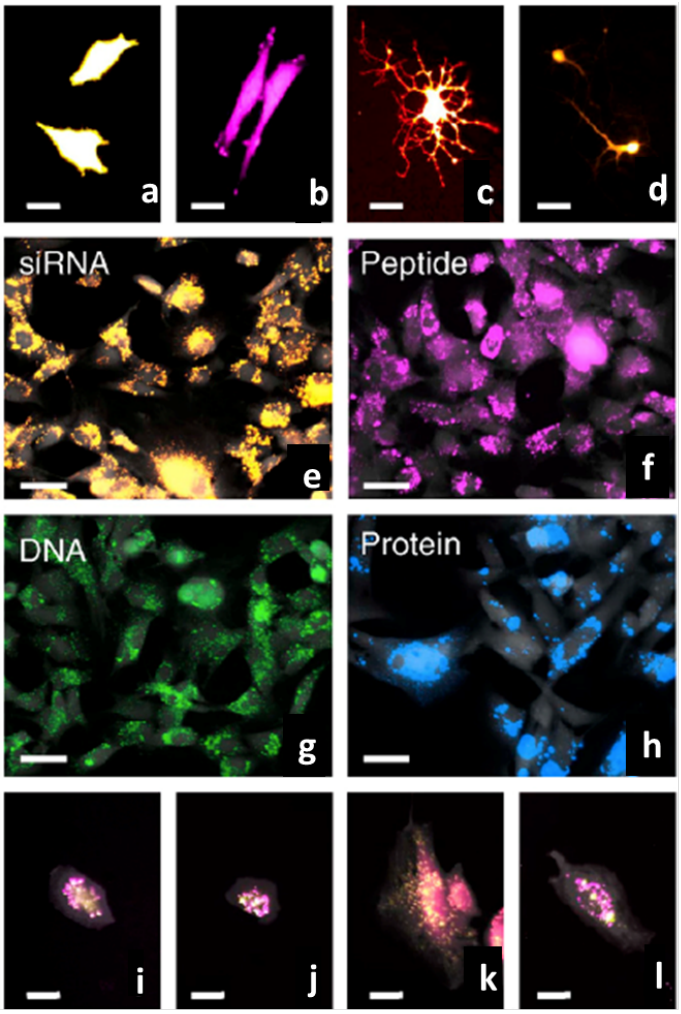

Figure 2.2 | Si NWs can deliver and codeliver diverse biomolecular species to a broad range of cell types. (**a**)-(**b**) Various immortalized and primary cell types expressing fluorescent proteins after being transfected with plasmid DNA via the Si NWs: (**a**) HeLa S3 cells (pCMV-TurboRFP), (**b**) human fibroblasts (pCMVTurboRFP), (**c**) NPCs (pCMV-mCherry), and (**d**) primary rat hippocampal neurons (pCMV-dTomato). Scale bar in **a-a**, 25 **µ**m. (**e**)-(**h**) Human fibroblasts transfected with a variety of biochemicals. To verify intracellular delivery, following a 24-h incubation on coated Si NWs, cells were replated on glass coverslips for imaging. Epifluorescence images show >95% of the cells receive: (**e**) siRNA (Alexa Fluor 546 labeled AllStar Negative Control siRNA), (**f**) peptides (rhodamine labeled 9-mer), (**G**) plasmid DNA (labeled with Label-IT Cy5), and (**h**) proteins (recombinant TurboRFP-mito). Scale bars in **e-h**, 50 **µ**m. (**i**)-(**l**) Fluorescence images of human fibroblasts cotransfected with two different molecules using Si NWs: (**i**) two different siRNAs (Alexa 546 labeled siRNA-yellow & Alexa 647 labeled siRNA-magenta), (**j**) a peptide and an siRNA (rhodamine labeled peptide-yellow & Alexa 647 labeled siRNA-magenta), (**k**) plasmid DNA and an siRNA (Cy5-labeled TagBFP plasmid DNAyellow & Alexa 546 labeled siRNA-magenta), and (**l**) a recombinant protein and an siRNA (recombinant TurboRFP-mito-yellow & Alexa 647 labeled siRNA-magenta). In **e** to **l**, to facilitate identification, cell membranes were labeled with fluorescein (**Gray**). Scale bars in **i–l**, 25 µm.

2.2 SiNW Fabrication Method

To further expand the applicability and utility of the SiNW platform, we developed a novel method to fabricate perfectly ordered SiNW arrays with user defined heights, diameters, densities, and overall patterns. Further implementation and integration of this method enables massively parallel high-throughput screening. Principally, our method utilizes a top down fabrication approach that integrates a wide variety of well-understood semiconductor processes. In brief the fabrication process consists of the following steps, as shown in Fig. 2.1: (1) A silicon wafer is coated with a thin resist. (2) That resist is patterned using lithography (stepper photo-lithography) and development to define a series of resist holes at specified locations – these holes mark the location of the SiNWs to be fabricated. (3) A hard etch mask (preferably aluminum oxide for maintaining CMOS compatibility) is deposited and the resist is lifted off to leave hard etch mask spots at the sites of SiNWs-to-be. (4) The exposed silicon is etched to the desired depth using a reactive ion etch (RIE), yielding SiNWs pillars of the specified height at the protected sites. Our standard process RIE was performed for 25 minutes using the STS ICP RIE at 1200RF power, while flowing in 160sccm C_4F_8 and 60sccm SF_6 gas, which leads to selective etching of the silicon substrate underneath. (5) The hard etch mask is removed. (6) At this point, the SiNWs can be used as previously described[90] or their diameters can be adjusted down by oxidation (preferably, thermally) and subsequently etching away the formed oxide (RIE or a wet etchant, e.g. HF). This process can be cycled as needed.

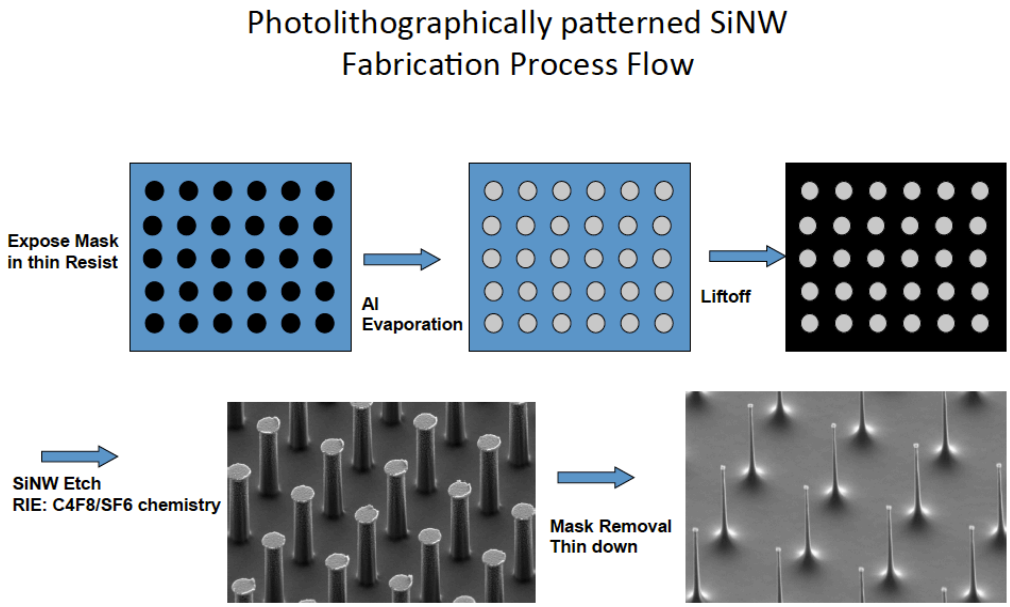

Figure 2.3 | Summarized process-flow of patterned SiNW fabrication: 1 – A thin resist is patterned; 2 – The inverse of the pattern is generated by depositing a hard mask and lifting off; 3 – Exposed silicon is etched down to leave SiNWs; 4 – The etch mask is removed; and, 5 – If desired the SiNWs are thinned down using cycles of oxidation and selective oxide etching.

The development of this optimized top-down fabrication process enabled the scalable production of SiNWs with complete tunable geometry (length, density, diameter). In particular, using stepper photolithography for the definition of this array allows for precise control of the pitch between NWs and by extension the amount of nanowires that will engage a typical cell cultured on top of them. For smaller suspension cells like B and T-cells, the density is about 0.65 NW per μm^2, which corresponds to an array with a 1.25µm pitch. The height of the NWs emerging underneath the mask is controlled accurately by the RIE step. In addition, the final diameter of the nanowires can be controlled within a few tens of nanometers by repeated oxidation and oxide removal (Fig 4 c,d). Control over the NW profile, using different thin-down strategies, enables the fine-tuning of NW geometry thus in the generation of the optimal interface with cells of different characterizing features. In particular, the sharpness of the NW tip (e.g. Fig 4f) turns out to be of crucial importance for delivery of biomolecules to suspension cells that, compared to adherent cells, adhere less strongly to the culture substrate.

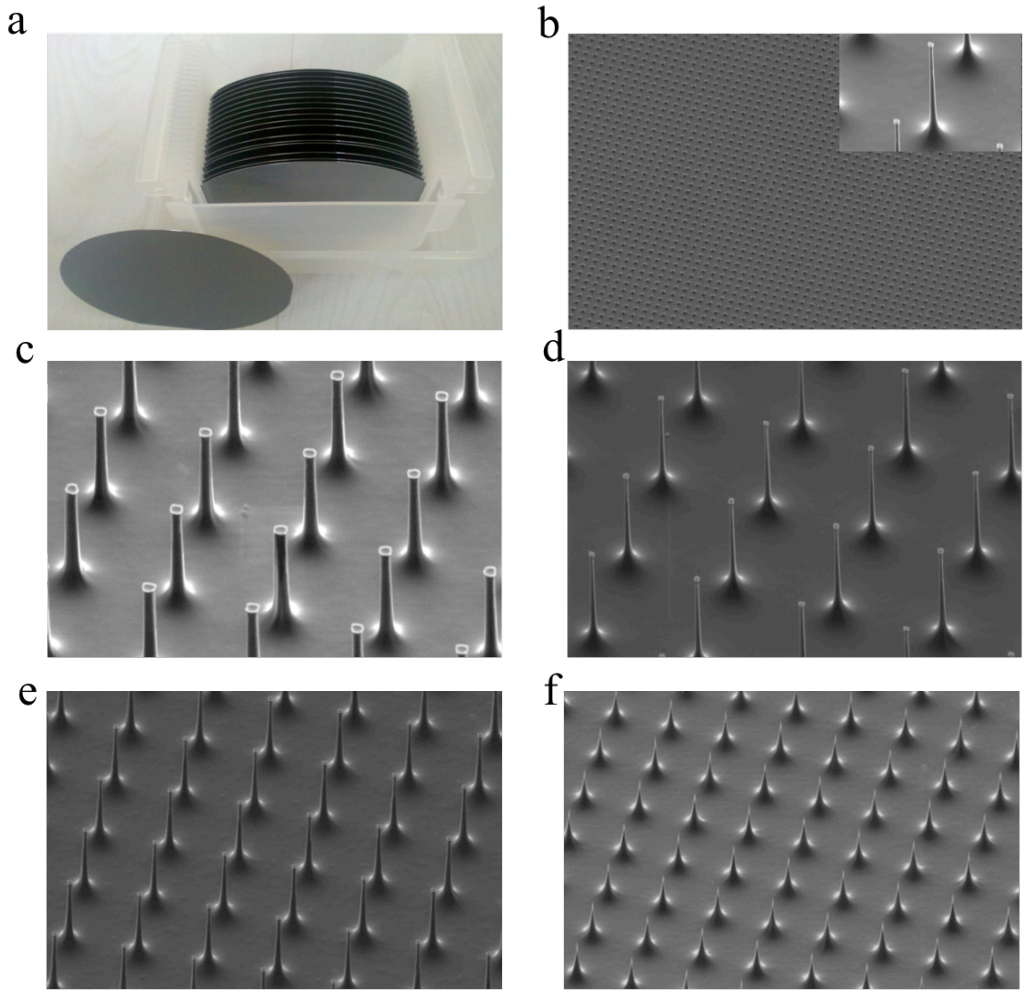

Figure 2.4 | SiNWs can be fabricated with consistent geometries at a specified density over a large area. (c – d) The diameter of the patterned SiNWs can be controlled by repeated oxidation and oxide removal. Different thinning strategies can be used to define SiNW shape and profile, (e) conformal and (f) directional.

2.3 Biomolecular perturbation using SiNWs

The SiNW platform has been applied to address fundamental problems in immunology through several collaborations[91-95]. By using the NWs to deliver perturbants into primary immune cells, we have interrogated the intracellular circuits that drive cellular functions in both normal and diseased states. As previously described, NW surface termination facilitates the conjunction of biomolecules[92,94]. A short aminosilane was used to bind siRNA to the nanowire surface in a non-covalent manner. This charge

based, non-specific binding method opens up the possibility to employ the NW platform to co-deliver different types of biomolecules (mRNA, plasmids, negatively charged proteins, etc.). Subsequently, the siRNA coated NWs are used as a culture substrate and merely by gravitational forces cells will settle onto the vertical nanowires, allowing siRNA release to the cytoplasm over time. Analysis by confocal microscopy of human B-cells (cell membrane colored magenta) from CLL patients cultured on top of a NW substrate (colored white), suggests that NWs reside in the cytoplasm (Figure 2.3.2a). In addition, being cultured on top of a NW substrate did not alter cell health or morphology greatly (Figure 2.3.2b). Importantly, NW-mediated delivery neither activated an immune response nor interfered with normal immune sensing, cellular activation, or cell proliferation in response to physiological signals.

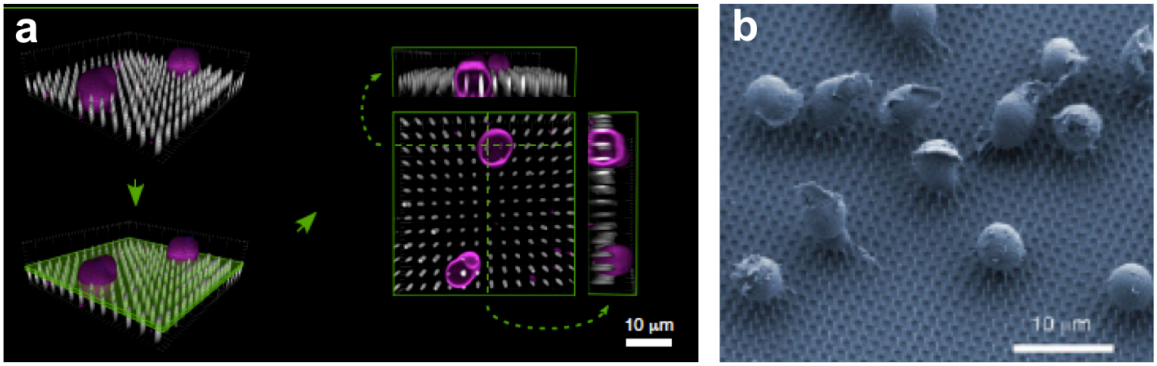

Figure 2.5 | Nanowires can deliver siRNA into ex vivo primary immune cells. **(a)** Three dimensional reconstruction (left) of confocally imaged human B cells (membrane: magenta) on top of Alexa-labeled NWs (white). (b) Scanning electron microscope images of CLL-B cells on top of NWs taken 24 h after plating.

The NW substrates were successfully used to introduce a variety of molecular cargo into immune cells; in particular, to investigate the molecular circuits that guide naïve mouse CD4+ T-cell differentiation [96]. Imbalance in the population of T-cell subtypes can lead to various autoimmune diseases because proper immune system function requires a balanced population and their proper activation [97,98]. Consequently, identifying the relevant molecules and pathways that control naïve T-cell differentiation is not only a basic scientific problem, but also one with substantial clinical relevance. To address this, we combined transcriptional profiling at high temporal resolution, novel computational algorithms, and

innovative nanowire-based tools for performing perturbations in primary T-cells to systematically derive and experimentally validate a model of the dynamic regulatory network that controls Th17 differentiation (Fig. 2.6). By profiling gene expression during Th17 differentiation, we identified genes that were differentially expressed with respect to controls that lacked Th17 inducing cytokines (TGF-B & IL-6). Using this time-course data, we reconstructed a dynamic regulatory network model for Th17 differentiation consisting of three distinct temporal phases.

In order to experimentally validate this model and infer directionality of regulation, we needed to perturb key Th17 differentiation genes; yet, traditional perturbation methods, like viral- or transfection-based siRNA delivery, have been of limited utility since they either alter differentiation or cell viability in unstimulated primary mouse T-cells [99,100]. By leveraging NW-based siRNA delivery, we were able to get around this hurdle and successfully knockdown 39 regulators in the Th17 network. Figure 2.6c shows scanning electron micrograph of primary T-cells (false colored purple) cultured on vertical silicon nanowires. This perturbation data allowed us to identify that the network is organized into two antagonistic modules: a module of 22 'Th17 positive factors', whose perturbation decreased the expression of Th17 signature genes, and a module of 5 'Th17 negative factors', whose perturbation did the opposite. The two antagonistic modules may play a key role in maintaining the balance between Th17 and other T-cell subsets and in self-limiting the pro-inflammatory status of Th17 cells. To further analyze the role of key novel genes, the validated model was tested by differentiation of naïve T-cells from knockout mice of the novel factors. Intracellular staining followed by flow cytometry and cytokine analysis (ELISA) of the corresponding supernatants confirmed the predictions by our model. Overall, this study identified and validated 39 regulatory factors, embedding them within a comprehensive temporal network and revealing its organizational principles, and highlighted novel drug targets for controlling Th17 differentiation[96].

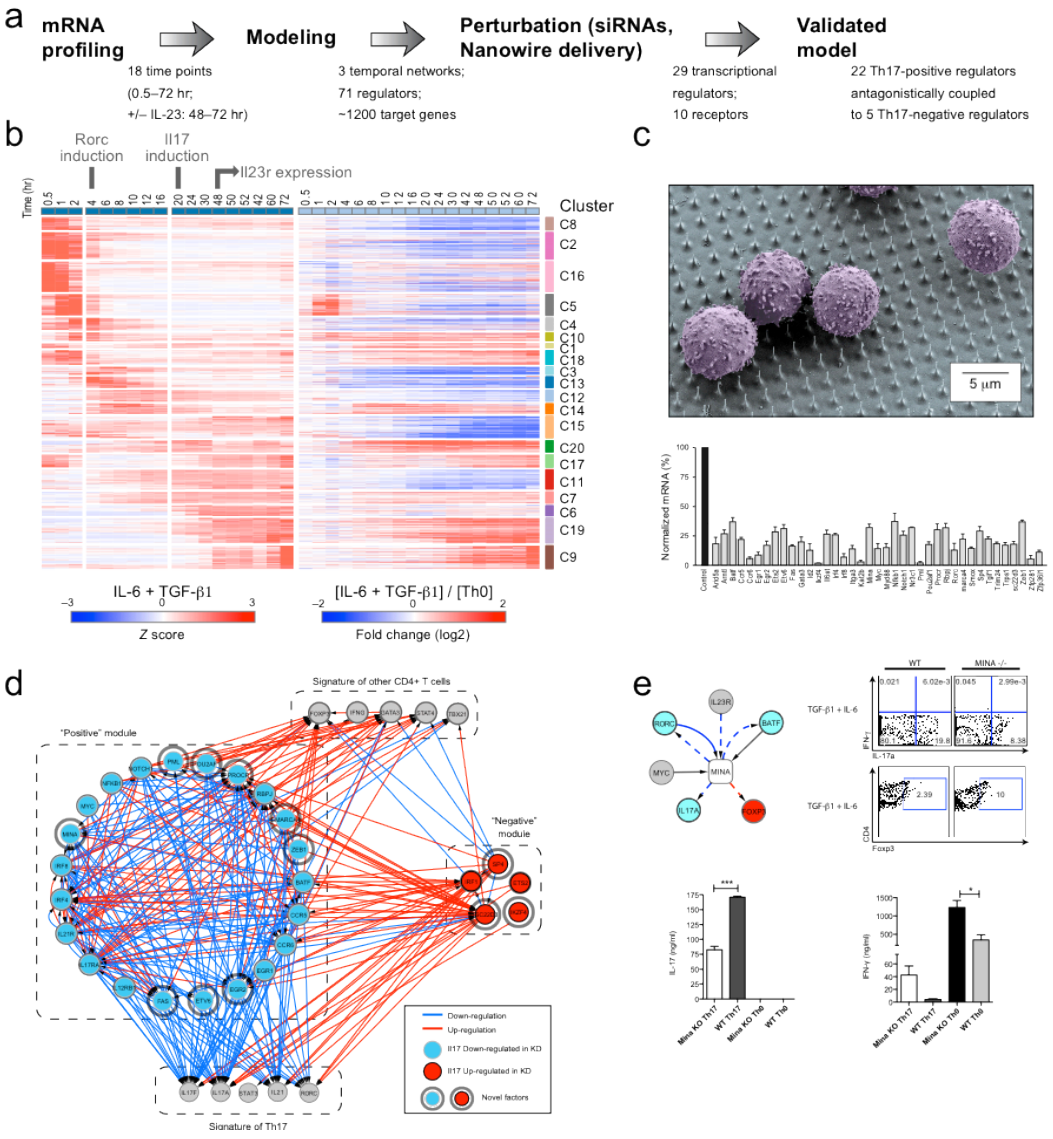

Figure 2.6 | (a) Overview of approach. (b) Gene expression profiles during Th17 differentiation. Shown are the differential expression levels for genes (rows) at 18 time points (columns) in Th17 polarizing conditions (TGF-β1 and IL-6; left panel, Z-normalized per row) or Th17 polarizing conditions relative to control activated Th0 cells (right panel, log2(ratio)). The genes are partitioned into 20 clusters (C1-C20, color bars, right). (c) Scanning electron micrograph of primary T cells (false colored purple) cultured on vertical silicon nanowires. (c) Effective knockdown by siRNA delivered on nanowires. Shown is the % of mRNA remaining after knockdown (by qPCR, Y axis: mean ± standard error relative to non-targeting siRNA control, n = 12, black bar on left) at 48hrs after introduction of polarizing cytokines. (d) Two coupled and opposing modules. Shown is the perturbation network associating the 'positive regulators' (blue nodes) of Th17 signature genes, the 'negative regulators' (red nodes), Th17 signature genes (grey nodes, bottom) and signature genes of other CD4+ T cells (grey nodes, top). A blue edge from node A to B indicates that knockdown of A downregulates B; a red edge indicates that knockdown of A upregulates B. Light grey halos: novel regulators. (e) Example network model of key targets and regulators (round nodes) connected to the pivotal nodes based on perturbation (red and blue dashed edges), TF binding

Figure 2.6 (Continued). (black solid edges), or both (red and blue solid edges). Intracellular staining and cytokine assays by ELISA or Cytometric Bead Assays (CBA) on culture supernatants at 72h of in vitro differentiated cells from the respective KO mice.

2.4 Future directions of SiNW-based platforms

In future efforts, we will enhance the scale at which NW-based perturbations can be performed to accommodate large-scale perturbation studies towards the facilitation of conducting a genome-scale screen of regulators in primary immune cells (~500-1,000 genes). For this purpose, by selectively protecting regions of the silicon wafer, regions without SiNWs can be generated. This enables the delineation of active delivery (SiNW-containing) regions and non-delivery zones (Fig 7). By attaching a well structure, made of patterned silicon, PDMS, or any other polymer, these active zones can be isolated from one another to generate SiNW transfection wells. Subsequently, different molecular reagents can be deposited within these wells (by pipetting, micro arraying, or the like) and then, by adding cells to the entire structure, the consequences of delivering different molecules, either alone or in combination, can be assayed in parallel in high throughput. Different cells can be spotted onto different areas to enable a screen of fewer molecules across multiple cell types. Similarly, the washers that define the assay wells can be affixed to the surface without pre-defining SiNW free binding regions by using photoresist to protect certain areas and then adding a curable polymer; similarly, wells can be defined by photo-lithographically patterning boundaries in a photo-curable polymer or resist (e.g., spin on glass) and the developing.

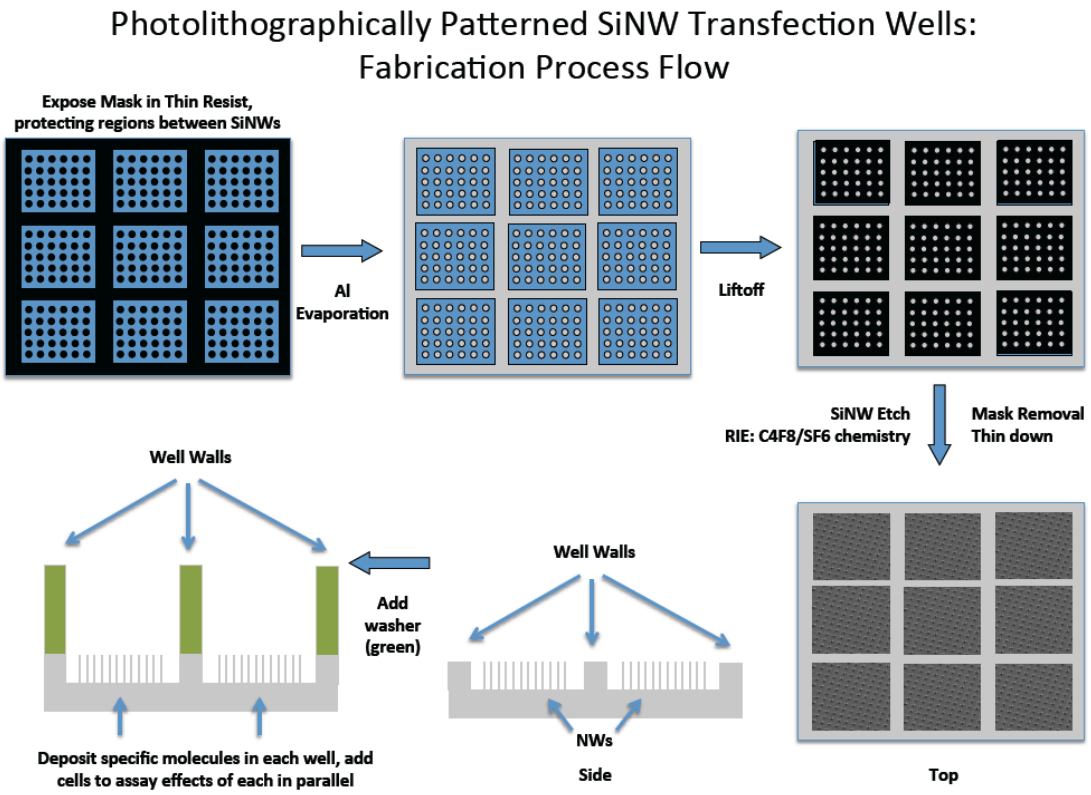

Figure 2.7 | By selectively protecting regions of the silicon surface, spots of SiNWs can be made. Once these transfection-competent regions are defined, they can be isolated through the addition of a washer structure (e.g., PDMS). Coupled with selective dispensing, this enables the functional consequences of a wide variety of different molecules (e.g., drug candidates, siRNAs) to be assayed, either alone or in combination, in parallel using a small area and a small number of cells, thus enabling truly high throughput screens.

We envision that this strategy will enable a series of efficient and effective high-throughput screens (e.g., small molecule libraries, genome wide siRNAs, etc.), even with limited numbers of cells and scarce reagents. If wells of 175 um by 175 um are generated at 200 um pitch, 25 would fit in a square mm, and more than 400,000 wells would fit onto a standard 6 inch silicon wafer (1.6 million on a 12 inch). This means that over 400,000 (1.6 M) different molecules (of the same or different specifies) or combinations thereof could be screened simultaneously using one SiNW wafer. The compact assay spot would reduce reagent and cell requirements. Also, the full wafer can be trimmed to any shape with a dicing saw to enable compatibility with different high-throughput screening platforms (e.g., optical microscopes). Finally, in order to accommodate large-scale perturbation studies, efforts could be taken to

automate the protocol. By coupling the nanowire platform to robotics, a high throughput process line, including fluorescence based phenotype readout, can be established that enables quick screening, and expand the combinatorial combinations that can be probed.

2.5 Generating transparent SiO_2 NW based platforms

Vertical Si NWs have been broadly utilized as a scalable and highly effective platform to obtain intracellular access to living cells for both perturbing and observing their cellular phenomena. To further expand the functionality of vertical nanowires, we moved into the development of a similar biological interface with the distinct feature of transparency in comparison to the opaqueness of Si NWs. The advanced transparent nanowire arrays are realized by employing optimized Si NW fabrication techniques on top of quartz wafers. These transparent structures pave the way towards truly multiplexed platforms that can be directly integrated with microscopy systems paving the way towards novel applications including: (1) the visualization of the nanowire/cellular-membrane interface through stochastic optical reconstruction microscopy (STORM) and (2) the development of a new sensing platform that consists of nanodiamonds (NDs) selectively tethered at the nanowire tips.

2.6 Fabrication Summary

Transparent NW substrates are prepared in via a top-down approach by etching them from silicon dioxide (SiO_2; quartz and/or fused silica) wafers using standard semiconductor techniques (stepper lithography, directional reactive ion etching, and isotropic wet etching) tailored for this application. Varying the processing parameters can precisely control the structural profile and layout of the SiO2 NWs (Fig. 2.8b), in similar fashion with the opaque Si NWs as described above. To achieve the critical parameter of feature uniformity within the die and across the wafer, we implemented two additional steps. First, we corrected for pattern non-uniformity that resulted from optical reflection due to the transparent substrate by depositing a reflective film (Copper) in the bottom of the wafer. This prevents any reflection

from the wafer holding chuck, thus improving exposure uniformity. In addition, an anti-reflective coat (ARC) layer on the top of the wafer was used to reduce unwanted optical effects from backscattering and reflection through the photoresist. The process described above is performed on 4-inch wafers (Fig. 2.8a), which can be subsequently diced up and/or post-processed for particular applications.

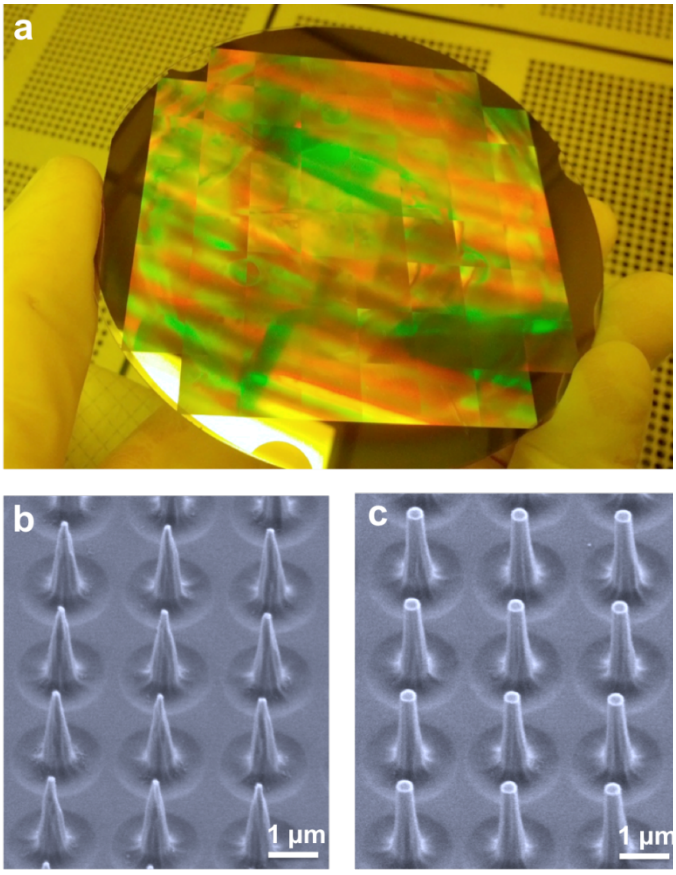

Figure 2.8 | Fabrication of transparent nanowires from quartz wafers

2.7 STORM Experiment

The distinct feature of transparency enables these NW based platforms to be implemented with STORM for superresolution imaging[101] based on the high-accuracy localization of individual fluorophores. As shown in Fig. 2.9a, bare SiO2 NWs labeled with Alexa-647 fluorophore were imaged in index-matched media by maximizing the possible localizations to define their overall structure over a 1µm length (z-dimension). To visualize the interface between the NWs and the cellular membrane of

primary cells we cultured bone-marrow-derived dendritic cells (BMDCs) on top of labeled SiO2 NWs. Pre-imaging sample preparation consisted of two steps: (1) fixating the cultured cells with paraformaldehyde combined with glutaraldehyde and (2) labeling the cellular membrane with CM-Dil. The distinct and separated emission spectra of Alexa-647 and CM-Dil allowed for multicolor STORM imaging using a multichannel fluorescence detection scheme. Figure 2.9b, bottom shows the x-z projection of the NW-membrane interface of the boxed region shown in Fig. 2.9b, top, indicating the cellular penetration of SiO_2 NWs. A similar multicolor approach can be used to achieve superresolution imaging of live cellular cultures, which are being perturbed via the NWs. Integrating the capability of SiO_2 NW intracellular perturbation with superresolution imaging, through their transparent substrate, will facilitate truly multiplexed studies of complex biological systems paving the way towards new insights at the nanoscale.

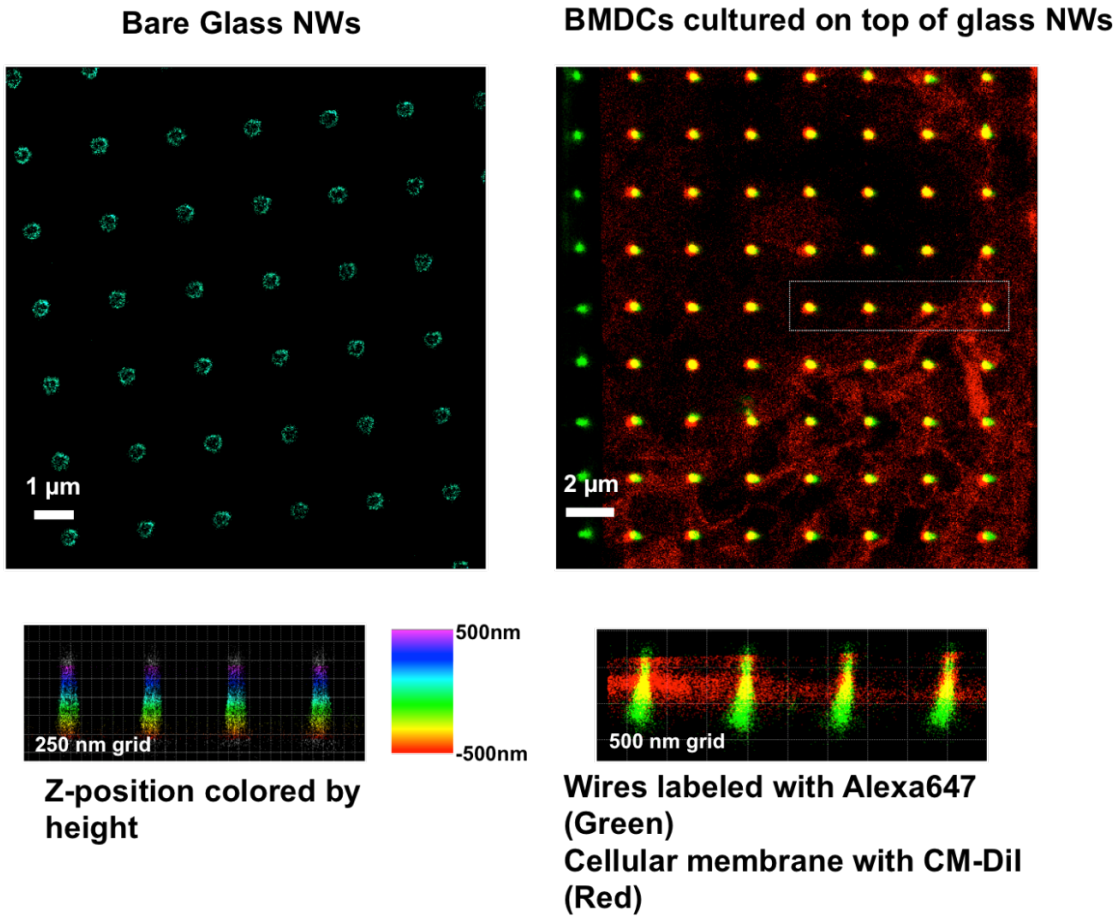

Figure 2.9 | Visualization of the NW/cellular-membrane interface through STORM.

2.8 Nanowire - Nanodiamond Integration

Another aptitude of the transparent SiO_2 NWs as an interfacing substrate is the possibility to develop a new sensing platform that consists of nanodiamonds (NDs) selectively tethered at their tips. As discussed below, NDs enable the measurement of voltage changes by leveraging the nanoscale magnetic and electric sensing properties of nitrogen-vacancy centers in NDs[102-105]. Their integration with SiO_2 NWs ensures optimal placement of the NDs in close proximity to the plasma membrane for achieving high sensitivity and enables detection of the voltage pulses through the transparent substrate. This platform will enable minimally invasive interrogation of neuronal networks with high-spatial resolution.

Nitrogen vacancy (NV) centers in nanodiamonds are distinguished by superior optical properties and are paving the way for the development of novel applications such as bright biomarkers, switch-controlled emitters for high-resolution microscopy, and optical sensors for electrochemical detection. Their capability as nanoscale optical sensors and probes has shown great potential for biological sensing applications, in particular for measuring the membrane potential. Recent developments in optical voltage sensors, including voltage-sensitive dyes and genetically coded proteins, are limited due to their properties of intracellular delivery, potential toxicity, and typical photo bleaching. The NV centers in nanodiamonds, with their photoluminescence sensitivity to perturbations in electric fields and chemical changes, provide a non-invasive technique for highly sensitive detection of electrochemical activity with remarkable biocompatibility.

To avoid shortcomings associated with the direct field-sensing[106] method (including imperfect spin readout of a single NV center and the Debye screening of the membrane potential), we have implemented NV center charge state readout as an indirect electric-field detector. The NV center can exist in two charge states, NV^- and NV^0, which are associated with distinct excitation and fluorescence spectra that enable fast (less than 15μs) and efficient (fidelity > 90%) readout of the charge state[107,108]. The equilibrium state of an NV can shift between NV^- and NV^0 (directly leading to the fluorescence spectra change) when the NV center is subject to an external electric field. In this way, the detection of the

spectra shift, through spectral filtering of fluorescence photons, enables the measurement of electric fields. Figure 2.10 depicts the results of our proof-of-concept experiment demonstrating the detection of voltage pulses through the detected fluorescence signals. We simulated a cellular-like measurement setup, schematically shown in Fig. 2.10a, consisting of the detector platform (nanodiamonds deposited on a glass slide coated with a conductive indium-tin-oxide (ITO) film), the extracellular solution, and an electrode immersed in the extracellular solution. We utilized the immersed electrode as the source of voltage pulses to simulate changes in cellular membrane potential. The preliminary results, Fig. 2.10c, demonstrate the detection of increasing amplitude voltage pulses (0 to 500 mV) characterized by 1 ms duration, thus showing the feasibility of this new voltage-sensing modality through the measurements of the fluorescence signal.

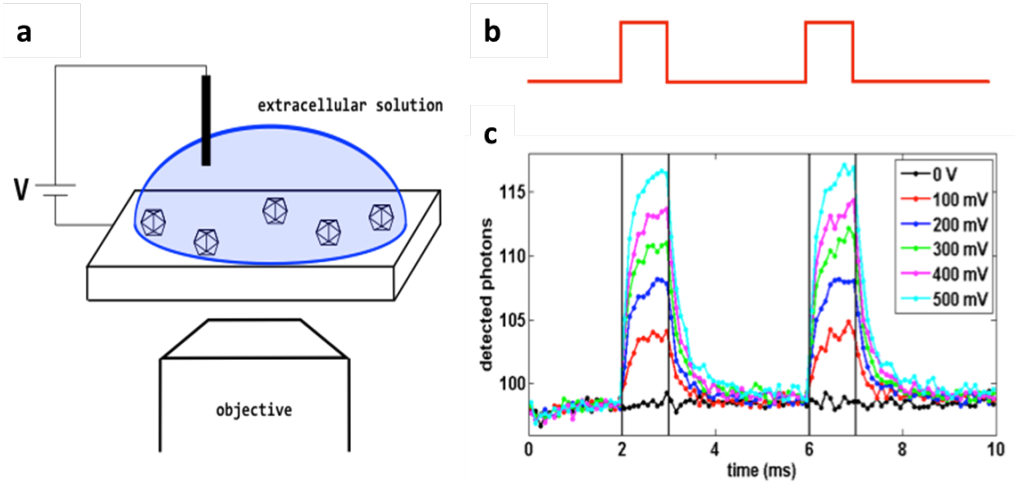

Figure 2.10 | (a) The nanodiamonds, drop-cast on a glass slide with a conductive indium-tin-oxide (ITO) coating. (b) The voltage pulses that simulated membrane potential changes were applied to an electrode that was held inside extracellular solution, which was in contact with the surface. (c) Detected fluorescence signals, showing detection of the voltage pulses, for pulse amplitudes between 0 and 500 mV.

Having shown this novel voltage-sensing modality, we moved towards the integration of the nanodiamond sensors with the SiO_2 NW substrate to further expand and optimize the platforms' potential. This combined platform was achieved via a multiple step process-flow, Fig. 2.11a, which allowed the generation of a conductive surface in addition to the conjunction of NDs in a selective methodology.

Briefly, these step consisted of: (1) conformal deposition of a conductive indium-tin-oxide (ITO) via sputtering, (2) surface functionalization with aminosilane, (3) selective tip exposure through a height controlled resist layer to shield the base, (4) ND covalent attachment via drop-casting a solution with activated NDs, and (5) resist removal and sample clear-out. Figure 2.11b shows SEM images of the final results of our ND-NW platform preparation, demonstrating our control over the localization of the NDs on the NWs. To evaluate the properties of the post-processed NDs attached to NWs and the characteristics of the transparent substrate, we utilized the pulsed electron spin resonance (ESR) technique. The fluorescence detection in the x-y plane, shown in Fig 2.11d, depicts a good uniformity of the ND distribution across the NW array. Furthermore, the ESR spectra (NV population in m_s=0 vs. microwave (MW) frequency) show the typical MW frequency that is resonant with the m_s=0 to m_s=1 spin transition, Fig. 2.11e. The ability to achieve optical detection through the NW substrate demonstrates the possibility of generating the ND-NW integrated platform with great potential.

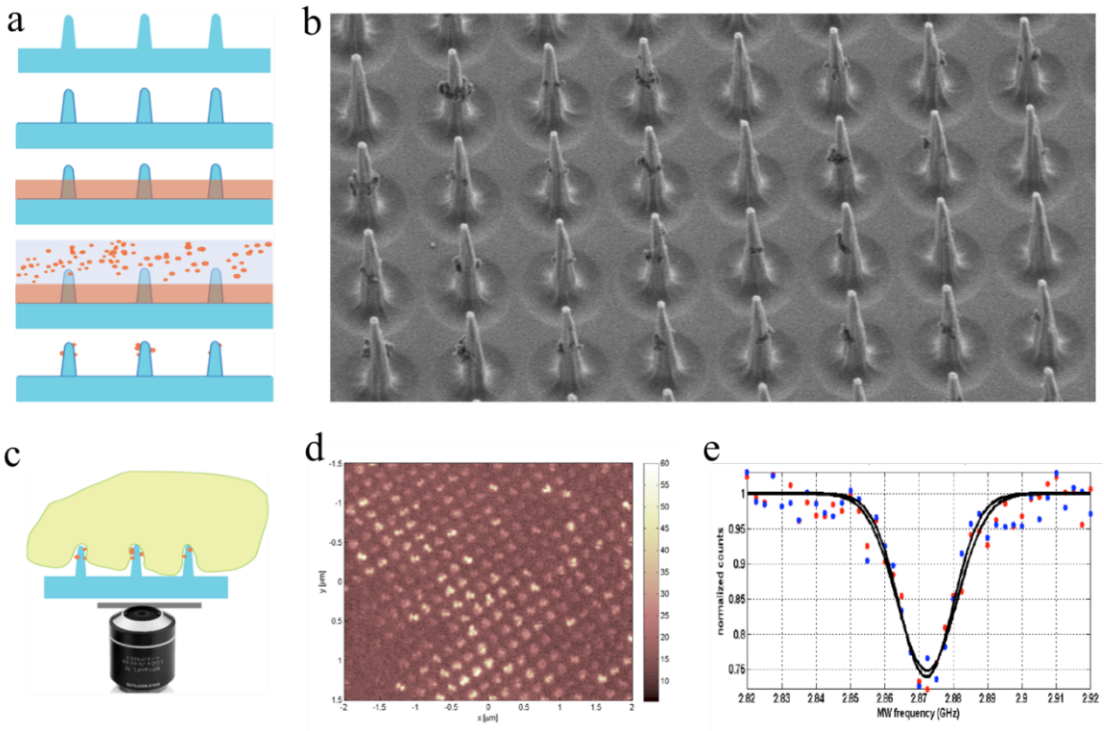

Figure 2.11 | Nanodiamonds integrated with transparent NWs. (a) Process flow to selectively attach NDs to the SiO_2 NWs. (b) SEM images of NDs tethered to the upper portion of the vertical NWs to achieve high SNR. (c) Schematic of the sensing platform interfacing a single cell. (d-e) ESR on NDs

Figure 2.11 (Continued). attached to SiO_2 array.

2.9 Conclusions and prospects

The development of these integrated and transparent, NW-based platforms gives rise to novel nanoscale based interrogative techniques for biological systems. Building upon the current results, we will utilize the ND-NW platform to investigate neuronal networks through measurements of their membrane potential. Besides the ability of the NV detection system to acquire the membrane potential activity in a non-invasive fashion with high spatial resolution, the integrated platform facilitates the well-controlled and optimized localization of ND sensors to achieve high signal-to-noise ratio. While, monitoring the membrane potential in multiple points of a single neuron can be used to map intracellular dynamics of neuronal activity, large-scale interrogation at the network level will facilitate the determination of the combined functional and structural connectivity.

CHAPTER 3

Vertical Nanowire Electrode Arrays as a Scalable Platform for Intracellular Interfacing to Neuronal Circuits

3.1 Introduction

Deciphering the neuronal code - the rules by which neuronal circuits store and process information - is a major scientific challenge[42,74]. Currently, these efforts are impeded by a lack of experimental tools that are sensitive enough to quantify the strength of individual synaptic connections and also scalable enough to simultaneously measure and control a large number of mammalian neurons with single-cell resolution[60,64]. Here, we report a scalable intracellular electrode platform based on vertical nanowires that affords parallel electrical interfacing to multiple mammalian neurons. Specifically, we show that our vertical nanowire electrode arrays (VNEAs) can intracellularly record and stimulate neuronal activity in dissociated cultures of rat

cortical neurons and can also be used to map multiple individual synaptic connections. The scalability of this platform, combined with its compatibility with silicon nanofabrication techniques, provides a clear path toward simultaneous, high-fidelity interfacing with hundreds of individual neurons.

To date, most microfabricated neuronal interfaces have been based on electrodes that reside outside of the cellular membrane, preventing their use for measuring sub-threshold events and also prohibiting precise cell-to-electrode registration[64,65,71,109-113]. Recently, emerging nanofabrication techniques have enabled the development of new micro- and nanoscale devices that exhibit significantly improved electrical coupling between cells and electrodes. Notably, gold mushroom-shaped microelectrodes have been used to perform "intracellular-like" recordings from *Aplysia* neurons and mammalian cell lines[75,76,114], and true intracellular recordings from several mammalian cell lines and cardiomyocytes have been realized using microfabricated planar patch clamp devices[66-68] and kinked nanowire probes[11]. Although these examples represent major advances in cell-electrode coupling, they have been either too large to interface to mammalian neurons[66-68,75,76], or lack the scalability required to perform simultaneous measurements of multiple cells[11].

3.2 Device Design and Fabrication

Our VNEA is specifically designed to address these issues by leveraging the same nanofabrication technology that enables mass production of integrated silicon electronic circuits. Vertical nanowire electrode arrays (VNEAs) were fabricated on a silicon-on-insulator (SOI) wafer with a degenerately doped device layer (Ultrasil Corp., *n*- and *p*-type, 0.001 – 0.005 Ohm·cm), as depicted in Fig. 3.1. Our prototype VNEA device consisted of 16

stimulation/recording pads (200 μm pitch), each containing 9 vertical silicon nanowires (3 × 3, 2-μm pitch, Figs. 2A-C). Silicon nanowires (~ 150 nm in diameter and 3 μm in length) were fabricated via reactive ion etching (RIE) and thermal oxide thinning. Briefly, 600-nm diameter holes in poly(methyl methacrylate) were patterned via electron-beam lithography. Subsequent evaporation and liftoff yielded 30-nm thick alumina discs that served as an etch mask. Reactive ion etching of the surrounding silicon surface produced 3-μm tall silicon nanowires that were then thinned down via thermal oxidation and wet chemical etching. The silicon surface was next passivated with thermally grown SiO_2 (20 ~ 40 nm in thickness). Selective metallization of the nanowire tips was achieved by spinning a thin layer of photoresist (500 nm, Shipley 1805) so as to leave the nanowires' tips exposed. After the tips' oxide layer was stripped with buffered HF, the exposed silicon was metalized with 10 nm of Ti followed by 50 nm of Au via sputtering and liftoff. To improve contact resistance, the VNEAs were annealed at 250^{o}C in nitrogen. Subsequently, stimulation/recording pads were made independently addressable by first defining electrode tracks using photolithography and then etching away the interstitial regions via RIE. These tracks were then passivated via atomic layer deposition of a 100-nm layer of Al_2O_3. The Al_2O_3 layer covering the nanowires was removed via photolithography and selective wet chemical etching (TransEtch-N, Transene). Finally, a metal contact pad (50 nm Ti/50 nm Au) was added to each electrode track to facilitate electrical interfacing to our measurement setup.

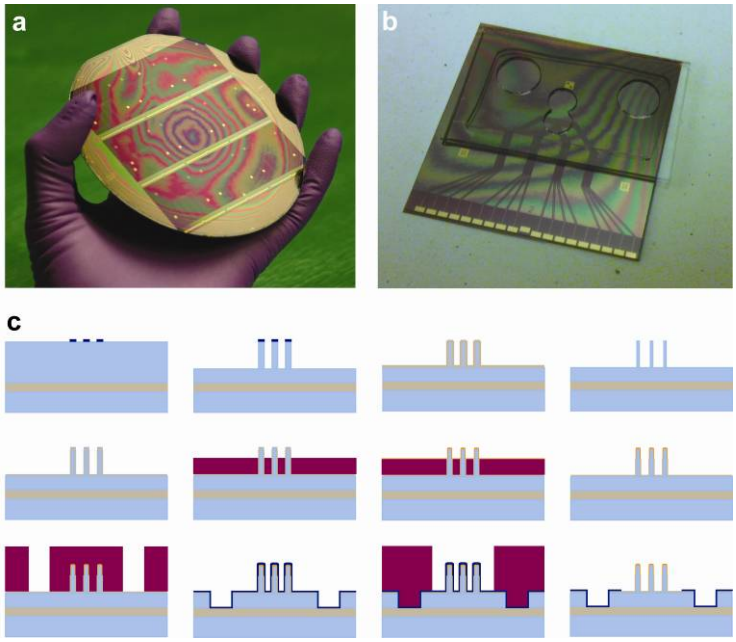

Figure 3.1 | VNEA device fabrication. (**a**) Image of a set of 9 completed VNEA devices, fabricated in parallel on a 4-inch SOI wafer. (**b**) Image of a representative VNEA device consisting of 16 stimulation/recording pads and a polydimethylsiloxane (PDMS) washer with three cell-culture wells: a central double well that surrounds the active region of the device and two additional wells that hold neurons for media conditioning. (**c**) Device fabrication process flow. Briefly, from left to right, then top to bottom: devices were fabricated on an SOI wafer with degenerately doped silicon device and handle layers (cyan) and a 2 – 4 μm thick buried oxide layer (gray). Electron-beam lithography, followed by aluminum evaporation and liftoff, yielded 600-nm diameter aluminum discs (blue) at positions intended for nanowire fabrication. The aluminum discs served as a hard mask for RIE, yielding arrays of silicon nanowires. The nanowires were then thinned down via thermal oxidation and wet chemical etching to obtain diameters of 150 nm. Next, SiO_2 (gray, 20 - 40 nm in thickness) was grown thermally, and a thin layer of photoresist (red) was spun on top, leaving the nanowire tips exposed. Oxygen plasma cleaning and buffered oxide etch were used to remove the SiO_2 covering the nanowire tips. Immediately following oxide removal, the sample was sputter-coated with metal (yellow). Subsequent liftoff yielded metal caps only at the nanowire tips. Next, photoresist was patterned to define the electrode tracks used to address the nanowires, and the interstitial silicon was etched away using RIE. The entire device was then insulated using an Al_2O_3 layer (blue). The Al_2O_3 layer covering the nanowires was then removed using selective wet chemical etching followed by removal of the photoresist.

Figure 3.2 shows a prototype VNEA with 16 stimulation/recording pads. The entire device was fabricated from a silicon-on-insulator (SOI) substrate so that each pad could be independently addressed electrically. At the center of each stimulation/recording pad lies a 3 × 3 array of 9 silicon nanowires (~150 nm in diameter, 3 μm in length, at a 2-μm pitch). Each

nanowire in the array consists of a degenerately doped silicon core encapsulated by a silicon dioxide (glass) shell, and is capped with a sputter-deposited metal tip (Ti/Au: see Fig. 3.2a): the silicon core and metal tip provide electrical access to the cell's interior, whereas the glass shell plays the dual role of preventing current leakage through the nanowire sidewalls and serving as a material for making tight seals to the cell membrane[60]. The geometry of each nanowire array (a 4-μm square) was chosen to be smaller than the size of a typical neuronal cell body so as to increase the probability of single-neuron coupling.

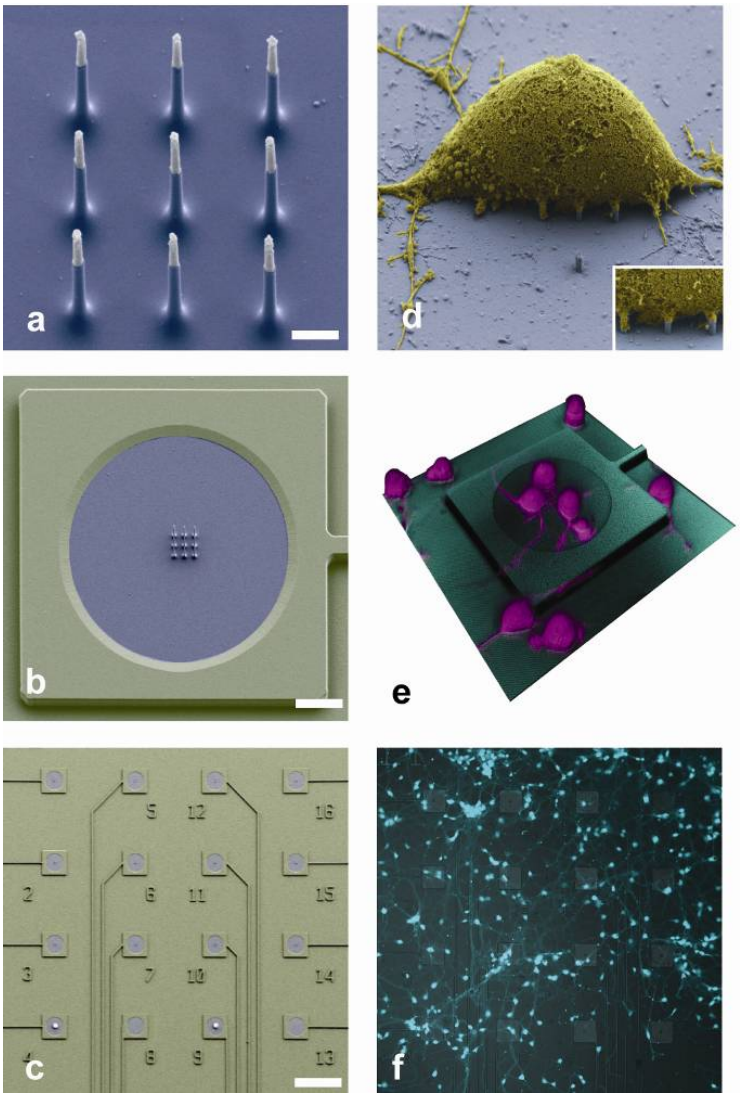

Figure 3.2 | Vertical nanowire electrode array (VNEA) for interrogating neuronal networks. a, Scanning electron microscope (SEM) image of the 9 silicon nanowires that

Figure 3.2 (Continued). constitute the active region of a VNEA. Dimensions of the nanowire electrodes were designed to facilitate single-cell intracellular electrical coupling. False coloring shows metal-coated tips (*gray*) and insulating silicon oxide (*blue*). Scale bar, 1 μm. **b**, SEM image of a VNEA pad. False coloring indicates additional insulation by Al_2O_3 (*green*). Scale bar, 10 μm. **c**, SEM image of a device consisting of 16 stimulation/recording pads for parallel multi-site interrogation of neuronal circuits. Scale bar, 120 μm. **d,** SEM image of a rat cortical cell (3 days *in vitro* (DIV), false colored *yellow*) on top of a VNEA pad (false colored *blue*), showing nanowires interfacing with the cellular membrane (inset). **e**, Reconstructed three-dimensional confocal microscope image of rat cortical neurons cultured on a VNEA pad (3 DIV). **f**, Representative optical microscope image of calcein AM-labeled rat cortical neurons (cyan) cultured on a VNEA (5 DIV).

The top-down nanofabrication technology employed here enables precise control over the physical dimensions of the nanowires, as well as the size and the configuration of the stimulation/recording pads. Moreover, the number of pads can easily be scaled up to the thousands. By virtue of its planar integrated geometry, the VNEA is well suited for studying *in vitro* dissociated neuronal circuits and quasi-2D *ex vivo* preparations, like brain slices or retina. It can also be readily coupled with fluorescence microscopy[44,115], optogenetic techniques[50], and conventional patch measurements[60], allowing truly multiplexed interrogation of neuronal circuits. As an example, Fig. 3.2f shows a typical network of dissociated rat cortical neurons on top of a VNEA after five days *in vitro* (DIV). Images obtained via confocal microscopy demonstrate that the neurons sitting directly on top of the nanowires envelop them and, at times, appear penetrated (Fig. 3.2e and Fig. 3.3). Meanwhile, whole cell patch clamp measurements show that neurons cultured on the VNEAs have similar electrophysiological characteristics as those cultured on glass cover slips, as previously observed[89].

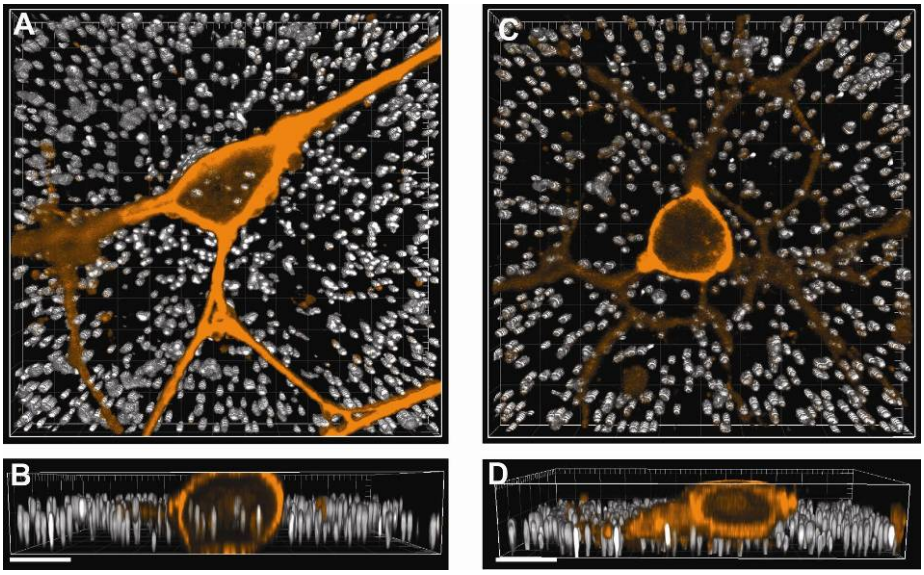

Figure 3.3 | Nanowire penetration of neuronal cell membranes. Three-dimensional confocal reconstructions show that the membranes of some neurons (orange) appear penetrated by nanowires (white) (**A, B**), while others appear to rest on top of the nanowires (**C, D**).

3.3 Optimization of Operation Protocols

We optimized operation protocols for our VNEA devices using HEK293 cells as a model system. HEK293 cells are advantageous for establishing stimulation and recording procedures because they require a short culture time before electrical interrogation (only a few hours), and their membrane resistance remains constant within 15 mV of the resting membrane potential[116]. To determine the device parameters that characterize the VNEA-cell interface, we performed whole-cell patch-clamp recordings of HEK293 cells residing directly on top of the nanowires and monitored voltages and currents simultaneously using both a patch pipette and a VNEA pad (Fig. 3.4a). In more than half of the cases, the membrane potential changed immediately upon VNEA current injection, suggesting that the nanowires had spontaneously penetrated the cell's membrane. When the membrane potential of a cell did not change significantly upon current injection (i.e. when the nanowires were not inside the cell), we used a short voltage pulse (~ ±3

V, 100 ms duration) to permeabilize the cell membrane[117] and promote nanowire penetration (see Methods).

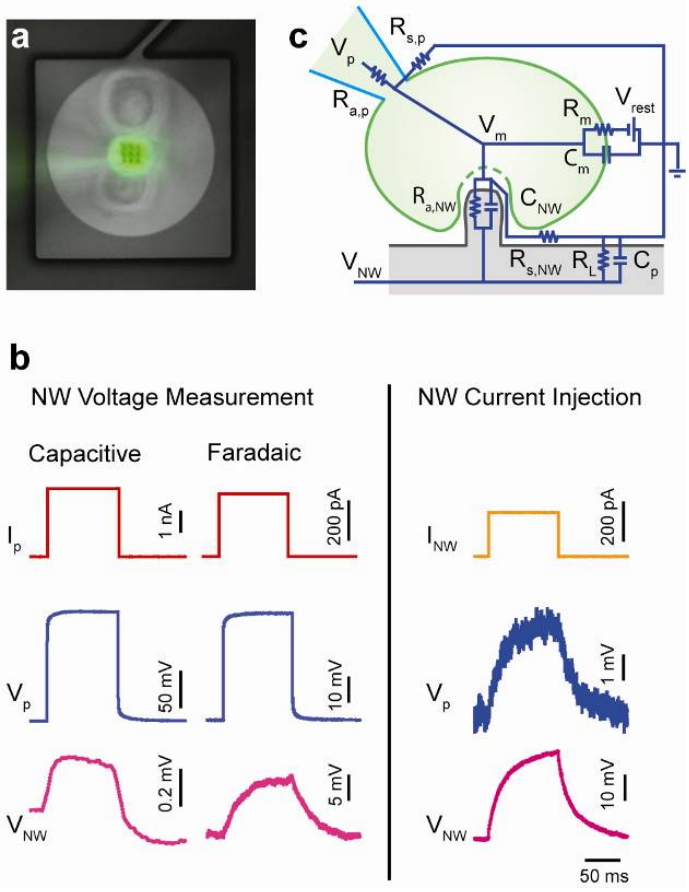

Figure 3.4 | Characterization of the VNEA-cell electrical interface. a, Composite bright field and fluorescence image of a patched HEK293 cell on a VNEA pad (0 DIV). Calcein (green) was added to the intracellular recording solution to enable fluorescence imaging of the patched cell. **b**, In both capacitive and Faradaic modes, the voltage response of the cell due to pipette current injection (I_p) (red) was recorded simultaneously using a patch pipette (V_p, blue) and a VNEA pad (V_{NW}, magenta). Similarly, the cell's membrane potential could be controlled (as verified by patch pipette recordings) by injecting current through the nanowires (I_{NW}) (orange). Note that capacitive and Faradaic measurements were performed on different cells since switching between recording modes required swapping amplifier electronics. **c**, Equivalent circuit model of the VNEA-cell interface. $R_{a,NW}$ and $R_{s,NW}$ ($R_{a,p}$ and $R_{s,p}$) represent the access and seal resistances for the nanowires (pipette), respectively. The capacitance of the electrical double layer at the nanowire surface is represented as C_{NW}. The equivalent circuit also includes the leak resistance due to uncoupled nanowires or defects in electrode insulation (R_L) and the parasitic capacitance due to the device and associated electronics (C_p). The cell itself has a characteristic membrane resistance (R_m), capacitance (C_m) and resting potential (V_{rest}), all of which combine to determine

Figure 3.4 (Continued). the potential across the cell membrane (V_m). The values of these circuit elements were determined based on simultaneous patch pipette and VNEA measurements such as those shown in b.

Once the nanowires had access to the cell's interior, the VNEA device was used to measure and control the cell's membrane potential (V_m) by leveraging electrochemistry at the nanowire tips. Specifically, when no voltage was applied to the nanowires, the change in V_m induced by the patch pipette led to a change in the nanowire voltage (V_{NW}) due to the charging/discharging of the electrical double layer at the metal-coated nanowire tips (the "capacitive" regime: Fig. 3.4b left column). Changes in V_m could also be recorded by applying a bias (~ -1.5V) to the nanowires that was sufficient to flow a small electrochemical current – in this "Faradaic" regime, the value of V_{NW} required to maintain a fixed current tracked the changes in V_m, in a fashion similar to conventional current-clamp techniques[60] (Fig. 3.4b center column). Finally, when current was injected through the nanowires, the voltage measured at the patch pipette (V_p) changed (Fig. 3.4b, right panel and Fig. 3.5), indicating that NW-based control over the membrane potential is also possible (we note that because the nanowires provide only a small point source of current, changes to the membrane potential may not be uniform throughout the cell). In the Faradaic regime, when current was injected through the pipette (nanowire), voltage changes measured at the nanowire (pipette) were ~3 (~10) times smaller than those measured at the pipette (nanowire). In the capacitive regime, on the other hand, V_{NW} was ~300 times smaller than V_p.

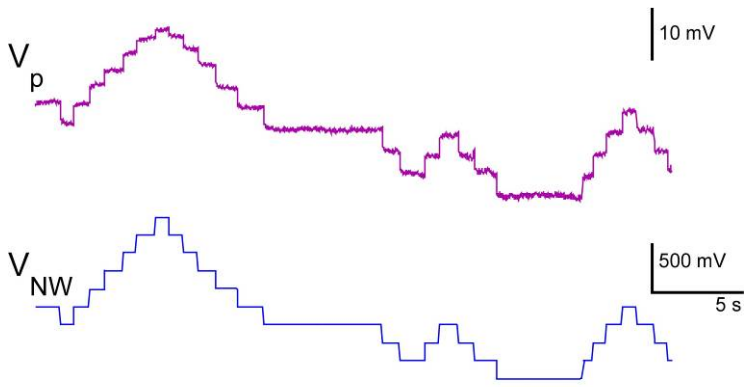

Figure 3.5 | Steady state control of the membrane potential. The membrane potential in a 0DIV HEK293 cell recorded via patch pipette (V_p, magenta) can be controlled by changing the offset voltage applied to the nanowire electrode (V_{NW}, blue)

During capacitively coupled measurements, V_p typically rose by ~10 mV from the initial resting potential after 30 minutes of recording. Such a rise was common even for patch pipette recordings without nanowire penetration, suggesting that the duration of our measurement was limited not by the nanowire recording but rather by effects from patching. During capacitive measurements, a reduction in the signal amplitude measured at the nanowires was also observed over the course of few minutes, indicating partial recovery of the permeabilized membrane. However, this signal could be repeatedly restored to full strength by reapplying the permeabilization protocol. In the Faradaic regime, no signal reduction was observed, likely due to the constant current flow at the nanowire tips. It should be noted that, unlike capacitive measurements, the continuous recording time in the Faradaic regime was typically limited to less than 10 minutes, most likely due to prolonged electrochemical reactions damaging the cellular membrane. By performing measurements intermittently, however, the interrogation period could be extended significantly.

3.4 Equivalent circuit analysis of the VNEA-cell interface

Analysis of the current/voltage traces measured at the patch pipette and the nanowire (Fig. 3.4b and Fig. 3.6) using the equivalent circuit model in Fig. 3.4c enabled the determination of all of the parameters that specify the electrical coupling between the cell and the nanowires. In particular, this analysis showed that the seal resistance ($R_{s,NW}$) between the nanowires and the cell membrane ranged between 100 and 500 MΩ, and the total double-layer capacitance at the nanowire tips (C_{NW})[118] was typically ~1 pF. The nanowire access resistance ($R_{a,NW}$), which includes the intrinsic nanowire resistance and the resistance at the electrochemical junction and thus varies with V_{NW}, was determined to be infinite at zero bias (no electrochemical reactions occurs at the metal tips) and ~300 MΩ at V_{NW} ~ -1.5 V. When the measurement was performed in the Faradaic regime, this large $R_{a,NW}$, combined with the parasitic capacitance (C_p) of a typical VNEA pad and its associated electronics (~150 pF), resulted in an RC time constant on the order of 10 ms. Although this RC component filtered the voltage waveform measured at the nanowires (as compared to that measured at a patch pipette), this distortion could be easily corrected using a deconvolution procedure (Fig. 3.6, 3.7). In the capacitive regime, the change in V_{NW} originated from the charging and discharging of the electrical double layer and thus accurately followed fast changes in V_m. The magnitude of this response, however, was attenuated due to capacitive voltage division (~C_{NW}/C_p).

Herein we depict in more details how the values of the circuit elements shown in Fig. 3.4c were determined using the input impedances of the patch pipette and the VNEA pads, as well as the electrical coupling between the two. After forming a seal with the patch pipette (prior to membrane rupture), the pipette seal resistances ($R_{s,p}$) were measured to be >2 GΩ based upon the steady state current resulting from 10 mV test pulses applied to the patch pipette. The pipette

access resistance ($R_{a,p}$), membrane resistance (R_m) and membrane capacitance (C_m) were then measured from transient current responses to 10 mV test pulses after rupture using the pCLAMP 10 software (Molecular Devices) and Matlab. Values of $R_{a,p}$ were typically between 15 and 30 MΩ, within the normal range for the 5 ~ 10-MΩ patch pipettes used in our experiments. Because this value was small compared to $R_{s,p}$, currents through the pipette seal were neglected from the subsequent analysis. Typical R_m and C_m values for HEK293 cells were between 150 ~ 600 MΩ and 10 ~ 30 pF respectively, consistent with those reported in literature[22].

After obtaining a whole cell patch with a pipette, current injected through the pipette (in the current-clamp mode) and the VNEA were used to determine the values of the remaining circuit elements. The nanowire seal resistance ($R_{s,NW}$) was determined to be 100 ~ 500 MΩ based on the change ($\Delta R_{in,p}$) in the access-adjusted pipette input impedance ($R_{in,p} \equiv [1/R_m + 1/R_{s,NW}]^{-1}$) before ($R_{in,p0}$) and after ($R_{in,p1}$) membrane permeabilization at the nanowire-cell junction (Fig. 3.6):

$$R_{s,NW} = \frac{R_{in,p0} R_{in,p1}}{\Delta R_{in,p}}.$$

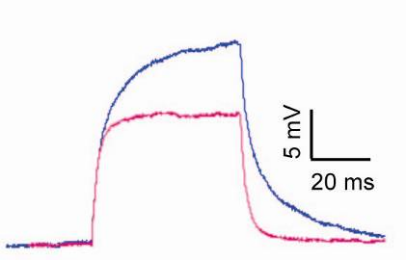

Figure 3.6 | Membrane characteristics before and after permeabilization. Typical voltage response to 50-pA current pulses before (blue) and after (magenta) membrane permeabilization at the nanowire-cell junction. Measurement and stimulation were performed on a HEK293 cell (0 DIV) using a patch pipette in whole-cell current-clamp mode.

The ratio (κ_p) between the pipette voltage change (ΔV_p) and the nanowire voltage change (ΔV_{NW}) during nanowire current injection can be related to the nanowire access resistance ($R_{a,NW}$) and the leak-adjusted nanowire input impedance ($R_{in,NW} \equiv R_{NW} + [1/R_m + 1/R_{s,NW}]^{-1}$) by:

$$\kappa_p = \frac{\Delta V_p}{\Delta V_{NW}} = \frac{R_{in,NW}}{R_{in,NW} + R_{a,NW}}.$$

Note that similar to the pipette access resistance, $R_{a,NW}$ includes the intrinsic nanowire electrode resistance, the resistance at the electrochemical junction, and the resistance through the permeabilized membrane interface.

Meanwhile, the ratio (κ_{NW}) between ΔV_{NW} and ΔV_p during current injection via the pipette can be related to $R_{a,NW}$ and the VNEA leak resistance R_L (either through defects in electrode insulation or uncoupled nanowires) by:

$$\kappa_{NW} = \frac{\Delta V_{NW}}{\Delta V_p} = \frac{R_L}{R_L + R_{a,NW}}.$$

Typical values for κ_{NW} and κ_p in our experiments were 0.2 ~ 0.5 and 0.04 ~ 0.1, respectively. From these measured values, we can calculate the $R_{a,NW}$ and the R_L:

$$R_{a,NW} = \frac{R_m R_{s,NW}}{R_m + R_{s,NW}} \left(\kappa_p^{-1} - 1 \right),$$

$$R_L = \frac{R_{a,NW}}{\kappa_{NW}^{-1} - 1}.$$

$R_{a,NW}$ and R_L typically ranged between 0.3 and 1.5 GΩ, consistent with the total nanowire input impedance $R_t \equiv R_{NW} + [1/R_L + 1/R_{in,NW}]^{-1}$ measured experimentally. Note that due to electrochemical reactions at the nanowire tip, $R_{a,NW}$ is a nonlinear function of V_{NW}, and the value presented above represents those determined at a typical operating voltage of -1.5 V with respect to the bath electrode.

RC time constants of the VNEA measurement setup

Bare nanowire RC time constants were measured as follows. At the conclusion of a recording session, the patched cell was removed from the recording pad by slowly withdrawing the patch pipette. The current flowing through the nanowires was then increased by 200 pA for 300 ms and the corresponding voltage change was recorded. The transient portion of the response could be well described by a single exponential with a time constant between 5 and 50 ms. We determined the nanowire resistance from the steady-state potential difference at the two nanowire currents. Dividing the exponential time constant by this resistance yielded the value of the parasitic capacitance (C_p), which was typically 150 pF. We determined the parasitic capacitance of our current-clamp electronics to be 50 pF by applying the same protocol using a 1 GΩ load resistor.

Using the measured RC time constant of a VNEA pad, we could deconvolve voltage waveforms measured by the VNEA pad and recover true membrane potential waveforms. As an example, we used a model action potential (AP) waveform to control the membrane potential of a HEK293 cell. The time-averaged VNEA recording is shown in Fig. 3.7. To recover the original waveform, we rescaled the measured signal according to the measured coupling constant (κ_{NW}) and performed a Weiner deconvolution in Matlab using the measured time constant of 9.3 ms. The deconvolved VNEA measurements showed good agreement with the original waveform applied to the pipette (Fig. 3.7).

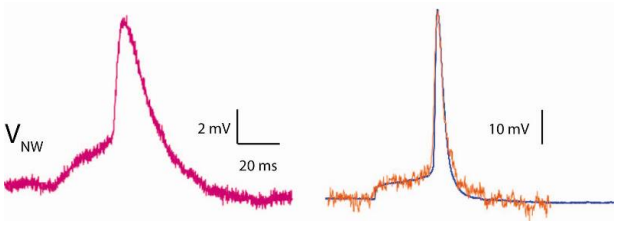

Figure 3.7 | Deconvolution of VNEA measurements. A model AP waveform generated via a patch pipette is measured using the VNEA in current-clamp mode (magenta). Deconvolution of

Figure 3.7 (Continued). the VNEA measurement (orange) shows good agreement with the waveform applied at the patch pipette (blue). Plots are averaged over 5 recordings.

3.5 High-fidelity Intracellular Stimulation and Recording of Rat Cortical Neurons

Once the device characterization and protocol optimization were complete, we utilized the VNEA to perform high-fidelity intracellular stimulation and recording of rat cortical neurons (Fig. 3.8). Typically, these neurons were interrogated after 6 to 14 DIV to allow electrophysiological development and the formation of synaptic connections[119,120]. As shown in Fig. 3.8c, current pulses injected into neurons via the nanowires reliably evoked neuronal action potentials (APs) as recorded via simultaneous whole-cell patch clamp. The stimulation probability followed a sigmoidal dependence on the magnitude of the nanowire-injected current (Fig. 3.8b), similar to that reported for patch pipette stimulation[121]. Moreover, the VNEA operating in current-clamp mode could be used to monitor individual APs evoked by the patch pipette. For single-shot AP measurements, the signal-to-noise ratio for VNEA recordings was typically 100 or greater (Fig. 3.8d). When we averaged multiple waveforms obtained under identical experimental conditions, we could improve the signal-to-noise ratio to >1000 (Fig. 3.7). This suggests that by averaging the response to repeated presynaptic stimulations, postsynaptic potentials (PSPs) could be measured using the VNEA.

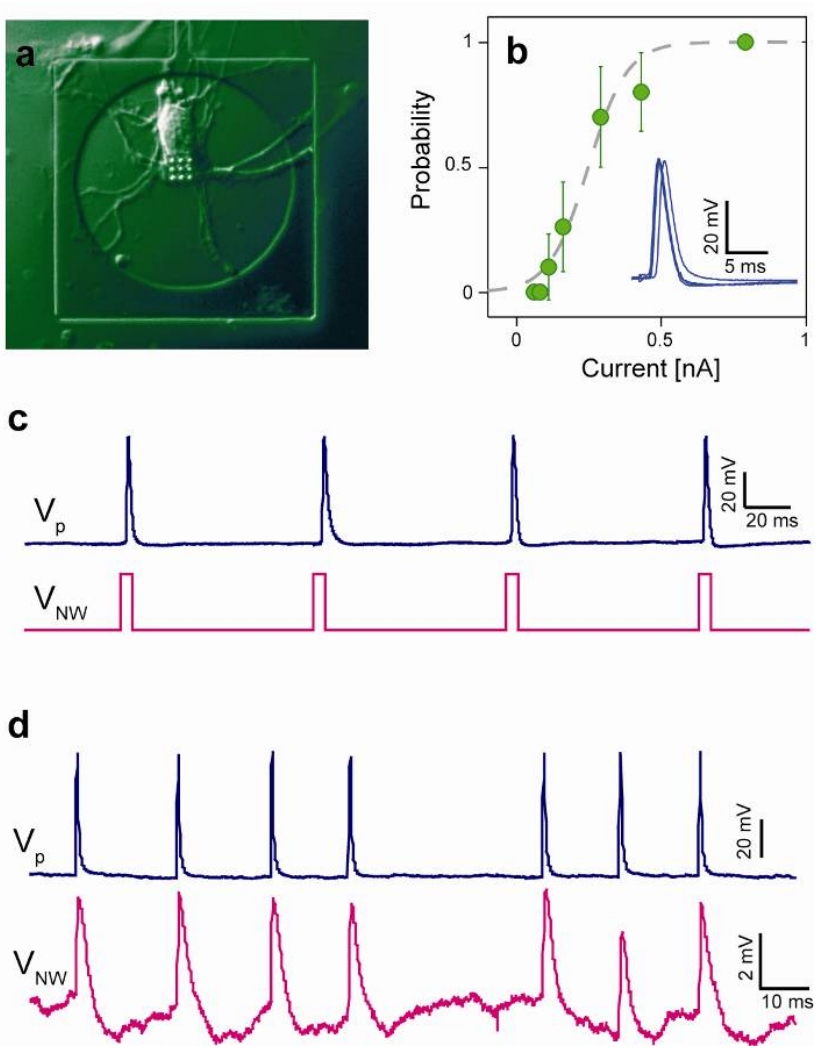

Figure 3.8 | Stimulation and recording of rat cortical neurons using a VNEA. a, Representative differential interference contrast micrograph of a rat cortical neuron cultured on a VNEA pad (6 DIV). **b**, Probability of action potential (AP) excitation plotted as a function of current injected by nanowires shows a sigmoidal dependence (dashed line), which is similar to AP excitation elicited via intracellular patch pipettes. Probabilities were calculated for 20 trials and plotted as a function of the stimulation current. Error bars represent 95% confidence intervals. **inset**, 5 consecutive time-aligned APs stimulated by nanowire current injection show less than 1-ms jitter. **c**, APs were reliably stimulated by voltage pulses at the VNEA pad (magenta) and recorded using a patch pipette (blue). **d**, Similarly, APs were stimulated using a patch pipette (blue) and recorded by the VNEA pad in the Faradaic mode (magenta). VNEA measurements show good agreement with those obtained simultaneously via patch pipette.

3.6 Functional Connectivity in Neuronal Circuits

The multiplexed stimulation and recording capabilities of the VNEA platform and its compatibility with conventional patch-clamp and fluorescence microscopy techniques enable comprehensive examination of the functional connectivity in neuronal circuits beyond traditional connected-pair studies[122]. To illustrate the potential of such measurements, we used our VNEA platform to map multiple individual synaptic connections onto a single postsynaptic neuron. Specifically, we used a patch pipette to measure the PSPs of a single neuron in a dissociated neuronal culture while inducing APs in other neurons using neighboring VNEA pads (Fig. 3.9a). By monitoring PSP responses upon repeated stimulations at each pad, we found that excitation of some of the nearby neurons reproducibly generated either excitatory (EPSPs) or inhibitory PSPs (IPSPs) in the patch-clamped cell (Figs. 9b and 9c). The latency window of these EPSPs and IPSPs ranged from 2 to 8 ms, indicative of a monosynaptic connection[123]. We note that performing this type of measurements using conventional patch clamp techniques would require each pre-synaptic cell to be individually identified and patched separately. Using our VNEA platform, this process can be significantly simplified and expedited. Together, the magnitude, sign, and latency of these PSPs define the functional connectivity of a neuronal circuit. By monitoring changes in this connectivity as a function of time and combining it with structural reconstruction techniques, we should be able to investigate the relationships between the architecture, dynamics, and function of neuronal circuits in unprecedented detail.

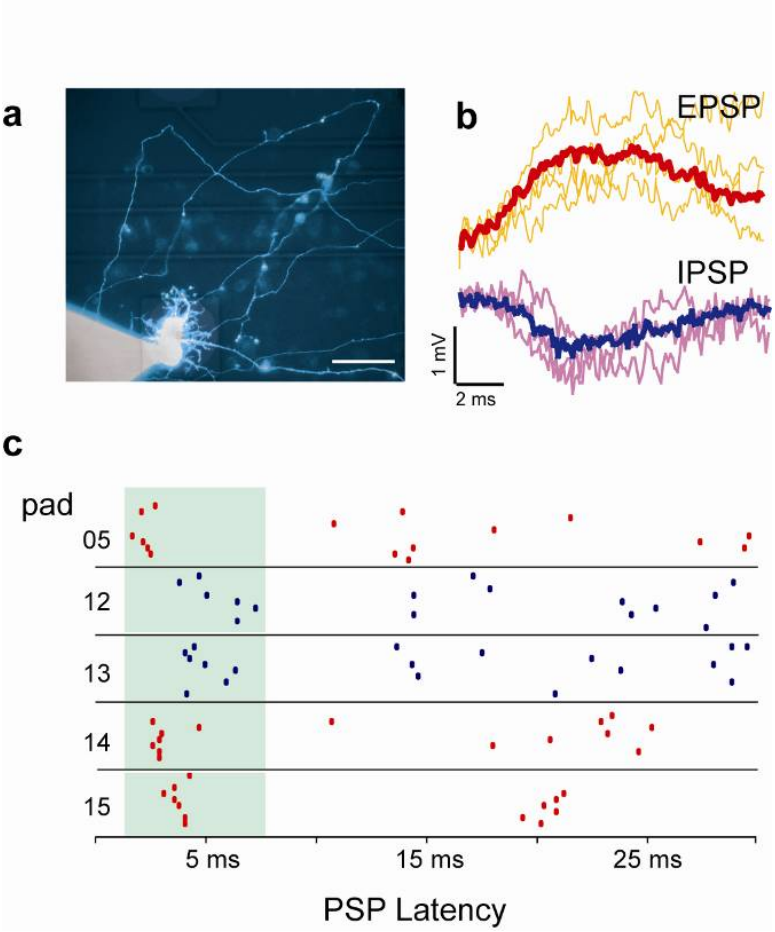

Figure 3.9 | Identification of functional synaptic connectivity using a VNEA and a patch pipette. a, Composite bright field and fluorescence image of a cortical neuron patched and backfilled with calcein (14 DIV). **b,** Representative EPSPs (top) and IPSPs (bottom) were averaged (bold) and used as templates for identifying other PSPs recorded via a patch pipette. To measure these PSP events, we injected a constant current through the patch pipette to hold the membrane potential near -40 mV. At this resting potential, EPSPs and IPSPs produce positive or negative changes in the membrane potential respectively, allowing them to be distinguished from one another. **c,** Raster plots of EPSPs (red) and IPSPs (blue) identified by patch-clamp recording and plotted as a function of their latency following stimulation at the specified VNEA pads. Each of the five pads shown here evoked reproducible PSPs in the patched cell within a latency window of 2 - 8 ms (green), suggesting monosynaptic connectivity.

3.7 Conclusions and Prospects

The present study demonstrates that the VNEA platform provides new experimental methods to stimulate and record neuronal activities in a highly scalable fashion. Moreover the VNEA platform can be readily coupled with conventional patch measurements,

fluorescence microscopy, and optogenetic techniques, allowing truly multiplexed interrogation of a neuronal circuit. Although the prototype demonstrated here has only 16 stimulation/recording sites, higher numbers and densities can easily be achieved using standard silicon nanofabrication processes. For instance, contemporary deep UV lithography with feature sizes near 150 nm can produce recording pad densities approaching 10,000 electrodes/mm^2. The integration of complementary metal-oxide-semiconductor circuitry with a VNEA would further allow on-chip digitization, signal multiplexing, compression, and telemetry. Finally, the small dimensions and planar geometry of VNEAs should facilitate their incorporation into implantable electrodes, similar to the silicon-based microelectrode array implants currently in use[124], opening up new possibilities for neuronal prosthetics and large-scale studies of neuronal circuit dynamics *in vivo*.

CHAPTER 4

CMOS-Nanoelectrode Array: A Fully Integrated Platform to (1) Map and Modify the Functional Connectivity of Complex Neuronal Networks and (2) Enable High-throughput Drug Screening of Neurological Disorders

4.1 Introduction

Our prototype device with 16 recording/stimulation sites demonstrated that vertical nanowire electrode arrays enable direct intracellular electrical access to mammalian neurons in a minimally invasive fashion[127]. The development of the VNEA as a highly scalable intracellular electrode platform paved the way towards novel nanotechnologies that facilitate large scale measurements of the functional connectivity of neuronal networks[114]. To further expand and improve upon this prototype device we

moved towards the development of a fully integrated CMOS-nanoelectrode array (CNEA) that is capable of measuring and controlling a large number of neurons with single-cell resolution. The design of our CNEA aims to generate the new neuro-nanoelectronic interface to: (1) map and modify the functional connectivity of complex neuronal networks *in vitro* and *ex vivo* and (2) screen candidate drug treatments for neurological disorders in a high-throughput fashion.

Advanced CMOS technology has been recognized for its potential and integrated in platforms for neuronal network studies in several configurations; for example, (1) foundry-fabricated CMOS chips with high-density microelectrode arrays for *in vitro* neuronal networks and (2) CMOS chips combined with the Utah MEA for *in vivo* neuronal networks[128-134]. Despite the high-density recording capability characterizing these platforms (up to ~16,000 active sites), neuronal signals were measured only at a small number of sites and were not directly correlated. Being based on extracellular neuronal recordings, these studies were unable to obtain signal-to-cell registry or a detailed description of network dynamics in complex neuronal circuits.

The overall design and aimed functionality of our CNEA device is a significant departure from previous CMOS-microelectrode arrays: unlike the previous devices that performed extracellular recordings, our CNEA will monitor and stimulate signals intracellularly, thereby enabling the unambiguous cell-to-electrode registry essential for functional mapping of large numbers of interconnected neurons[135,136]. The front side of the array features 1024 recording/stimulation sites, each equipped with NWs for neuronal coupling (the length of the NWs will vary from 3 μm for *in vitro* culture studies to 30 μm for *ex vivo* tissue studies, and the site numbers will vary accordingly). The backside of the array will contain the CMOS integrated circuits (ICs) that perform amplification and processing of neuronal signals. In addition, the CMOS chips include the additional circuit that enables each pixel to pass a voltage pulse for stimulating neuronal activity. By applying specific electrical stimulation to each pixel individually, we will be able to excite neuronal networks with a broad range of spatiotemporal patterns. Thus, each recording/stimulation site (pixel) in the array will contain nanowires on top, and a low-noise amplifier, a stimulator, and digital circuits in the underlying IC. The IC will play a critical role

in enabling parallel operation of the nanoelectrode array and will thus propel it as a practical forefront tool in neuroscience. Also, the proximity of the IC to the nanoelectrodes will ensure the sensitivity promised by the intracellular recording. In sum, the CMOS-assisted nanoelectrode array will make possible both parallelism and high-sensitivity intracellular recordings.

4.2 CNEA Top Fragment: Large array of electrically active vertical nanowire electrodes

One of the defining characteristics of our CNEA device is its ability to intracellularly interface with a large number of neurons via its front-side vertical nanowire electrodes. The definition and generation of the front nanoelectrode cellular interface array is achieved via a multi-level and complex nanofabrication process to produce an efficient interface between biological neuronal networks and the underlying electronic circuitry. The complexity of the nanofabrication process is a necessity due to the complementary metal–oxide–semiconductor (CMOS) technology that can withstand full functionality if exposed only to temperatures below 450°C. In addition, the functional goals of the final device layout – a cellular interface that is intracellular, individual, and parallel – further extend the nanofabrication requirements and limitations. Our fabrication process, summarized in Fig. 4.1 below, makes possible the achievement of our ultimate functional aims in parallel to preventing any physical or functional damage to the underlying CMOS chip.

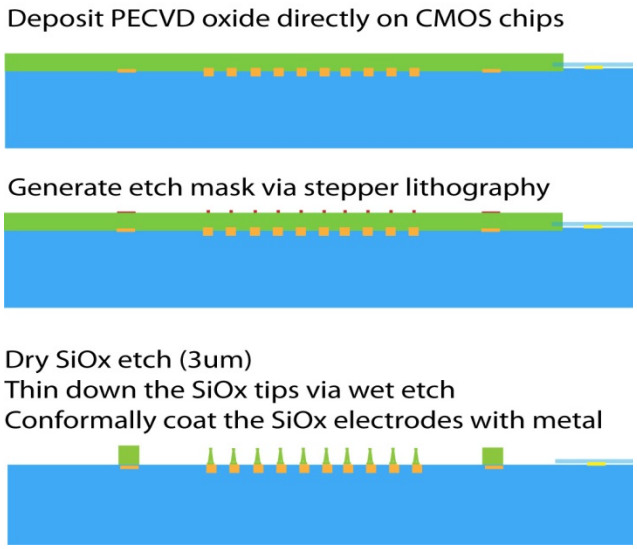

Figure 4.1 | Summarized fabrication process-flow

Initially, to prevent any functional or physical damage to the CMOS chip, we begin the fabrication process by protecting the CMOS exposed Aluminum-metal-layer-4 (Al-4) via sputter deposition of a Titanium (Ti) and Platinum (Pt) metal layer. Our optimally thick and high-resolution Ti-Pt protection layer ensures: (1) inhibition of any chemical attacks of the exposed Al-4 possible during etch processing, (2) prevention of the Al-4 diffusion to the top of the protection layer during high temperature processes, and (3) production of a high-quality underlying material that supports the generation of the top nanowire electrodes by ensuring a good adhesion between the deposited silicon dioxide (SiO_2) and the substrate.

Secondary, to facilitate the generation of high-quality structural material for the nanowire electrodes and prevent any impairment of the CMOS chip we developed a non-standard plasma-enhanced chemical vapor deposition (PECVD) of SiO_2 at a temperature of only 350°C. Our developed PECVD process includes: (1) ensuring a highly clean substrate, (2) stabilizing the chamber vacuum, (3) ensuring a plasma chamber uniformity, (4) establishing a stable plasma prior to the deposition start, and (5) maintaining a low silane to nitrous ratio. To fabricate the vertical nanowire electrode array for interfacing two-dimensional *in vitro* cultures, at the previously determined optimal height, we first deposit 3.5μm SiO_2 via this PECVD process, which gives rise to an excellent uniformity and structural quality material with strong adhesion to the underlying pixel metal.

Consequently, we optimized stepper lithography to allow the generation of the accurately aligned, widely uniform (across the large pixel array), and high quality etch mask. We used the optimized stepper lithography process to generate the array of the etch mask consisting of photoresist discs 1μm in diameter – aligned centrally on top of the active pixel array. Such an etch mask facilitates the generation of the highly uniform array of vertical nanoelectrodes via reactive ion etching (RIE) of the surrounding SiO_2 surface. Once the characteristics of the RIE process were characterized and subsequently improved, we achieved a highly selective and reproducible SiO_2 etching that facilitated the generation of initial vertical structures with high aspect ratio and the designed vertical etch profile. Subsequently, SiO_2 isotropic wet

etching is used to achieve the final structural profile of the vertical nanowire (length, 3μm; diameter, 100nm).

Next, electrical activation of the tips of the vertical nanowire electrodes in addition to conductive connection with the underlying metallized pixel is achieved through selective and conformal metallization. Contact lithography followed by sputtered metallization allows the generation of a uniform metal layer with high conductivity and small grain size. The whole chip is insulated by 20nm SiO_2 and 200nm Al_2O_3 (via atomic layer deposition – ALD) to prevent currents leaking from the metal pads and reduce parasitic capacitance. Selective Al_2O_3 etching via photolithography and wet etching enables us to remove the Al_2O_3 only on nanowires and a small region around it, and stop at the SiO_2 layer. The exposure of the nanowire metal tip is achieved by spincoating photoresist to protect the nanowire base and subsequently wet etching the SiO2 at the selectively exposed tip. The final results of the fabrication process are summarized in Figure 4.2.

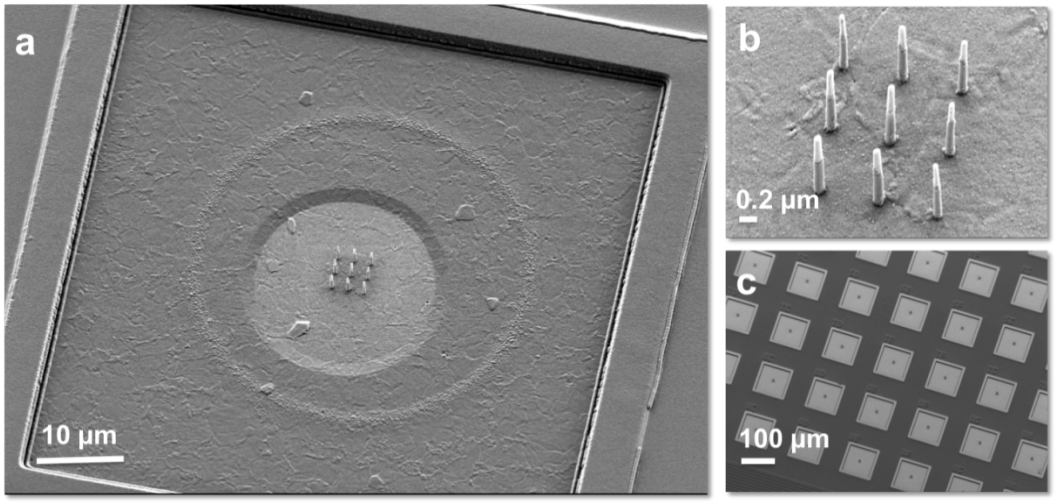

Figure 4.2 | Scanning electron microscope (SEM) images of increasing scale showing vertical nanowire electrodes post-fabricated on each pad.

The design, development, and optimization of our nanofabrication process-flow facilitated the generation of our efficient interface between biological neuronal networks and the underlying electronic circuitry. First, the ultimate profile geometry of the vertical nanowires, shown in Fig. 4.2 a, makes

possible the intracellular interface of individual neurons. Secondly, the electrical properties of these nanoelectrodes (electrochemically active nanowire tips (**color)**, selectively insulated base, and conductively connected to the underlying pixel circuitry) provide the direct electrical access to the cell's interior with minimal effect on cellular viability. Thirdly, Fig. 4.2 c depicts the fabrication of the uniform nanoelectrode array (geometrically and electrically) across the CNEA chip, which allows the generation of 1,024 independently addressable recording/stimulation sites at a 126 μm pitch over a 16 mm^2 area.

4.3 CNEA Underlying Circuitry: CMOS ICs

The backside of the CNEA contains the CMOS circuits that perform amplification and processing of neuronal signals. The implementation of *in situ* amplifiers proximate to the nanowires makes possible the reduction of signal attenuation by eliminating lengthy interconnects. Each pixel records the voltage signal generated by a neuron as detected by the front-side NWs. In addition, the CMOS circuits are designed so that each pixel can pass a voltage pulse for stimulating neuronal activity. By applying specific electrical stimulation to each pixel individually, we will be able to excite neuronal networks with a broad range of spatiotemporal patterns. The underlying CMOS chip of our CNEA devices was designed and fabricated in the 0.35 μm node of Taiwan Semiconductor Manufacturing Company (TSMC), using the high breakdown voltage metal–oxide–semiconductor field-effect transistor (MOSFET) option with top/bottom power rails of ±2.5 V. Individual CNEA chips contain 1024 stimulation/recording sites enabling large-scale interfacing of neuronal networks, with single cell resolution. The CMOS IC design considerations – associated with the required functionality of individual pixel circuitries – determined the pitch between two adjacent recording/stimulation sites to be 126 μm[137]. Thus, the individual 10x10 mm CMOS chip contains a ~ 4x4 mm active area consisting of a 32x32 pixel array as represented in blue in the chip micrograph shown in Figure 4.3b.

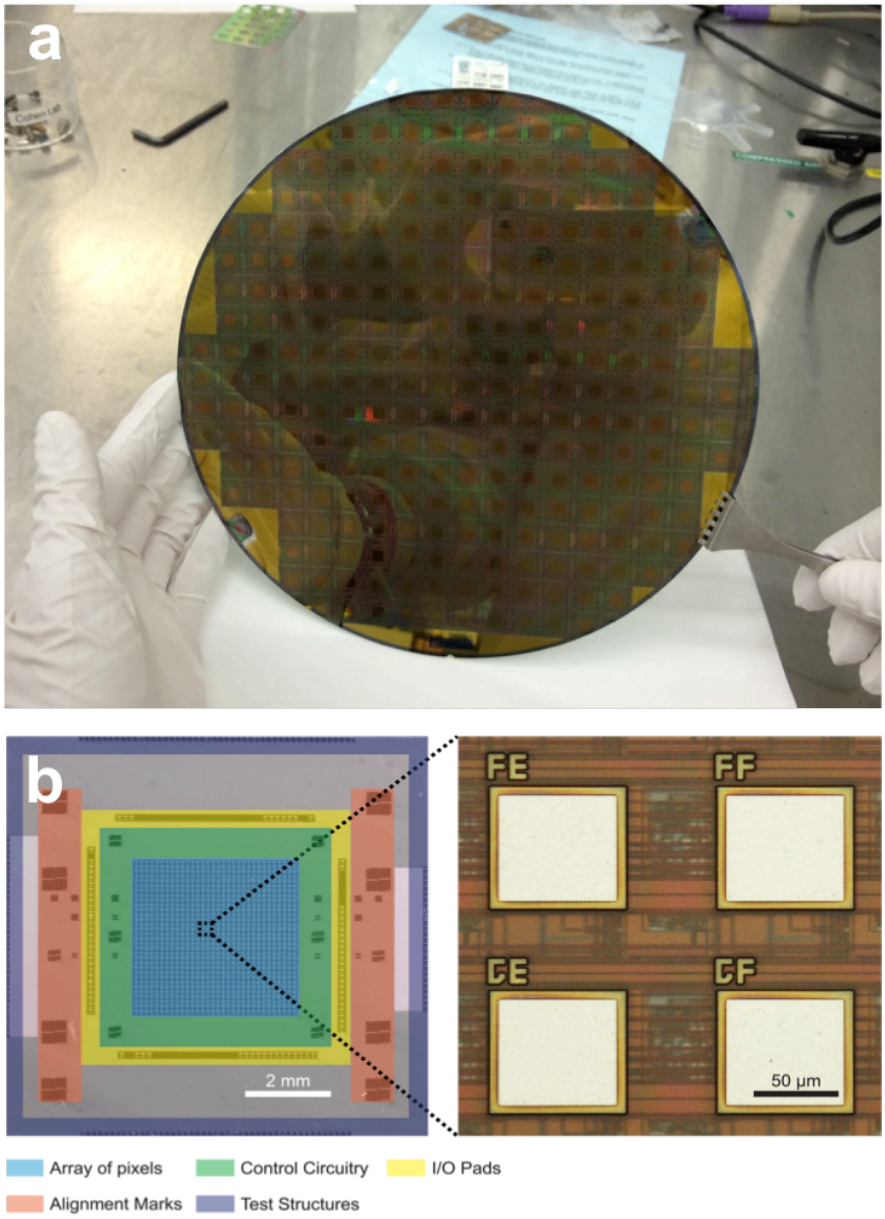

Figure 4.3 | (a) Image showing the 8-inch wafers containing the CMOS chips. (b) CMOS chip micrograph; in the middle is the 32x32 pixel array (represented in blue color); a zoom in of four shown on the right. Control circuitry is then located around the array, which programs the memory at each pixel and run the output multiplexer (green color coded). Further outside, the I/O pads and alignment marks used for post- fabrication (yellow and red, representation).

The IC design goals that determined the overall layout of the active array included: (1) a two-way interface with neurons for both recording and stimulation of electrical activity, (2) high Signal-to-Noise Ratio (SNR) recordings for each of the individual sites, (3) simultaneous, low-energy operation of the

active array for biocompatible and high-throughput interrogation capability of neuronal networks. First, the dual pixel functionality (capability of both stimulating and recording modes) is achieved via two separate circuitries, as shown in the summarized circuit schematic (Fig. 4.4), combined with digital control circuits that enable the activation/deactivation of the selected functional mode. The pixel layout of the CNEA underlying IC shows the optimized design and circuitry arrangement in individual pixels (Fig. 4.4 b).

Stimulation mode

The central components of the stimulation circuitry, colored in blue in Fig. 4.4, consist of an op-amp with a unity gain feedback (a voltage buffer) whose output is controlled by the memory in conjunction with the multiplexer (MUX). The stimulation voltage signals drive the nanoelectrode by the direct injection or draw of a current (no de-coupling capacitor between the stimulator and electrode) directly to or from the neuron through the access resistance (R_a). The stimulation mode circuitry is characterized by a <0.1 ms settling time (faster than the membrane response) and enables stimulating currents over a wide range up to 4 V. Independent control on three variable voltage signals for stimulation on individual pixels enables a wide variety of stimulating schemes for network level studies.

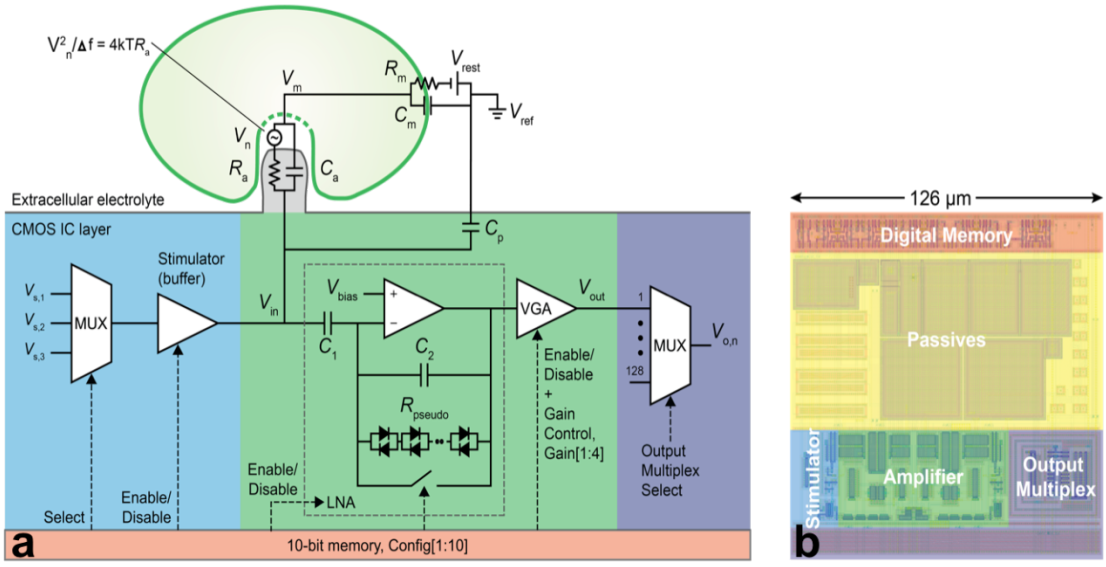

Figure 4.4 | (a) Electrical block diagram**.** Nanoelectrode and underlying pixel circuitry showing equivalent circuit models of the neuronal membrane (membrane potential, V_m, membrane resistance, R_m, membrane capacitance, C_m, and resting potential, V_{rest}) and nanowire-electrolyte interface modeled as a double layer capacitance, C_a, and faradic resistance, R_a, with noise source, V_n, and power spectral density per hertz of bandwidth, $V_n^2/\Delta f$, of $4kTR_a$ (k is Boltzmann's constant and T is temperature). The pixel is composed of the reading amplifier (green/right) and stimulator (blue/left) with digital control circuits (bottom) to allow for enabling or disabling the stimulator or amplifiers, gain, and choice of stimulation signal. (b) Top-view of pixel layout.

Recording mode

The circuitry of the recording mode, detailed in Fig. 4.5, was designed to meet the sensitivity and performance requirements necessary to account for the wide variety of signal properties and to overcome the attenuation and noise generated from several sources. Signal attenuation arises from the properties of the top electrode (from active and parasitic coupling) in combination with the properties of the underlying amplifiers. The nanowire electrode can be modeled with a Faradic resistance, R_a that varies with the electrode's DC current, in parallel with a capacitance, C_a of the electrode/electrolyte double layer formed at their interface. To prevent damage to cell viability, the NWs are operated at zero DC current. In this configuration, we achieve capacitive coupling to the intracellular signals through the double layer capacitance, the impedance of which, $1/(j\omega C_a)$, is on the order of $0.1\ G\Omega \sim 0.1\ T\Omega$ in the

electrophysiological signal bandwidth of 1 Hz ~ 5 kHz[138]. Despite the relatively lower impedance compared to the Faradic resistance (~10 TΩ), capacitive coupling is associated with significant signal attenuation due to voltage division with parasitic capacitances of the metal pad and subsequent interconnects, summed up as C_p (Fig. 4.4). This necessitates an optimal interface with the input impedance of the amplifier to minimize further signal attenuation in addition to an optimized amplifier overall design to facilitate signal amplification well above subsequent transmission noises. Furthermore, the *1/f* amplifiers' noise significantly affects the biological signals due to their low amplitude and low frequency.

To address these challenges, high SNR recordings of electrical signals is achieved via a two-stage amplifier design consisting of (1) a front-end low noise amplifier (LNA) and (2) variable gain amplifier (VGA) (Fig. 4.5, right). Each of the LNA and VGA consists of a single-ended two-stage operational amplifier topology with a minimal number of transistors to reduce overall 1/*f* noise contribution from the circuit. The overall two-stage amplifier acts as a bandpass filter (closed-loop configuration with a passband gain of C_1/C_2), with a bandwidth 0.1 Hz – 5 kHz including the wide frequency range associated with the biological signals while filtering out most low-frequency 1/*f* noise and high-frequency noise beyond 5 kHz[139]. Turning on the recording mode results in the simultaneous activation of the first and second stage of LNA via the two current sources I_1 and I_2 in addition to activating and setting the VGA similarly. The front-end amplifier (stage 1) is an op-amp with a negative feedback loop and with an AC-coupled input to the top nanowire electrodes. AC coupling the front end of the amplifier to the nanowire electrodes, through C_1 = 200 fF, generates a high nanowire faradic resistance (~TΩ, Teraohms), thus preventing any direct currents in recording mode. The nanowire electrode is portrayed by the capacitor generated by the double layer formed between the nanowire electrode and cellular electrolyte (C_a, 10-100fF). The implementation of these capacitive measurements enables long-term recording capabilities by eliminating any cellular damage caused by continuous current injections/draws.

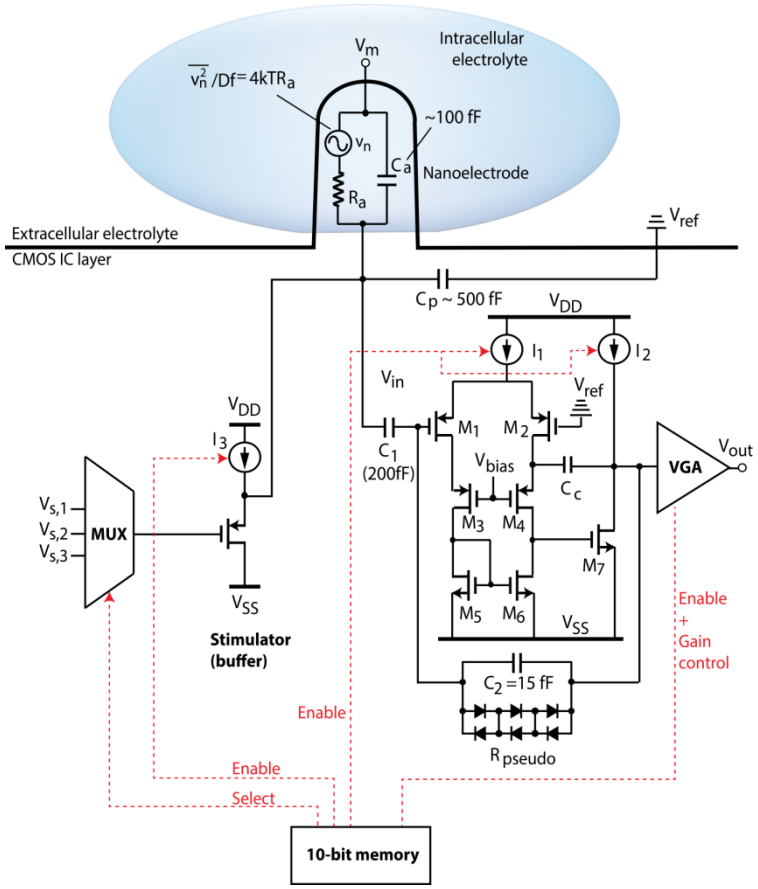

Figure 4.5 | Detailed schematic of the pixel circuitry with nanoelectrode. In addition to the noise produced by the amplifier, the nanoelectrode's resistance produces noise that is referred to the input of the amplifier. To accomplish a low frequency pole to reduce low frequency *1/f* noise, a pseudo resistance composed of diodes is used in the feedback path allowing for greater than teraohm resistance or less than a 0.1 Hz pole.

The op-amp, internally, consists of a two-stage configuration with the first differential and second single-ended stage assuming a common-source topology with active loads. Input transistors (M_1 and M_2) are p-type metal-oxide-semiconductor (PMOS) transistors; they are chosen because of their smaller *1/f* noise compared to the typical n-type metal-oxide-semiconductor NMOS transistors, as PMOS transistors are built in n-wells that isolate the amplifier input from substrate noise. Furthermore, their configuration suppresses noise that is generated from fluctuations in the top power rail, V_{DD} = 2.5 V. Additional noise, generated via fluctuations in the bottom power rail V_{ss} = -2.5 V, is suppressed through the cascode transistors (M_3, M_4) at the amplifier output. Even though the cascoding configuration introduces another bias line (V_{bias}), it draws no current, thus a stable voltage reference can make it quiet.

On the other hand, the negative feedback loop contains a high-pass filter – a diode pseudo resistor (R_{pseudo}) in parallel with a poly-insulator-poly capacitor (C_2) defining a 5-Hz 1-pole cutoff. It filters *in* most spectral contents of the electrical activity of cells to enable high fidelity in signal acquisition, while at the same time it filters *out* DC drifts and near-DC *1/f* noise to prevent saturation of subsequent amplifiers. The incorporation of the pseudo resistance composed of a series of diodes, which provides a very high resistance within the limited pixel area, enables the creation of the low frequency pole. Additionally, the negative feedback loop sets the bias for the gate of input transistor M_1 at V_{ref} (the gate of M_2 is directly biased at V_{ref}). The array is split (top and bottom) using two different LNA amplifiers; the top half LNA has a measured passband voltage gain of ~20 V/V by design while the bottom half LNA is ~8 V/V.

The second stage of the recording-mode circuitry consists of a VGA with the double role of (1) enabling high SNR of the wide electrical signal range for routing off the chip for data acquisition, and (2) providing low-pass signal filtering with a 10-kHz 1-pole cutoff, suppressing any noise above the sampling rate. It has a designed digitally tunable measured gain (4 bits, Gain [1:4]) from ~1.25 V/V to ~20 V/V with an increment of ~1.25 V/V to adjust signal dynamic range. Adjusting the VGA's gain through a control voltage facilitates two extreme case scenarios: at its highest settings the recording of low magnitude signals (PSP ~ 1mV) and at its lowest settings the large magnitude signals (APs ~ 100mV) without causing saturation. In addition, by providing this variability in voltage gain, it allows adjusting for signal attenuation resulting from variability in the top nanowire electrodes as well as their interface with the biological cells.

The pixel operational mode and variability is controlled through a 10-bit digital memory. The 10 static random-access memory (SRAM) cells store rewritable data that define the overall operational settings of individual pixels. First, they define the pixel operation mode into recording, stimulation, or off through enabling/disabling specific amplifiers. Second, they select the specific stimulus to define the particular stimulation experiment. Third, they set the gain of the VGA to control the overall signal amplification in recording mode, thus accounting for attenuation variations from pixel to pixel.

4.4 Overall Experimental Set-Up

Device packaging for culture compatibility

Specialized packaging technology was developed to generate the final experimental platform for cell culture compatibility, leaving exposed the nanoelectrode array while completely isolating the rest of the electrically active components. Individual chips are mounted on ceramic chip-carriers through low-height wire bonding to allow for the subsequent high-quality encapsulation. Next, a square Si ring (0.5 mm high and 0.5 mm wide) surrounding the active central array area is attached via biocompatible epoxy to form the main chamber for cellular culture directly on top of the active array. A larger glass ring (outer diameter 34mm, width 3mm, height 5mm) is used to form the chamber for media supplement. Subsequently the wire bonds located in the region between the inner (Si) and the outer (glass) rings are encapsulated with PDMS to completely isolate them from the highly conductive medium. The material arrangement of the overall chip package allows the generation of a substrate fully supportive of viable cellular cultures while the structural design facilitates complete compatibility with standard electrophysiological setup including patch clamp and fluorescent imaging (Fig. 4.6).

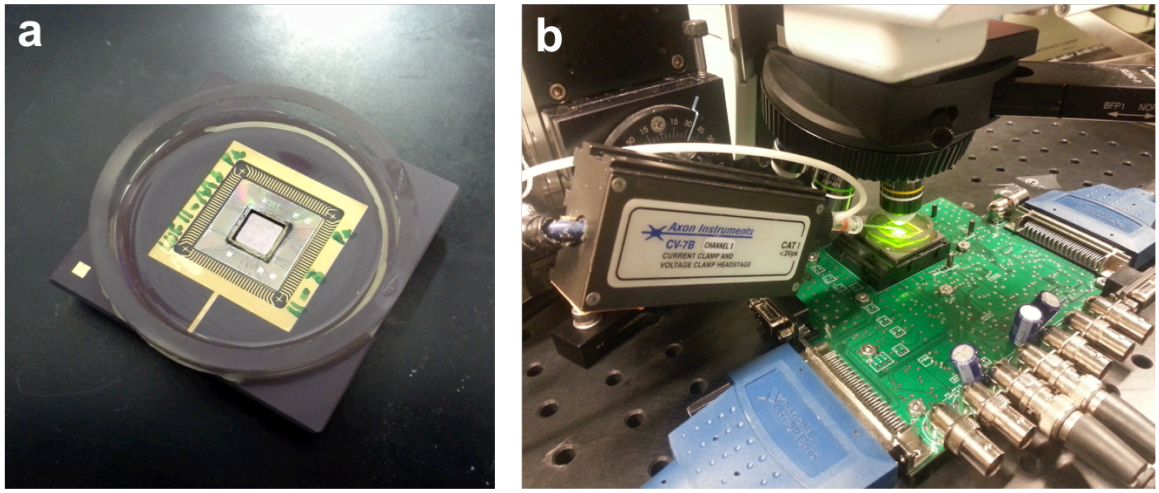

Figure 4.6 | Packaging: (a) CMOS-nanowire array chip is wire-bonded to a chip carrier; a glass ring and PDMS flowed over the wire-bonds create a microfluidic well for cell culture. (b) Experimental setup including the packaged CMOS-nanowire array chip, custom designed PCB, patch clamp, and fluorescence microscope.

Printed circuit board (PCB), external circuitry and software

The fully packaged device on the chip carrier is inserted into a custom designed PCB connecting to further downstream electronics, thus facilitating control and optimization of its overall functionality. Using a data acquisition card (DAQ, National Instruments PXIe-6358) connected through the PCB, the pixel's digital memory is programmed and the analog output multiplexers are controlled (allowing for a pixel to be addressed and directly connected to the output, which enables an individual pixel to be sampled at a much higher sample frequency if desired). The PCB itself contains analog buffers, programmable low noise voltage supplies, and a current-sensing circuit. The analog buffers are integrated to further buffer the eight analog outputs from the array before they are routed to the analog to digital converter (ADC) of the DAQ card. The low noise voltage supplies for the IC provide the chip with power signals, V_{dd} and V_{ss}, and reference voltages used in the amplifier design. The chip ground, V_{ss}, is digitally programmable from -5.0 V to +5.0 V with 1 mV accuracy with respect to solution's reference electrode biased at earth ground; V_{dd} (fixed +5.0 V to V_{ss}) and the reference voltages (digitally programmable with 0.5 mV accuracy) are then referenced to V_{ss}. As a result, the stimulation buffer at the pixel is able to achieve both positive and negative voltage stimulation with respect to the reference electrode. This configuration also ensures that all source/drain-to-body diodes of the CMOS transistors connected to the nanowires remain reversed biased and unconducting. To measure the current through the reference electrode immersed in the solution, a digitally programmable inline current sensing circuit is used with four current sensitivities (0.1 nA/V, 1 nA/V, 10 nA/V, and 100 nA/V) and read by the DAQ's ADC, allowing for positive and negative current measurements from ~1 pA to 1 μA. All circuitry on the PCB and IC are programmed and read through the DAQ card and interfaced by the user through a real-time custom Labview software, along with the microscope, manipulators, and camera.

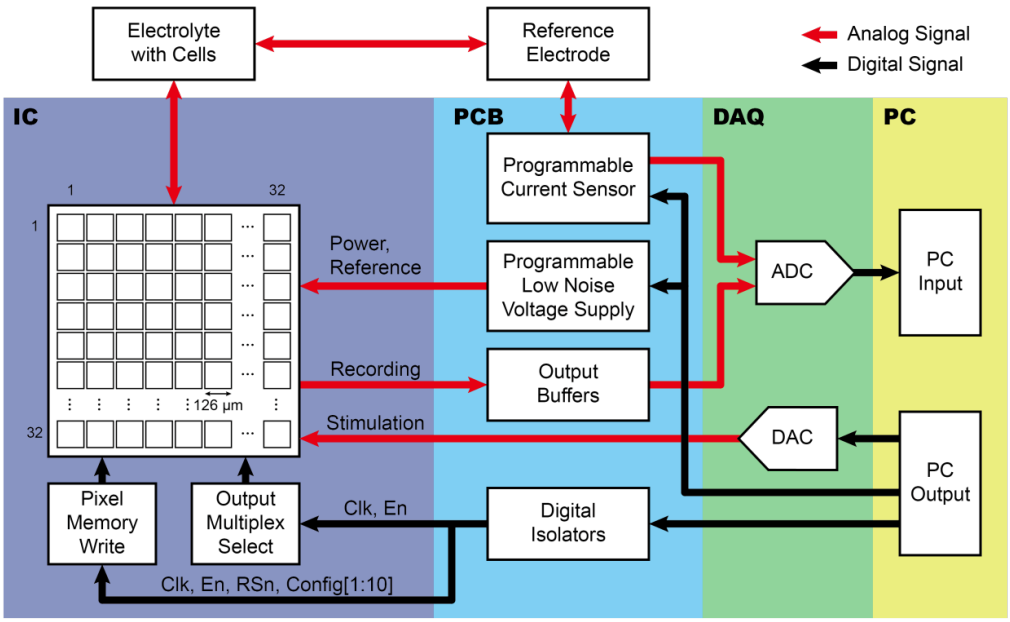

Figure 4.7 | Block diagram of the overall system depicting the operation of the CNEA using the printed circuit board (PCB), data acquisition (DAQ) card, and personal computer (PC).

Device characterization

Standard electrical measurements on chips that did not undergo post-processing facilitated the characterization of the pixel circuitry electrical performance. Initially, characterization of the amplifier for recording electrophysiological signals allowed the evaluation of the two distinct designs of the first stage amplifier (LNA); the first design located on the chip's top half has a measured passband voltage gain of ~20 V/V by design while the bottom half design ~8 V/V. Changing the parasitic junction capacitance of the diode pairs used as pseudo-resistors attains the passband gain difference between the two amplifier designs. The higher gain of the amplifiers in the top half pixels is attained via the lower parasitic capacitance associated with the larger number but smaller diodes in series, in comparison to the design of the bottom pixels. The measured transfer functions of the top (red) and bottom (blue) pixel overall amplifiers from V_{in} to V_{out}, shown in Figure 4.8a, convey the overall passband gain of ~400 V/V for the top pixel and ~180 V/V for the bottom pixel. Moreover, the measured transfer functions show the bandwidth of the bandpass configurations that filter out the low-frequency $1/f$ noise and high-frequency

noise above 5 kHz; the top passband gain of ~400 V/V is accompanied by a bandwidth of 0.05 Hz to 5 kHz while the bottom passband gain of ~180 V/V is accompanied by a bandwidth of 0.1 Hz to 5 kHz. In addition, measurements of the amplifier gain as a function of the VGA setting (Fig. 4.8 b), which once again shows the difference in passband gains of the two distinct designs in addition to conveying the availability of a wide range of gains that maximize output dynamic signal range. Measurements of the maximum amplifier gain across the whole array, shown in a 32x32 heat map array (Fig. 4.8 d), was obtained by turning on both the stimulators and amplifiers of the entire array and applying a sine wave (1 mV, 100 Hz) to the stimulators and recording the amplifiers' outputs.

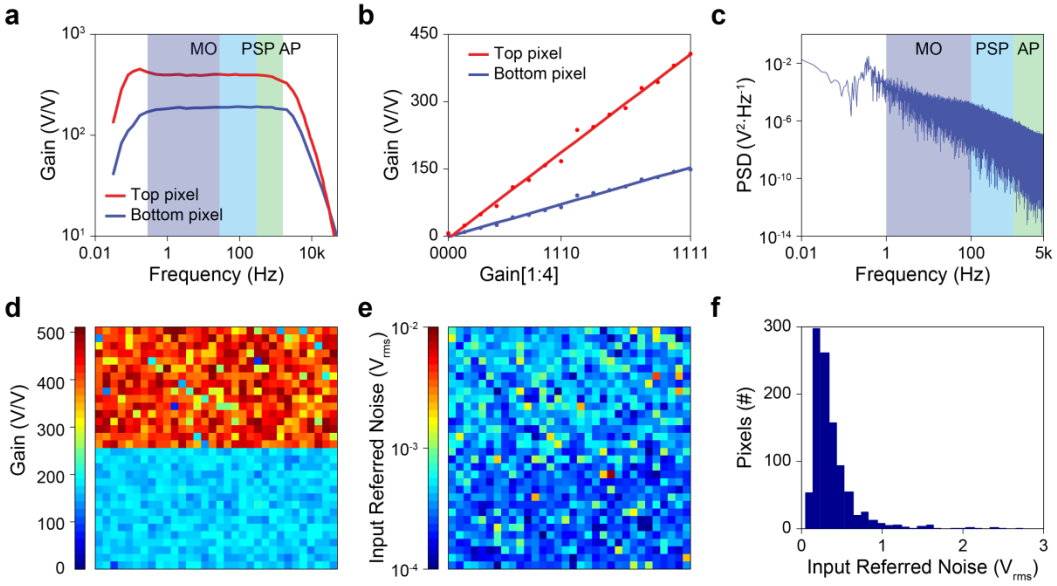

Figure 4.8 | (a) Measured transfer function of the top and bottom pixel overall amplifiers. Typical bandwidth of electrophysiological signals, in particular, membrane oscillations (MO), postsynaptic potentials (PSP), and action potentials (AP), are shown. (b) Measured amplifier gain as a function of the VGA code, Gain[1:4], for both the top and bottom pixels. (c) Output power spectral density (PSD) of a bottom pixel with typical electrophysiological bandwidths shown. (d-e) Heat map plots of all 32×32 pixels in the array of an integrated circuit showing the (d) maximum amplifier gain at 100 Hz. and (d) estimated integrated input referred noise across the electrophysiological bandwidth from 1 Hz to half the sample frequency, 4.875 kHz. (f) Linear distribution of input referred noise (e) (two outliers above 3 mV_{rms} omitted).

Afterwards, noise characterization was performed through measurements of the output power spectral density (PSD) of a bottom pixel with typical electrophysiological bandwidths (1 Hz to 5 kHz), as shown in Figure 4.8 c. At maximum gain the integrated output noise of this particular pixel resulted in

38.4 $mV_{rms.}$ The integrated input referred noise at V_{in} – referring to nanowire voltage node – is calculated by using the pixel's maximum passband gain of 152 V/V turns to be 253 μV_{rms}. Similarly, measurements of the output noise were performed across the whole array and the integrated input referred noise was calculated (integrated output noise divided by the pixel gain) across the electrophysiological bandwidth from 1 Hz to 5 kHz; it resulted in ~250 μV_{rms} as shown in the heat map in Figure 4.8 e. A difference in input referred noise is also seen between the top and bottom half pixels since more noise is filtered in by the larger bandwidth of the top design.

Characterization of the whole pixel array allowed the overall evaluation across the chip; it further portrayed the difference in gain of the top and bottom amplifier design, identified some performance variability from site to site despite their identical design, and allowed the measurement of maximum power density. The significantly larger gain associated with the top pixel design in comparison to the bottom pixel design is clearly depicted in the heat map in Figure 4.8 d. In addition, this heat map clearly portrays the gain variability from site to site, more significant in the top pixel design. This gain variability is mainly attributed to process variation of the feedback diode-pair parasitic capacitance; hence the top half with more diodes pairs has more variability. Furthermore, these large-scale measurement allowed the characterization of the maximum power density that resulted to be 61.5 mW/cm^2, measured with all amplifiers turned on and in good agreement to the designed value and fitting for substrates supporting viable cellular cultures.

Post-fabricated chips are further evaluated by characterizing the top nanowire to solution interface. The nanowire conductance was characterized through current-voltage (I-V) measurements between individual pixels and the Ag/AgCl reference electrode in extracellular solution. Figure 4.9 a shows the I-V characteristics in extracellular solution of two distinct nanowire electrodes, one consisting of an exposed gold tip and the other one platinum. The plots show linear voltage ramps at a scan speed of 50 mV/s across a range of 2.5 V centered near the $I = 0$ point (~0.3 V vs. Ag/AgCl for Pt and ~0.45 V vs. Ag/AgCl for Au). The data shows that there is a wide range of purely capacitive interaction via the double

layer capacitance, the region in which the reading amplifier operates. Beyond this region, both positive and negative faradic currents flow.

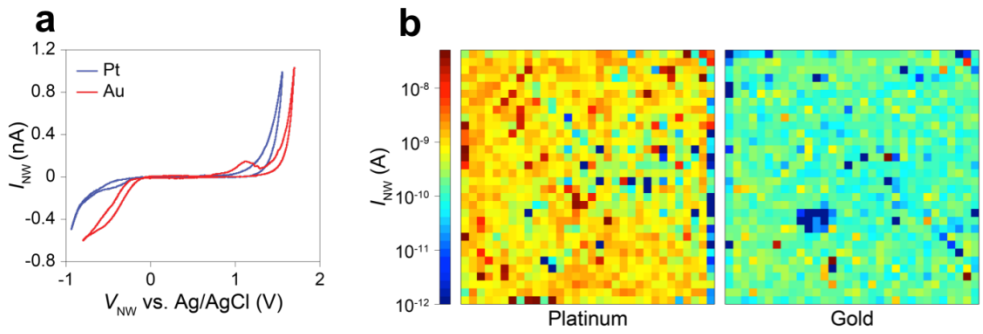

Figure 4.9 | (a) Current-voltage measurements of two pixels, Pt and Au tipped, vs. a Ag/AgCl reference electrode in extracellular solution. A linear voltage ramp is applied at a scan speed of 50 mV/s across a range of 2.5 V centered near the $I = 0$ point (~0.3 V vs. Ag/AgCl for Pt and ~0.45 V vs. Ag/AgCl for Au). (b) Measured nanowire current of each pixel across two devices, Pt and Au, with the application of a voltage step of 1.5 V vs. the Ag/AgCl reference in extracellular solution. The current is measured 100 ms after the voltage step.

Across the chip, evaluation of the nanowire conductance is obtained through the generation of conductance maps (Fig. 4.9 b), which is run before each electrophysiological test to ensure that conductive nanowires are present, and to track changes through multiple device use. This characterization is performed by measuring in a sequential order (one pixel at a time) the current through the reference electrode after 100 ms of applying a 1.5 V signal through the pixel's stimulation buffer. The 100 ms pause is helpful to ensure faradic current, and therefore exposed metal tips, as opposed to purely capacitive current through the insulating silicon dioxide on the nanowire sidewalls and pad. Pixels with currents measuring less than ~30 pA (dark blue in plots of Fig. 4.9 and 10), an empirically determined value, are considered to be non-conductive to perform experiments. Overall analyzes of the measured conductance show more than ~90% of the sites to be functional in stimulation and recording experiments.

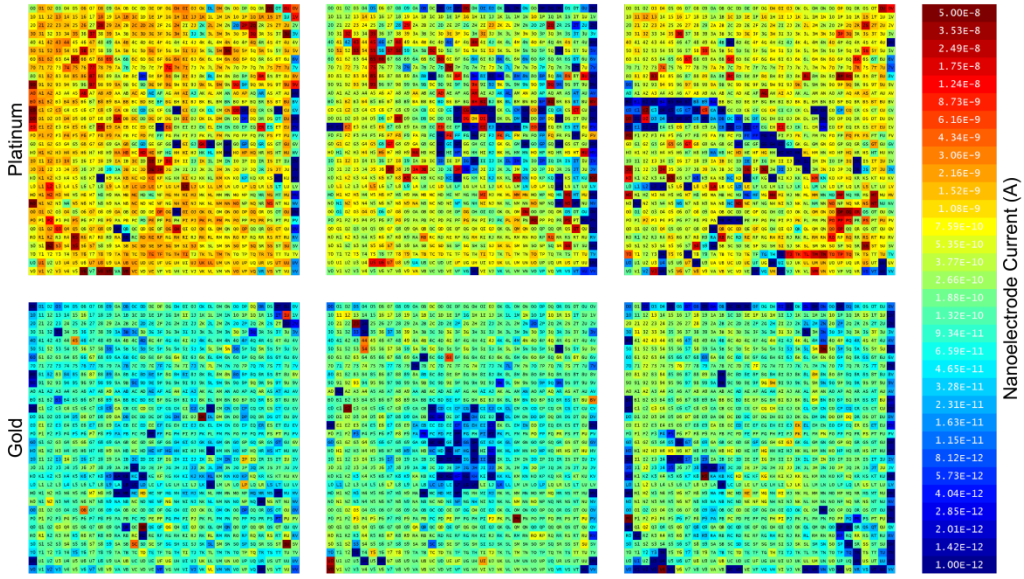

Figure 4.10 | Nanowire conductance across 6 different chips while in extracellular solution. A 1.5 V voltage step is applied to each pad with respect to the Ag/AgCl reference electrode and the current is measured after 100 ms. The three on top are Platinum tipped nanowires and the three on the bottom are Gold tipped nanowires.

4.5 Interfacing Biological Systems

We characterized the CNEA interface with cellular cultures and optimized its operation protocols using HEK293 cells as a model system. HEK293 cells offer an ideal platform since they have a short culture time (only a few hours) before electrical interrogation, and their membrane resistance has a robust passive electrical response remaining constant within 15mV of the resting membrane potential[116]. We performed simultaneous interrogation of HEK293 cells residing directly on top of the nanowires via (1) whole-cell patch-clamp stimulation/recordings and (2) voltage readings through the nanowires and their local amplifier to evaluate the overall functionality of the nanowire electrode pixels. Patch clamp is used in these experiments for verification and characterization of the nanowire performance.

We begin standard experiments by evaluating and characterizing the complete 32x32 array by measuring the gain and deriving the input referred noise. Figure 4.11 a,b show the heat maps of these two parameters, correspondingly. Subsequently, we proceed with the identification of centrally localized cells

on top of pixels with suitable characteristics and start the biological experiments. Typically, we use a short voltage pulse to permeabilize the cell membrane and promote nanowire penetration, thus resulting in intracellular electrical coupling[26,127,140]. Operating the patch clamp in voltage clamp mode allowed monitoring of the cellular current response simultaneously with voltage pulse stimulations (Fig. 4.11d, bottom row). Without spontaneous membrane permeabilization, nanowire electrodes cannot detect changes of the membrane potential resulting from applied patch pipette voltage pulses (Fig. 4.11b, first column, NW – top, patch clamp – bottom). However, application of a voltage pulse through the nanowires (Fig. 4.11d, middle column) induces intracellular electrical coupling, thus allowing high-fidelity nanowire measurements of the stimulated membrane potential changes (Fig 11d, third column, top row).

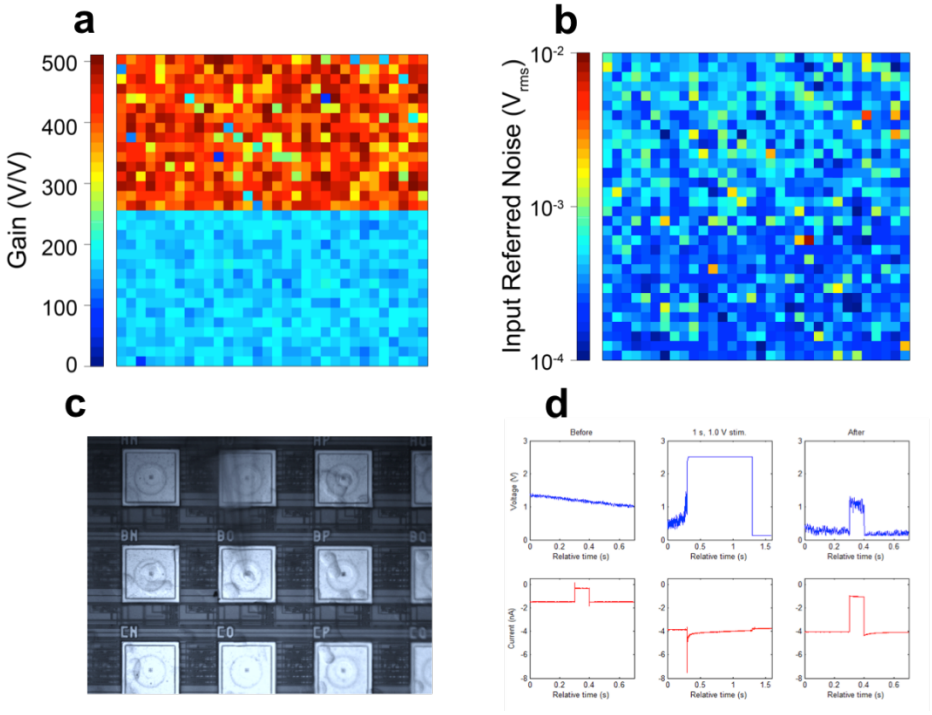

Figure 4.11 | (a) Heat map of pixel gain across the 32x32 array; clearly depicting the difference between the top and the bottom pixel designs. In addition, the pixel gain value determines the bias voltage to be applied to the pixel enabling the operation of the amplifier in its optimal range. (b) Input referred noise estimated by integrating the output power spectral density over the signal frequency range and dividing the measured gain generated through automatic current mapping to determine pads with good NWs. Apply 0.5V for 200ms on each pad, read corresponding current. (c) Representative DIC micrograph of HEK293 cells cultured on a CNEA device; patched cell centrally located on pad BO. (d) Simultaneous

Figure 4.11 (Continued). recording on HEK cell from nanoelectrode (top raw) and patch clamp (bottom raw) in response to patch voltage pulses.

Once intracellular access is achieved, we use the nanowire electrodes to monitor the membrane potential with high fidelity and resolution. To characterize the recording capabilities of CNEA pads, we used the patch pipette to change the membrane potential by applying voltage signals to the cell (in voltage clamp mode) and measure them simultaneously with the nanoelectrodes. Specifically, the change in V_m induced by the patch pipette led to a change in the nanowire voltage due to the charging/discharging of the electrical double layer at the metal-coated nanowire tips. Figure 4.12a below shows the nanowire voltage measurements in response to patch pipette pulses, 20 mV and 50 mV, across several pads/cells. These particular measurements were performed with the top design pads, which are characterized by higher gain compared to the bottom design pads (Fig. 4.11a). In addition, we conducted long duration recordings through the nanowires on HEK293 cells of sequential voltage pulses with increasing magnitude applied via the pipette, (Fig. 4.12b). As depicted in the heat map across the array of the amplifiers' gain and observed in these recordings, there is a significant variability in the measured magnitude of the output signal resulting from the range of gains from ~13 V/V to ~ 26 V/V. Furthermore, the long-term measurements of the membrane potential through the high-gain, top amplifiers show saturation at the baseline (~ 0.2 V) due to the reference voltage not centering the amplifier's DC output in the middle of its dynamic range, (0.2 V to 2.6 V) in combination with a large gain of the amplifier, Fig. 4.12b. These variation studies allowed further evaluation of pixel performance.

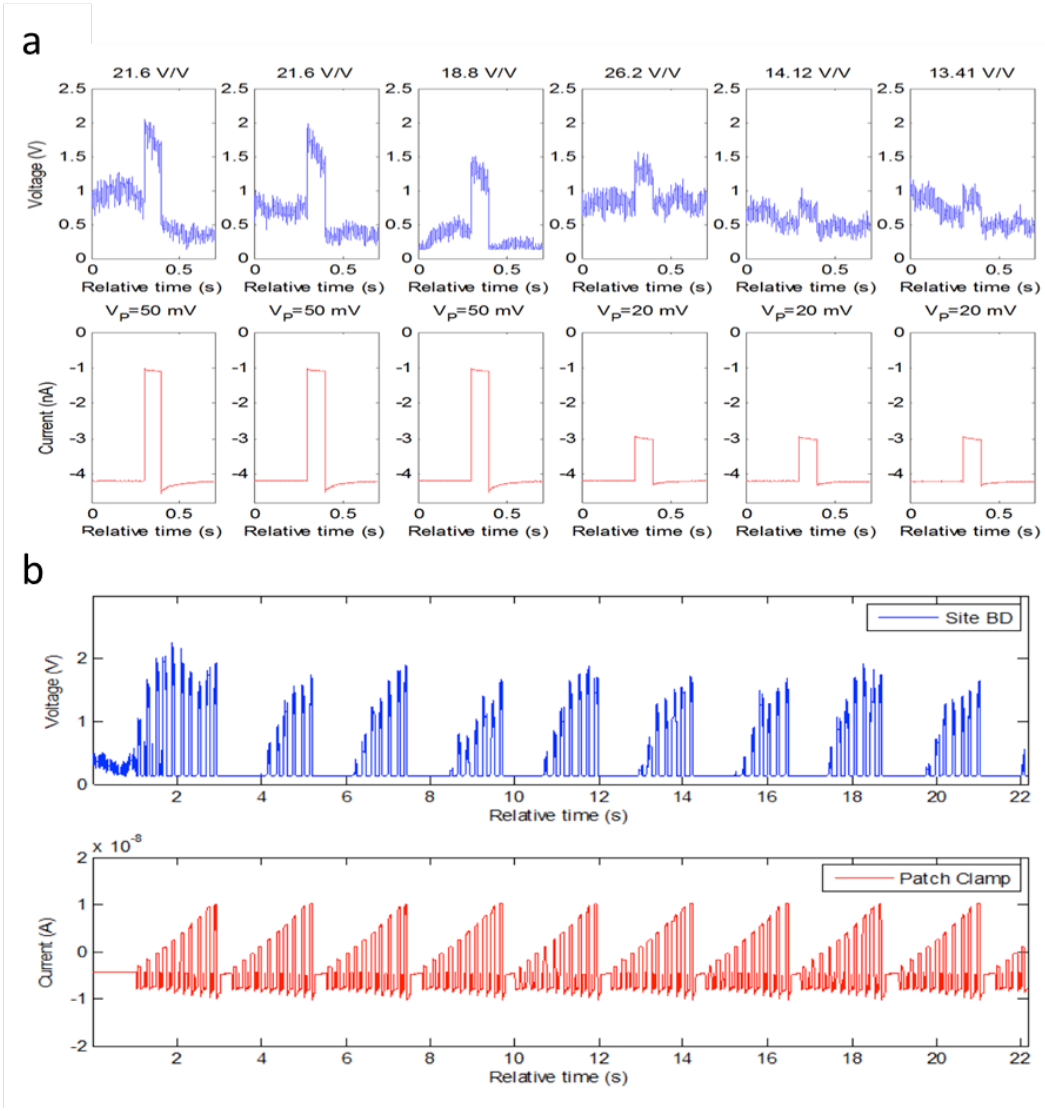

Figure 4.12 | Recording of voltage pulses with different magnitude and on different cell. (a) Nanowire measurements of changes in membrane potential of HEK293T cells in response to applied patch pipette voltage pulses of 50 mV (left) and 20 mV (right). (b) Current response of the cell measured simultaneously via a patch pipette.

In addition, we utilized similar HEK293 experiments to characterize the stimulation/recording performance of the bottom pads and evaluate the differences between the top and bottom amplifier designs. Similar to the top pads, once the nanowire-cell interface is intracellular, the changes in the membrane potential with increasing amplitude (induced via the patch clamp in voltage clamp mode) are recorded reliably through the nanowires and pixel amplifier. As expected from the amplifier design, these measurements are characterized by significantly lower intergraded gain of ~5 V/V. This reduced gain is

as expected based on the circuitry design that defined the maximum passband gain of the amplifier to be 400 V/V for the top circuitry while 150 V/V for the bottom circuitry. On the positive side, the lower high-f and low-f noises associated with the bottom circuitry facilitates measurements of the membrane potential without saturation and better SNR. Analysis of the recordings of Fig. 4.13c showed that voltage changes measured at the nanowires were ~ 50 times smaller than the voltage changes controlled by the patch clamp. These capacitively coupled measurements through the on-pixel amplifier demonstrate a 6x improvement in comparison to our VNEA measurements performed via off-chip amplifiers. Furthermore, we evaluated the recordings of typical neuronal signals (using actual action potentials measured through patch clamp from *in vitro* cortical neurons) applied to HEK293 cell. AP-like signals are clearly distinguishable from the noise in single measurements (measured input referred noise, 230 μV_{rms}). Besides verifying the capability to measure neuronal signals, these measurements show that the nanowires are measuring intracellular signals with minimal signal distortion. This is observed in the averaged output data that fully preserve the original waveform (Fig. 4.13c).

Once the nanowires had access to the interior of the cell, the pixel was also used to control/stimulate the cell's membrane potential. As an example, Fig. 4.13 d shows the changes in membrane potential measured at the patch pipette resulting from the applied biphasic voltage pulses through the nanowires. The changes in the membrane potential are tracked through the patch pipette in current-clamp mode by monitoring the potential value required to maintain the fixed current. Since the biphasic voltage pulses are centered near $I = 0$ A (the plateau region of the current-voltage curve of the nanowires) the stimulating pulse is transmitted primarily through the double layer capacitance of the nanowire interface, thus resulting in the RC response of the changes in membrane potential. Nevertheless, we show that biphasic pulses (~ 1 V) can manipulate the membrane potential by more than ±50 mV, corresponding to a large enough amplitude to stimulate and/or inhibit action potentials. These characterizing and evaluative experiments on HEK293 cells demonstrate the two-way and intracellular interface with the capability of stimulation and recordings of real-time neuronal activity.

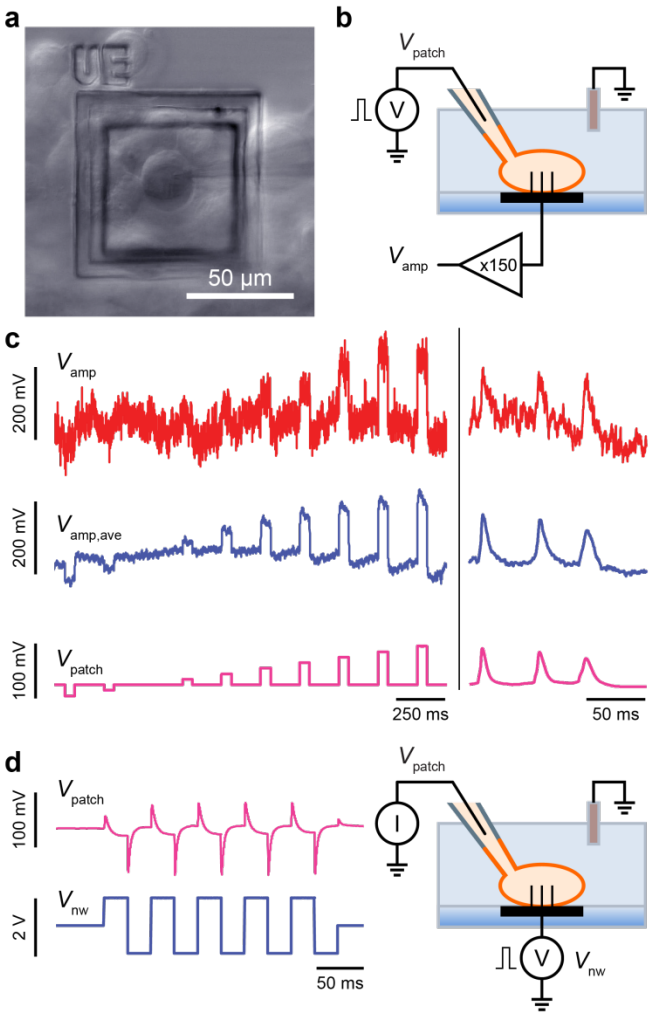

Figure 4.13 | (a) Microscope image of HEK293 cells sitting on top of a pixel pad with nanowires simultaneously interfaced via a patch pipette. (b) Voltage signals are applied to the patch in voltage clamp mode and measured through the nanowires and pixel amplifier to characterize the ability of the CMOS-nanowire array chip in measuring cellular signals. (c) Measured input, V_{patch}, and output, V_{amp}, signals from the HEK293. Increasing voltage pulse amplitudes (left) and recorded action potential shaped signals from *in vitro* rat cortical neurons (right) are measured through the nanowires; 50 pulse sequences and 100 action potential sequences are averaged for $V_{amp,avg}$ to reduce the noise. (d) Applied biphasic voltage pulses to the nanowire, V_{nw}, and measured responses of the HEK293 cell's membrane voltage, V_{patch}, (left) using the patch pipette in current clamp mode (right). The applied signal to the nanowire is approximately centered at the $I = 0$ point.

Cardiomyocytes – long term and stable recordings/ interface

Next, we made use of cardiomyocytes to further investigate and evaluate the capability of CNEA devices in recording intracellular signals. We cultured neonatal rat ventricular cardiomyocytes that typically fire action potentials spontaneously, resulting in beatings that are simultaneously observed with

our optical microscope, thus eliminating the necessity of patch clamping as a second independent probe. To use the CNEA with cardiomyocyte cultures, we coated them with nitrocellulose and allowed the cultures to grow and develop for between five and seven days. Right before experiments, we evaluate the culture's viability and perfuse it with Tyrode solution (extracellular solution mimicking biological conditions) to facilitate the electrophysiological study of cardiomyocytes.

In addition, before starting biological measurements we assess and adjust several controllable parameters of CNEAs to optimize their performance. Based on previous studies, we determined that biasing the V_{ss} to -2.7 V minimizes the leakage currents resulting from the amplifier diodes. Also, we set the bias voltage (V_{bias}) of individual pads based on their specific characteritics, which is determined through automatic generation of a bias voltage-gain sweep map. The bias voltage is swept from high to low with the gain and output voltages measured at each $V_{\text{bias,}}$. The bias voltage which places the amplifier's output in the center of its dynamic range is then chosen, thus resolving the variation of optimal performance across the array. Subsequently, we perform automatic current mapping (by applying 0.5V for 200ms on each pad and reading the corresponding current) to determine pads with good nanoelectrodes and eliminate the usage of non-conductive nanoelectrodes, which is typically only 10%.

Once the CNEA functional settings are optimized, we identify the pads that are directly interfacing actively beating cardiomyocytes via the central nanoelectrodes. First, we monitor the amplifier recordings to determine whether electrical coupling is achieved naturally. To determine the coupling status, we utilize cells beating spontaneously, monitored via microscope, which coincide with their membrane potential changes (APs). If we can't detect their electrical activity via the nanowire recordings, the pad is switched to stimulation mode to facilitate membrane permeabilization leading to intracellular access. In stimulation mode, we set V_{bias} at 2 V in the middle of the stimulation range (0 – 4 V) while V_{ss} is set at -2.7 V, which corresponds to setting the NW in the center of its capacitive range, thus eliminating any current passage. A typical membrane permeabilization protocol consists of three trains of pulses 0.5 s spaced apart with each train consisting of five 50 Hz biphasic pulses. The peak-to-peak magnitude of the stimulation pulses start at 1 V and gradually increase with 0.1 V increments until we can record the

beating. Concurrent mechanical beating of the cell can often be observed with stimulation pulses, and can be used as a sign to confirm that we have electrical coupling. Having achieved intracellular access, we switch to recording mode and monitor the continuous cardiomyocyte AP trace.

Results of a typical experiment are summarized in Fig. 4.14. Initially, it shows a trace depicting the continuous movement of an electrically active cardiomyocyte cell (top), calculated through taking derivative of image acquisition. The trace peaks are directly correlated to the beat of the cell as indicated by the aligned action potential spikes (shown in the middle row) recorded through the underlying nanowire by the amplifier. Some of the spikes recorded by the amplifier were not observed in the cell movement, which is due to the low frame rate of image acquisition. The bottom row of Fig. 4.14 shows detail of recorded action potentials with good signal-to-noise ratio (left) and a recorded action potential that shows sub-threshold behavior, with the membrane rising before it fired an action potential (right). These recordings clearly demonstrated the ability of our nanoelectrodes and the underlying integrated circuitry to record electrical signals from cardiomyocytes with high fidelity and resolution.

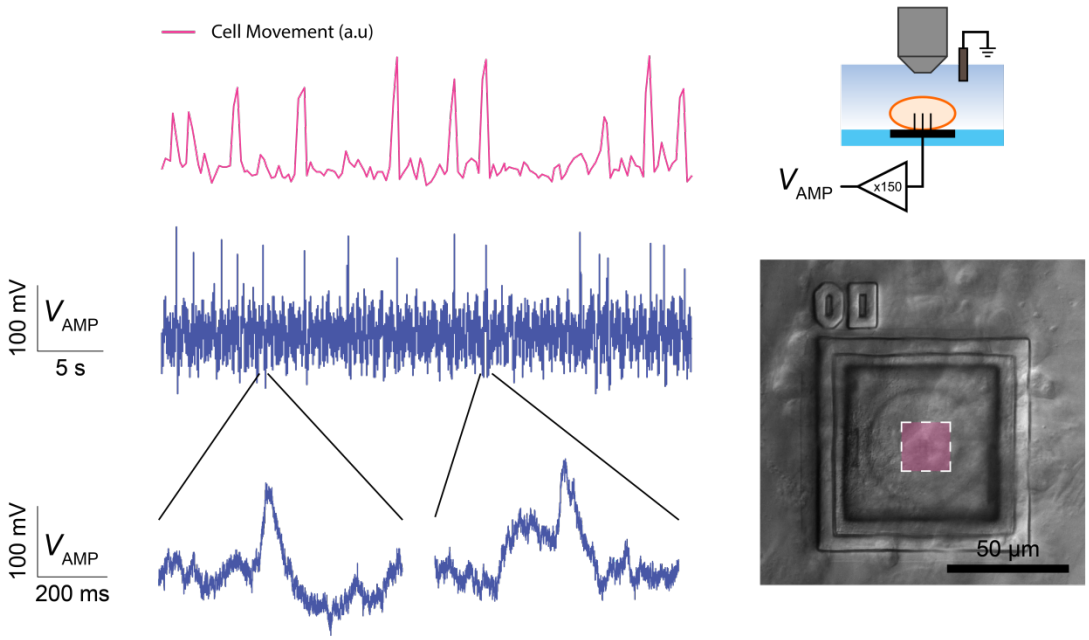

Figure 4.14 | Recordings of cardiomyocyte electrical activity.

We also utilized our nanoelectrodes to stimulate cellular action potentials by applying voltage pulses V_{NW} while operating the underlying circuitry in stimulation mode. Fig. 4.15 shows cell movement (top), with peaks correlated to the beat of the cell. Initially, the cardiomyocyte was beating at a relatively low frequency, about once every 30 seconds. To achieve a higher frequency activity (a proper beating activity of around 1 beat/sec corresponding to a normal heart rate), 10 trains of pulses were then applied at a frequency of about one pulse per second (bottom) to the nanowires interfacing the cardiomyocyte. We used pulse-trains consisting of five 50Hz biphasic pulses with peak-to-peak voltage 2 V, with the spacing between them set to 1 sec. Upon application of the pulses, the cardiomyocyte fired action potentials at a frequency corresponding to the applied pulses, thus demonstrating the ability of the nanowire to intracellularly stimulate a cardiomyocyte.

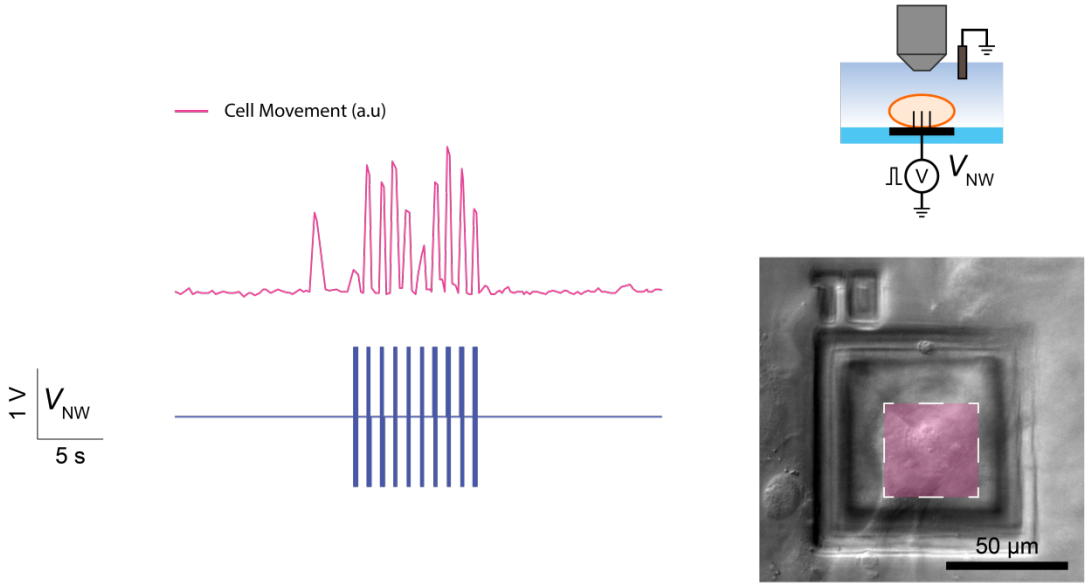

Figure 4.15 | Stimulation of cardiomyocyte electrical activity.

Monitoring neuronal activity of* in vitro *hippocampal and cortical neuron culture

Having completed the device characterization and protocol optimization, we used the CNEA to interrogate rat cortical neurons through high-fidelity intracellular recording and stimulation of their electrical activity. Optimal conditions for neuronal cultures were achieved by optimizing the surface treatment of CNEA devices through a two-day process that generated the poly-d-lysine culture support

coating. To allow electrophysiological development and the formation of synaptic connections, we cultured the cortical neurons for a minimum of 6 days *in vitro* before interrogation. Initially, we used nanoelectrodes to monitor changes in the membrane potential in response to sequential pulses of increasing amplitude applied via a patch pipette in the voltage clamp mode (1. 7b). Single-shot data, shown on the top in Fig. 4.16b, are typically characterized by 2~3 signal-to-noise ratio, while the average of 50 sequences obtained under identical experimental conditions could improve the signal-to-noise ratio by an ideal factor of sqrt(# of averaged samples) or ~7× improvement to 14~21. Furthermore, we utilized the nanoelectrodes to monitor individual action potentials (APs) evoked by a patch pipette. In this experiment, we ran the patch clamp in current clamp mode to inject current pulses that induced the neuron to fire APs. This particular dataset is associated with a lower SNR ratio due to the higher attenuation at the nanowire-cell interface (100x compared to the ~ 25x of the previous dataset). As before, averaging (100) sequential pulses obtained under identical experimental conditions, we could recover the AP waveform pattern in close correlation with the patch clamp measured potential. As demonstrated in Fig. 4.16e, we achieved stimulation of neuronal activity by applying biphasic voltage pulses to the nanoelectrodes. The active response to the third pulse (shown in Fig. 4.16f zoomed in view, bottom left) is distinguished by larger amplitude and specific shape that characterize typical APs. Aiming to minimize the number of pulses necessary to evoke individual APs, we established that by applying two biphasic pulses the neuron fired on the second pulse.

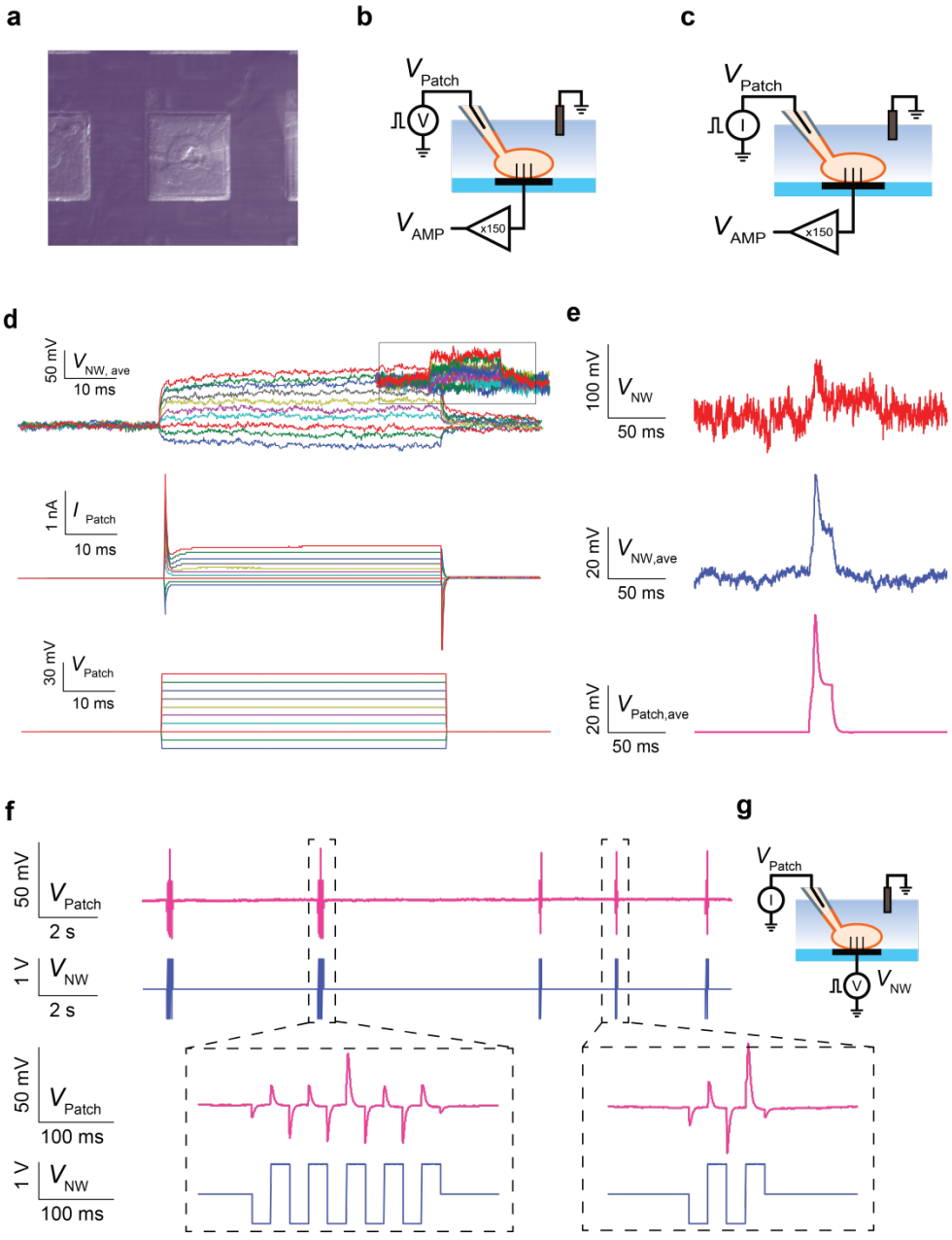

Figure 4.16 | Recordings and stimulations of neuronal activity. (a) Micrograph of a centrally located cortical rat neuron, interfacing the nanoelectrodes through cell body. (b) Schematic of the dual cell interface during NW recordings: Voltage signals are applied to the patch in current clamp mode and measured through the nanowires and pixel amplifier to characterize the ability of the CMOS-nanowire array chip in measuring cellular signals. (c) Schematic of the dual cell interface during NW recordings in current clamp mode: Current pulses are injected to cause the neuron to fire an action potential which are then read through the nanowires. (d) Membrane potential changes measured via the NWs, V_{amp}, in response to a patch pipette pulse sequence of increasing amplitude, V_{patch}. The average of 50 sequences shown to reduce the noise, with one-shot data shown in the inset. Current response measured through the

Figure 4.16 (Continued). patch pipette, shown in the middle, shows the cell viability even after penetration for intracellular recordings. (e) NW recording of neuron action potential fired in response to current pulses injected through the patch pipette; single shot NW data (top, red), averaged NW (middle, blue), and patch pipette simultaneous recordings (bottom, magenta). (f) Neuron fires action potentials stimulated via biphasic voltage pulses applied to the nanowires. (g) Schematic of the dual cell interface during NW stimulations: using the patch pipette in current clamp mode while applying voltage pulses through the NWs.

4.6 Prospects

Generation of tissue interfaces

The results presented here establish the CNEA platform to be capable of intracellular and parallel recording/stimulation of *in vitro* neuronal ensembles. For *ex vivo* applications of the AP chip for slice recording, we will fabricate long electrodes with sharp tips (>25 μm in length, 150-nm diameter at the tip, and 1.5-μm diameter at the base) so that we can penetrate through a layer of dead cells and access live neurons deep within the tissue (Fig. 4.17). We have developed the process flow for the fabrication for *ex vivo* devices as summarized in Figure 4.17. First, we flip-chip bond a silicon-on-insulator (SOI) substrate on the CMOS chip via conductive gold bumps, and fabricate the electrodes out of the SOI substrate. To this end, we will use reactive ion etching on the handle layer to expose the buried oxide layer of the SOI substrate. We will then generate an array of 1.5-μm diameter photoresist discs (serving as etch masks at the later step) on top of the buried oxide. Two subsequent steps of reactive ion etching applied to of the buried oxide and silicon device layer will generate the long electrodes on top of the exposed CMOS metal contacts. Subsequently, we will use dilute buffered oxide etch to selectively thin the 3-μm-tall oxide tip to 150 nm while leaving rest of the silicon base (1.5 μm in diameter; 25 μm in length) intact. The thicker base provides structural rigidity required for tissue penetration. Last, we will perform metallization and passivation via similar processes developed for the *in vivo* platform generation. This advanced geometry of the front side of the array will enable interfacing and studying intact slices of brain tissue.

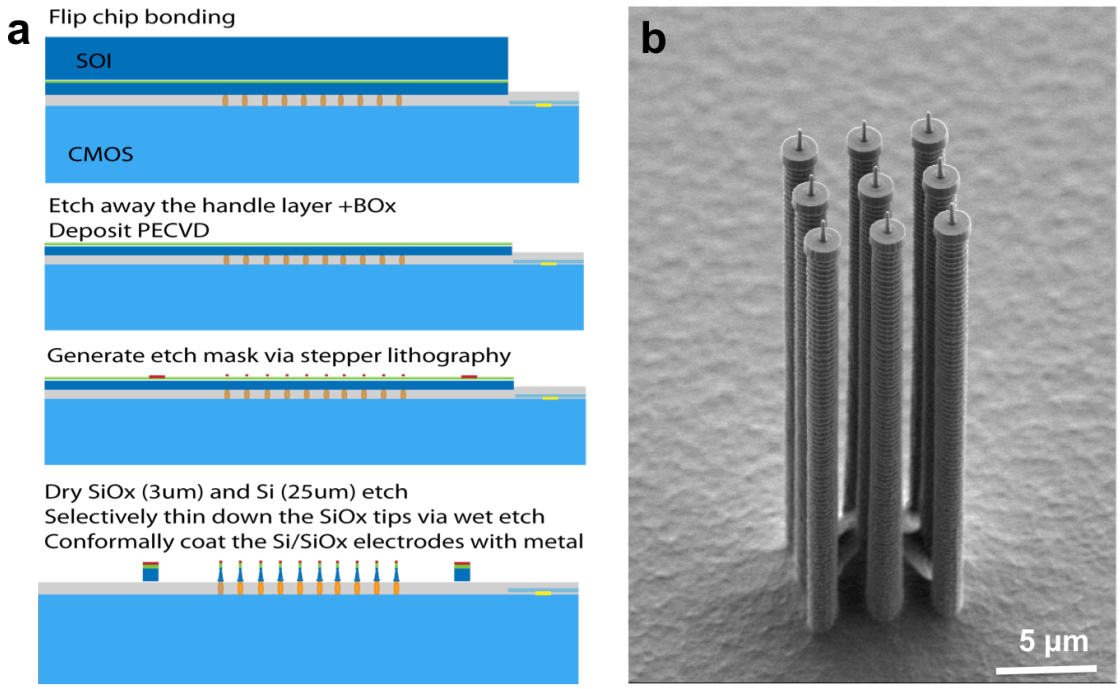

Figure 4.17 | (a) Summarized process-flow for generating tissue-interfacing nanoelectrodes. (b) SEM images of the two level nanoelectrodes fabricated through our optimized processes.

Network level studies – Functional map generation

The unique combination of intracellular and parallel features characterizing our nano-neuro interface, pave the way for higher-level experiments to map the functional connectivity of neuronal networks both *in vitro* and *ex vivo*. We are particularly interested in addressing the question of how changes to the input-output relationships of neuronal networks form the foundation of learning and memory[141]. The mechanisms and dynamics of this process remain poorly understood due to a lack of tools that are capable of simultaneously recording and stimulating the electrical activity of many individual cells[142].

The CNEA can overcome these limitations because it enables simultaneous intracellular measurements from many cells within a single circuit. Using this approach, we will search for trends in the spatiotemporal dynamics of neuronal networks as they are trained to perform specific computations. By identifying characteristic network dynamics that frequently occur during the training process, we will develop functional network motifs that will guide future studies of network dynamics *ex vivo* and *in vivo*,

and help in developing theories for learning and memory behavior. The concept of structural network motifs – frequently repeated connectivity sub-graphs that appear within a larger network – has proven to provide a powerful technique for analyzing networks and decomposing them into functional building blocks[143]. Using our CNEA we will search for functional equivalents of these structural motifs, referred to as functional motifs, and use them as building blocks for analyzing complex network dynamics (Fig. 4.18). The identification of these functional motifs will start by training many *in vitro* networks to perform simple computations[144,145]. Using our CNEAs combined with long-term fluorescence microscopy, we will then monitor the functional and structural connectivity of the network as it responds to controlled electrical and chemical inputs. To efficiently train the network and achieve a desired input-output relationship, we will compare a variety of input protocols including tetanic stimulation[146], paired stimulation protocols[147], and chemical reward[148]. Stimuli will be delivered to the network either electrically (using the CNEA) or optically (by transfecting a subset of the cells with light gated ion channels[50] and illuminating the network with specific spatial excitation patterns). The functional connectivity of a network will be represented as a point in multi-dimensional space where each coordinate stands for the strength of a possible synaptic connection. Changes to the synaptic strengths will move this point through the multi-dimensional connectivity space creating a trajectory. By repeating the stimulation protocols on many different neuronal preparations, we should be able to identify frequently occurring trajectories, or functional network motifs, that can serve as templates for investigation of *in vivo* neuronal dynamics and be used to develop learning rules that recapitulate the observed motifs. These investigations will guide future studies of network dynamics ex vivo and in vivo, and test theories of learning and memory behavior.

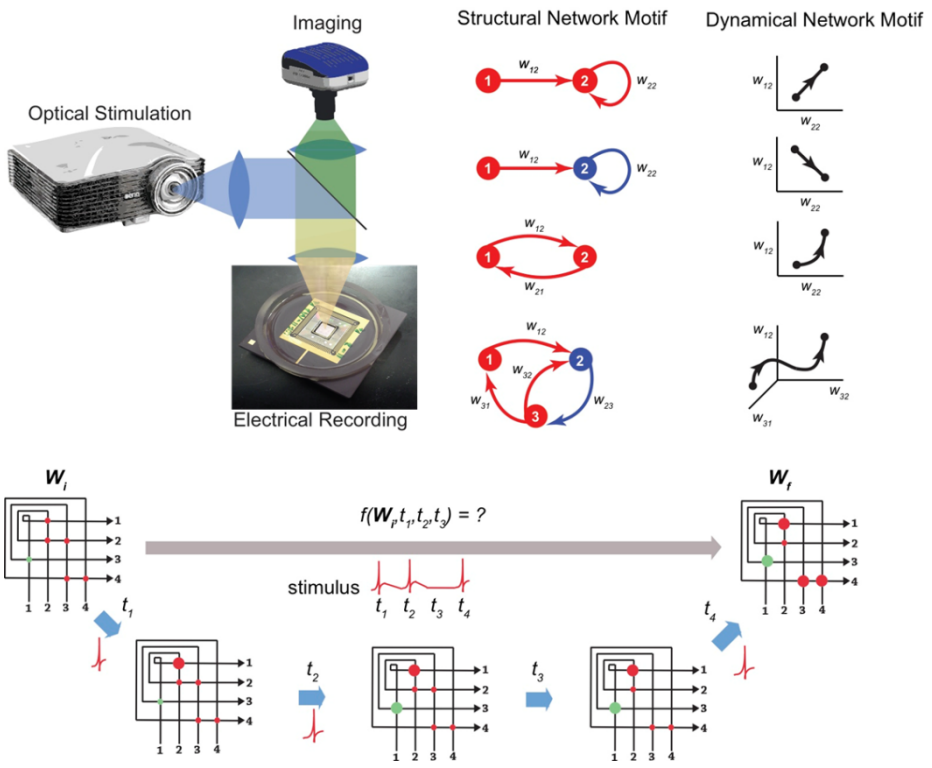

Figure 4.18 | Optical/electrical stimulation and recording of neuronal network activity *in vitro* will be combined with optical imaging to identify repeated patters of structural connectivity and functional activity. Lower panel: the synaptic strength of each connected pair monitored as a function of time (represented as a matrix of synaptic weights W). Upper right: example network (structural and functional/dynamical) motifs.

High-Throughput Discovery and Pharmaceutical Screening

To date, many neurological disorders remain poorly understood and lack therapeutic treatments; despite greater than ever research programs focusing on elucidating the cellular basis and screening for potential new drugs. In part, this has been attributed to a shortage of drug screening assays that facilitate large-scale experiments with primary mammalian neurons[149]. Our CNEA platform, with its capability for (1) intracellular recording/stimulation of neuronal activity with the fidelity that matches patch clamp pipettes and (2) high-throughput, massively parallel measurements of the responses of connected neuronal pairs and networks upon well-defined electrical and chemical stimulations (a task that would be prohibitively laborious using the currently available methods), is well suited for this task. Coupling the

CNEA to microfluidics – to enable rapid perfusion of pharmacological compounds in conjunction with electrophysiological testing – would facilitate the characterization and categorization of the behaviors of diseased mammalian neurons under the influence of small molecule pharmaceutical candidates. These capabilities make the CNEA platform an optimal assay for screening novel ion channel drug candidates in addition to helping elucidate the electrophysiological characteristics cellular mechanism of the corresponding neurological disorders, overall experimental schematic shown in Fig 20.

Genome-wide association studies continue to identify ion channel mutations that result in their irregulated activity leading to many debilitating diseases, including Parkinson's, Alzheimer's, hyperactivity disorders, epilepsy, and autism[149-151]. Neuronal nicotinic acetylcholine receptors (nAchRs) are one such example. nAchRs are cholinergic receptors that represent a superfamily of ligand-gated ion channel, and are pentameric complexes comprising different combinations of alpha (α2 – α10) and beta (β3, β4, β5) subunits. These receptors are emerging as potential drug targets for a variety of neurological diseases including Parkinson's disease (PD), Morbus Alzheimer, and hyperactivity disorders[149]. Some of nAchR subtypes (e.g. α4β2*, α6β2*, α4β2β3, and α4α6β2β3) are involved in the signaling pathways that are affected in Parkinson's disease[152], and thus can serve as particularly relevant therapeutic targets for the disease. Despite the increased interest in their potential as druggable targets they remain underutilized, and their physiology as well as involvement in neuronal pathologies remains poorly understood[153]. It remains unclear whether nAchR ligands exert their beneficial effects via receptor activation or blockage, leaving unresolved the question whether agonist or antagonist ligands would prove most beneficial for the treatment of PD symptoms[152,153].

Previous studies have identified some signature electrophysiological characteristics associated with the different nAchR subtypes. Utilizing the CNEA capabilities, we will first expand upon these findings towards a comprehensive identification and classification of the nAchR subtypes affected in PD and their corresponding phenotype. Several mouse models that recapitulate the symptoms and pathological features of Parkinson's disease have been validated. The initial experiments will therefore be conducted using neurons extracted from these Parkinsonian mouse models. We will focus our initial

efforts towards the discovery of therapeutic compounds targeted at α4β2* and α6β2*, previously identified as potential sites of drug action. Afterward, we will extend our drug discovery efforts to other subtypes. The efficacy of therapeutic compounds will be screened by profiling the compounds' effects on nAchR-mediated currents, in particular, on the modulation of the peak and steady-state currents as a function of drug concentration and treatment protocol. This electrophysiological measurement will be combined with dopamine concentration assays as well since dopamine is an essential component of the circuit involved in PD. A better understanding of the different nAchR subtypes and their mechanism of action will enable the design of more specific and efficient therapeutics for Parkinson's disease.

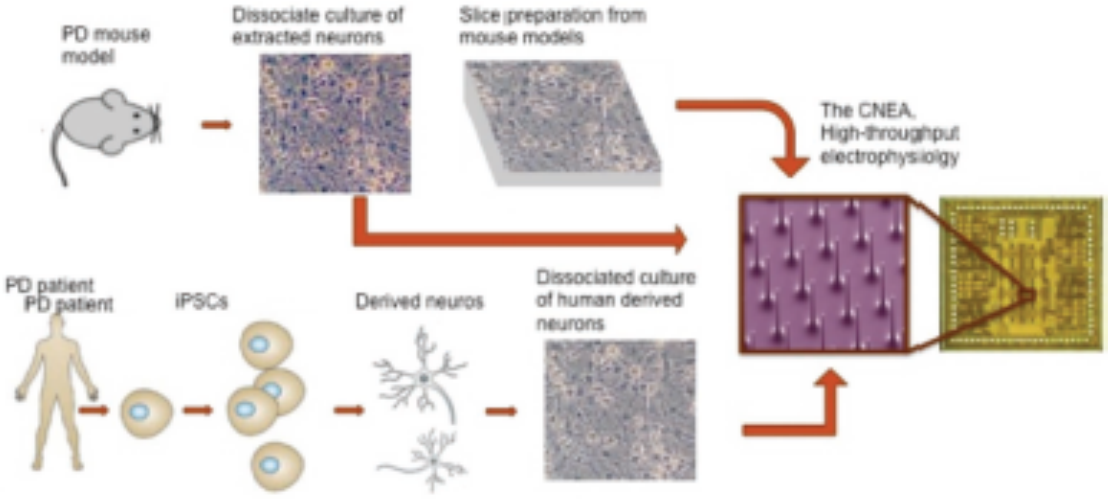

Figure 4.19 | Leveraging the high-throughput, high fidelity electrophysiology capability of our CNEA to perform screening of novel therapeutic compounds for neurological diseases; focusing on neuronal cultures and slice preparations extracted from the mouse models of Parkinson's disease. The same strategy should be applicable to neurons induced from human patients as well.

Another major line of research in drug discovery efforts for PD is focused on targeting pre- and postsynaptic sites in dopaminergic neurons. The impairments in synaptic plasticity, such as long-term potentiation (LTP) and long-term depression (LTD), have been widely implicated for the onset and progression of PD. For instance, alterations in the subunit composition of N-methyl-Daspartate (NMDA) receptors, which impair synaptic plasticity, are known to contribute to the pathological characteristics of PD[154-156]. Consequently, significant efforts have been made to identify molecules that can rescue normal synaptic activity in Parkinsonian mouse models. However, these efforts have been hampered by the low-

throughput of whole-cell patch clamp experiments. Our CNEA device, being able to simultaneously stimulate and record the activity of multiple connected neurons in dissociated cultures, will facilitate the ability to study and characterize these synaptic pathways in a much higher throughput, thereby expediting the discovery of potential drug targets as well as novel therapeutic compounds. The change in synaptic efficacy can be characterized by studying the change in amplitude as well as in the rising slope of PSPs. We will focus our initial screening efforts on therapeutic compounds targeting NMDA receptors.

APPENDIX A

Vertical Nanowire Electrode Arrays for Stimulating and Measuring the Activities of Multiple Mammalian Neurons

A.1 Introduction

Intracellular electrodes based on patch pipettes, which control and measure the membrane potential via direct electrical coupling, remain the most accurate technique for stimulating and recording neuronal activity. Unfortunately, due to the bulkiness of micromanipulators as well as the challenge of forming and maintaining high-quality cell-pipette interfaces[60,64,112], most patch-clamp studies have been limited to the simultaneous measurements of only a few neurons.

Efforts to parallelize this technique via planar patch-clamp chips have not yet been optimized for mammalian neurons, primarily due to difficulties in forming seals to their small neuronal cell bodies[64-66,67,68]. For large-scale interrogation of neuronal networks, microelectrode arrays (MEAs) are the tool of choice because they can monitor the neuronal activity from many neurons simultaneously. However, MEA measurements are extracellular and consequently, do not provide adequate signal-to-noise ratios to resolve subthreshold events[114]. Moreover, because a single electrode can stimulate or sense the activities of several neighboring cells, MEAs lack precise cell-to-electrode registry[114].

To address some of these issues and pave the way for large-scale neuronal network studies, semiconductor nanofabrication-based approaches, have been employed to generate a new class of electrical interfaces to neurons and other electroactive cells[11,71,72,75-77,109-111,113,157,158]. These tools, reviewed in detail elsewhere[114,158,159], rely on nano- and microscale structures that provide a minimally invasive interface to the cell's interior. For example, gold mushroom-shaped microelectrodes can perform multisite 'intracellular-like' recording and stimulation of neuronal activity in *Aplysia* neurons and primary rat cardiomyocytes[75,77]. Similarly, nanoscale structures based on field-effect transistors (FET) or vertical platinum nanowires enable true intracellular recording of action potentials in cardiomyocytes[10,11,72,73]. Each of these methods utilizes nanofabrication approaches to create recording platforms that can be scaled up to interrogate many cells simultaneously without using micromanipulators. A logical next step, then, is a nanofabricated device specifically designed and optimized to stimulate and record the activities of primary mammalian neurons.

Recently, we reported vertical nanowire electrode arrays (VNEAs) as a scalable experimental platform for performing parallel intracellular stimulation and measurement of

mammalian neurons[127]. These devices are fabricated from a silicon-on-insulator (SOI) wafer using standard nanofabrication processes and consist of an array of stimulation/recording pads. The first prototype had 16 pads, each of which contained a set of 9 vertical nanowires (Fig. A.1a-e); however, the number of pads and nanowires per pad can be varied to match experimental need. The VNE prototype design (nanowire diameter: 150 nm, length: 3 µm, pitch: 2 µm) was optimized to facilitate intracellular penetration and interfacing to individual neurons. The nanowire tips are selectively metalized to form the intracellular electrical interface, while the insulating glass sidewalls serve the dual function of forming a tight seal with the cellular membrane and preventing current leakage. Each electrode pad is individually addressable via a silicon track ending at a metal contact pad connected to control electronics. A polydimethylsiloxane (PDMS) well, shown in Fig. A.1e, supports dissociated neuronal culture directly on top of the VNEA. Individual devices are reusable over an extended period of time (> 1 year), provided that care is taken to clean and store them as described in this protocol.

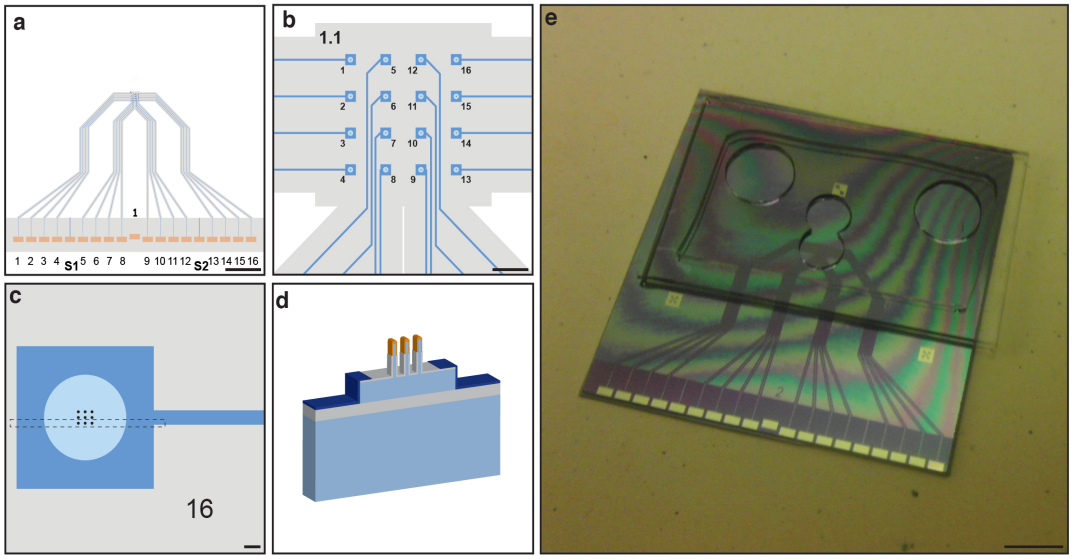

Figure A.1 | Device Layout. a, Schematic of a prototype device showing highly doped silicon electrode tracks (blue), exposed buried oxide layer (BOx) (grey), metal contact pads (orange, numbered 1-16), and substrate pads (S1, S2). Scale bar, 4 mm. **b,** Schematic of the sixteen electrode pads arranged in a 4 × 4 array with a 200-µm pitch. The central light-blue region

Figure A.1 (Continued). represents thinner (20 nm) SiO_2 insulation around the silicon nanowires. Scale bar, 200 μm. **c,** Schematic of a VNEA pad showing the 3 × 3 array of vertical nanowires. Scale bar, 5 μm. **d,** Three-dimensional rendering of the VNE cross-section (corresponding to the dashed region in **c**) showing the sputter coated metal tips (orange) and thin (20 nm) SiO_2 sidewall insulation (grey) surrounding the silicon nanowire core (blue). A thick (150 nm) Al_2O_3 insulation (dark-blue) covers the electrode tracks and regions of the exposed BOx (not drawn to scale). **e,** Image of a prototype VNEA device (25 × 25 mm) consisting of 16 stimulation/recording pads and a PDMS washer (12 × 25 mm). The PDMS washer contains a central double well (generated using two 3 mm-diameter biopsy punches) surrounding the active region of the device and two additional wells holding neurons for media conditioning (generated using a 6 mm-diameter biopsy punch). Scale bar, 5 mm.

The parallelized stimulation and recording capabilities of the VNEA can be used to map multiple individual synaptic connections in an *in vitro* neuronal network[127]. Additionally, the VNEA allows for straightforward coupling with conventional patch clamping[60,160,161], fluorescence microscopy, and optogenetic techniques[50], making possible multiplexed circuit-level studies. For example, a projector coupled to an upright microscope can be used to define a stimulation pattern for a neuronal culture expressing light-gated ion channels[162] (e.g. channelrhodopsin and halorhodopsin). The VNEA platform can then be used to record the activities of multiple neurons in the circuit and monitor how neuronal activities change both over time and in response to well-defined stimuli. The same platform can also be used to examine altered electrophysiological and synaptic activities in disease-affected neurons, as well as the responses of those cells upon the application of pharmaceutical candidates[154,163,164]. To date, most of these screening efforts have relied on patch-clamp measurements, which suffer from limited throughput[11]; the use of VNEAs for this purpose will facilitate the rapid characterization of disease-related synaptic connections and the discovery of new drug candidates for the treatment of neurological diseases.

A.2 Experimental Design - Device Layout

Figure A.1e shows a finalized prototype consisting of a VNEA chip (25 × 25 mm) and a PDMS washer (12 × 25 mm). The washer contains three cell-culture wells: a double well centered on the electrode array (formed from two 3mm-diameter biopsy punches) for neuronal measurements and two additional side wells (made with a 6 mm-diameter biopsy punch) for culturing neurons that will condition the media. All three wells share the same culture media. The double-well design allows micropipettes to approach cells from the top of the device without hitting the sidewalls of the PDMS well. The electrode tracks, also visible in the device image and schematic (Fig. A.1a-e), provide electrical connection from the stimulation/recording pads to the metal contact pads at the base of the device. Electrical isolation between individual electrode pads is achieved by etching through the device layer of a SOI wafer, thus exposing the buried oxide (BOx). We have previously described the fabrication process in detail[127]. The numbers on the electrode pads represent the location of the corresponding metal contact pads counted from left to right (Fig. A.1b). In addition to the 16 metal contact pads connected to the stimulation/recording pads, three extra contacts (two substrate pads and one floating pad, Fig.1a) are used to test the electrical contact between the device and a custom printed circuit board (PCB) (see *Mounting the Device*). An important design consideration was the minimization of the parasitic capacitance. To this end, we designed narrow electrode tracks to reduce their surface area (width: 3 μm) and insulated them with a thick aluminum oxide layer (150 nm, shown in dark blue in Fig. A.1d) using atomic layer deposition.

A.3 Modes of operation

Faradaic Recording Mode

Faradaic coupling refers to an ionic current flowing to or from the VNE as the result of electrochemical reactions at the metalized nanowire tips. This is accomplished by applying a voltage to the VNE with respect to a reference electrode (Ag/AgCl) in the bath solution. In our experimental setup (Fig. A.2 a-b), we use a custom-built current-clamp module (IC module) that can source up to ±10 nA with a compliance voltage of ±5V (Fig. A.2c). The Faradaic mode is equivalent to a patch pipette operating in current-clamp mode[160]: changes in the membrane potential are tracked by monitoring the VNE potential required to maintain a specified command current. In this mode, the VNE access resistance (the nanowire intrinsic resistance plus the electrochemical junction resistance and any residual cell membrane resistance at the nanowire-cell interface, designated as $R_{a,NW}$ in Fig. A.3c), in combination with the parasitic capacitance[118] to ground (C_p in Fig. A.3c), acts as low-pass RC filter for the recorded membrane potential. This RC filtering, combined with voltage division by the ratio of the leak resistance (R_L in Fig. A.3c) to the access resistance, results in temporally broadened and attenuated signals[127]. Typical attenuation factors and RC time constants are 3-5 fold and 5-50 ms, respectively. Nevertheless, the original waveform can be reconstructed by deconvolving the recorded signal with the VNE impulse response function (measured at the conclusion of the experiment – see *RC time constant analysis*). Recordings in the Faradaic regime are usually limited to ~10 min due to degradation of the cellular membrane by sustained electrochemical reactions at the VNE.

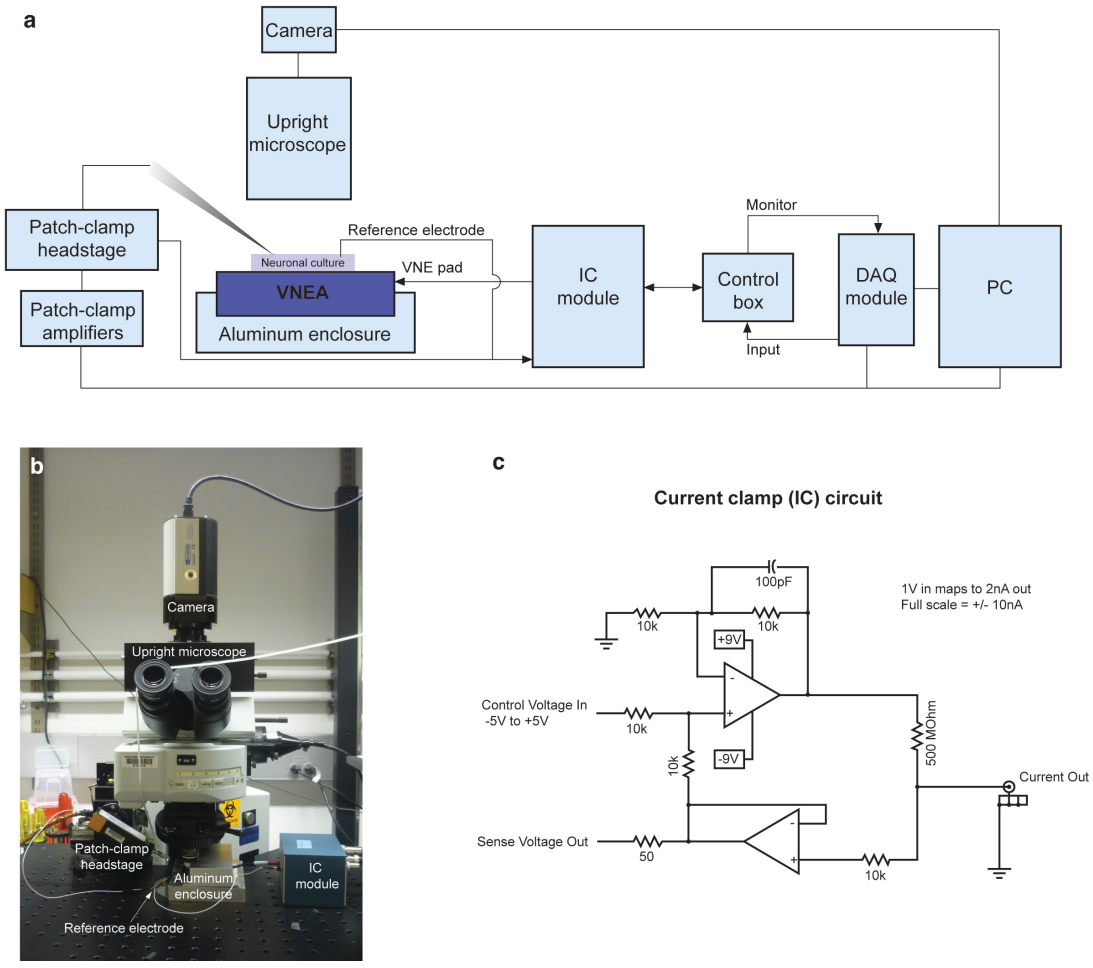

Figure A.2 | Equipment and Software Setup. a, Schematic of the hardware setup consisting of a VNEA device mounted on an aluminum enclosure and positioned under an upright microscope. The VNEA is connected to the current-clamp (IC) module, which connects to the data acquisition (DAQ) module through the control electronics. The IC module and the patch-clamp head stage share the same Ag/AgCl reference electrode submerged in the neuronal culture bath solution. Patch-clamp amplifiers connected to the head stage enable conventional whole-cell patch clamping, and a digital camera allows imaging of the neuronal culture. A desktop computer connected to the DAQ module, patch-clamp amplifiers, and camera controls the hardware and data acquisition. **b,** Image of a typical setup mounted on an air table. **c,** Circuit diagram of the IC module that can source up to ±10 nA with a compliance voltage of ±5V.

Access Resistance and Capacitance Characterization.

We have previously described in detail the equivalent circuit analysis of the VNE-cell interface (Fig. A.3 a-c)[127]. Characterization of the VNE electrical interface allows reconstruction of the original neuronal action potentials from the RC-filtered signals recorded in the Faradaic mode. Due to slight variations in the geometry of the nanowire electrodes, each VNE should be characterized individually at the conclusion of an experiment. To measure the RC time constant, the cells on top of the VNE should be removed either using a glass micropipette or by lysing the cell through the application of a large (~1nA) sustained electrochemical current from the VNE. Once the cell is removed, the bare-electrode RC time constant can be directly extracted by fitting a single exponential to the voltage response to a command current pulse (200 pA, 300 ms in duration). Typical time constants vary between 5 and 50 ms. Since the Faradaic current is a nonlinear function of voltage, the RC time constant depends on the holding current. Therefore, the current pulse used to characterize the RC time constant should be similar to the holding current used during the experiment. The approximate VNE access resistance ($R_{a,NW}$) can then be determined by applying Ohm's law to the steady state voltage response to the current pulse. Additionally, the parasitic capacitance to ground (C_p) can be calculated by dividing the measured time constant by the VNE access resistance ($R_{a,NW}$). The typical parasitic capacitance (C_p) of a VNE is ~150 pF. To recover an unfiltered waveform from the VNE measurement, one can deconvolve the measured signals with the impulse response of a low pass filter possessing the measured RC time constant.

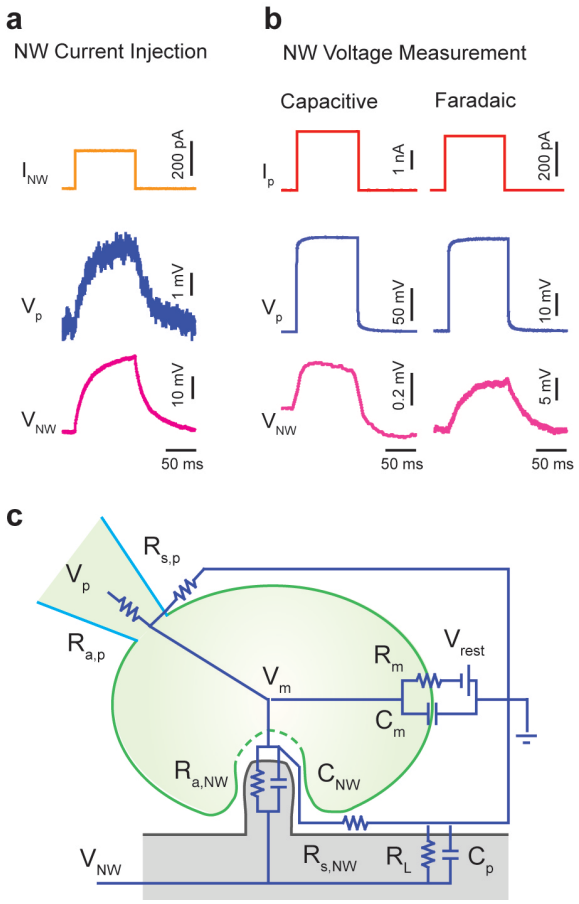

Figure A.3 | Access resistance and capacitance characterization in HEK293 cells as a model system a, Current injected through the nanowires (I_{NW}) results in a change in the membrane potential as measured at the patch pipette (V_p), confirming nanowire-based control over the membrane potential. Voltage changes measured at the pipette (V_p) were ~10 times smaller than those measured at the nanowire (V_{NW}) due to current leakage at uncoupled nanowires or defects in the electrode insulation. **b,** Current injected through the pipette (I_p) versus time in the capacitive and Faradaic modes (top row, left and right columns, respectively), and the resulting voltage response of the cell recorded with a patch pipette (V_p, middle row) and nanowires on a VNE pad (V_{NW}, bottom row). **c**, Equivalent-circuit model of the VNE/cell interface. $R_{a,NW}$, $R_{s,NW}$, $R_{a,p}$ and $R_{s,p}$ represent the access and seal resistances for the nanowires and pipettes respectively. The capacitance of the electrical double layer at the nanowire surface is represented as C_{NW}. The equivalent circuit also includes the leak resistance due to uncoupled nanowires or defects in the electrode insulation (R_L) and the parasitic capacitance to ground due to the device and associated electronics (C_p). The cell itself has a characteristic membrane resistance (R_m), capacitance (C_m) and resting potential (V_{rest}), all of which combine to determine the potential across the cell membrane (V_m). The values of these circuit elements were determined based on simultaneous patch pipette and VNEA measurements such as those shown in **a** and **b**.

Capacitive Recording Mode

In the capacitive mode, the electrical double layer at each metal-coated nanowire's tip serves as a capacitor[118] that follows fast changes in the membrane potential. Specifically, the charging/discharging of this double layer leads to a change in the VNE voltage that can be amplified via AC coupled amplifiers. The voltages measured at the VNE (Fig. A.3b) are typically 300 times smaller than those measured with a patch pipette due to a capacitive voltage division by the ratio of the total nanowire double-layer capacitance (C_{NW} in Fig. A.3c, ~0.5 pF in our prototype device) to the parasitic capacitance to ground (C_p, ~150 pF). Often an initial voltage pulse of ±3 V for 100 ms is required to establish an intracellular recording in the capacitive mode, and, at times, a brief re-permeabilization pulse is necessary to re-establish intracellular access if the signal amplitude decreases due to the recovery of the cellular membrane. Recording times in the capacitive regime can last up to several hours, mainly limited by cell viability in ambient conditions or the effect of a patch pipette, if the cell is simultaneously patched.

Analysis of Stimulation Coupling Modes

Stimulation coupling, similarly to recording coupling, can be achieved via two distinct coupling modes: Faradaic and capacitive. Figure A.4 summarizes the characterization of the two coupling modes simulated and measured pre- and post-synaptic activity. As depicted in the schematic of the experimental setup (Fig. A.4a), the presynaptic stimulus was applied via the VNE while a patch pipette was used to monitor the activity of the postsynaptic neuron. Representative input (I) and output (O) traces of the presynaptic VNE voltage pulse and the post-synaptic voltage response, respectively, are shown in Fig. A.4b. We simulated the presynaptic activity to thoroughly analyze the two distinct (faradaic and capacitive) VNE stimulation-

coupling modes. Fig. A.4c – d show the simulated plots of the Faradaic current plots the displacement (capacitive) current, respectively, injected through the VNE in response to a voltage pulse (insets) of varying duration. In faradaic coupling mode, the onset of all three action potentials coincides, independent of the pulse duration (Fig. A.4e). In contrast, the onset of the action potentials stimulated via capacitive currents is directly dependent on the duration of the voltage pulse and follows the injection of positive current (Fig. A.4f). As expected from these simulations results, measured postsynaptic activity in rat cortical neurons exhibited two distinct coupling modes, faradaic and capacitive. In faradaic coupling mode, voltage pulses of varying duration (10, 20, 30, and 50ms) result in excitatory postsynaptic potentials of the same 20ms latency (Fig. A.4g). Similarly, excitatory postsynaptic potentials stimulated via capacitive coupling show a discrete distribution of latencies corresponding to the different pulse durations, as expected (Fig. A.4h).

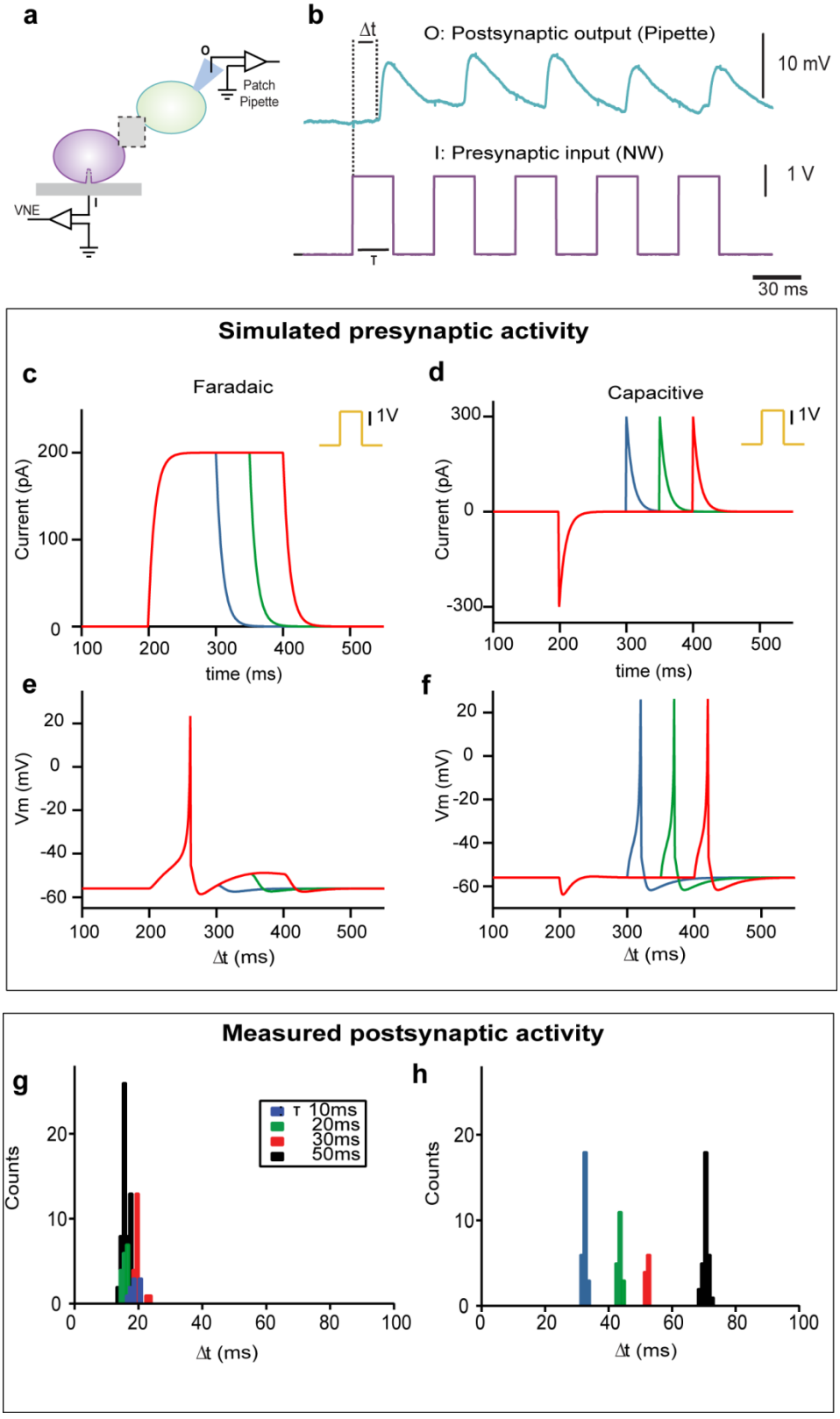

Figure A.4 | Stimulation coupling modes. a, Schematic of the experimental setup. Presynaptic stimulus (I: input) was applied via the VNE while a patch pipette was used to monitor the

Figure A.4 (Continued). activity of the postsynaptic neuron (O: output). **b,** Representative input (I) and output (O) traces of the presynaptic VNE voltage pulse and the post-synaptic voltage response, respectively. τ represents the pulse duration, while Δt represents the latency between the onset of the stimulus and the rising edge of the post-synaptic response. **c-f,** Simulated presynaptic activity show two distinct (faradaic and capacitive) VNE stimulation coupling modes. **c,** Faradaic current injected through the VNE in response to a voltage pulse (inset) of varying duration. **d,** Displacement (capacitive) current injected through the VNE in response to a voltage pulse (inset) of varying duration. Note that positive current is injected at the dropping edge of the voltage pulse. **e,** Membrane response to faradaic current stimulations of varying durations. The onset of all three action potentials coincides, independent of the pulse duration. **f,** In contrast, the onset of the action potentials stimulated via capacitive currents is directly dependent on the duration of the voltage pulse and follows the injection of positive current. **g&h,** As expected from the simulations results, measured postsynaptic activity exhibits two distinct coupling modes, faradaic and capacitive. **g,** In faradaic coupling mode, voltage pulses of varying duration (10, 20, 30, and 50ms) result in excitatory postsynaptic potentials of the same 20ms latency. **h,** Similarly, excitatory postsynaptic potentials stimulated via capacitive coupling show a discrete distribution of latencies corresponding to the different pulse durations, as expected.

A.4 Methods

Cell Culture and Imaging

Cells and cell culture media were contained within polydimethylsiloxane wells bonded to the VNEA surface. Dissociated E18 rat cortical neurons (BrainBits LLC) were cultured on top of VNEAs as previously described[89]. A three-well polydimethylsiloxane (PDMS) washer structure was used: a central double well (diameter: 3 mm, each) was employed to retain a droplet of cells above the VNEA during the initial 45 minutes needed for cell settling[22]. Two additional wells (diameter: 5 mm) were also seeded with cells so as to help support neuronal viability by conditioning the media within the larger washer structure[125] (Fig. A.1e). Prior to the addition of cells, exposed device surfaces were coated with poly-L-lysine (typically 2 – 5 nm in thickness) to promote cell adhesion and growth. Epifluorescence and DIC images of live cells were overlaid

and colored using ImageJ. False coloring of SEM images was performed using Photoshop CS3 (Adobe).

Membrane permeabilization and visualization

Typically, the membrane potential, as measured using a patch pipette, responded immediately to the application of current via the VNEA pad (-200 to -400 pA), suggesting that some of the nanowires formed a tight seal with the cell membrane and penetrated the cells on top. In the absence of immediate electrical coupling, permeabilization could be achieved by applying 100 ms voltage pulses with amplitudes of ~ ±3 V. Membrane permeabilization was typically accompanied by a depolarization of V_m by 10 ~ 20 mV; lowering the holding current on the recording pad or the patch pipette reversed this depolarization. Confocal microscopy imaging of cortical neurons cultured on vertical silicon nanowires (3 days *in vitro* (DIV)) showed that some neurons appeared penetrated by nanowires while others did not, consistent with our electrical measurements (Fig. 3.3). Images were obtained by labeling the nanowires with Alexa647-SE in DMSO (1mg/mL, Invitrogen)[89]. After a 30-minute incubation at 37^{o}C, samples were washed three times through water, blown dry, and used as a substrate for neuron culture. Prior to imaging, neuronal membranes were labeled by incubating the samples in extracellular solution containing 1:100 Vybrant DiI (Invitrogen) at room temperature. Images were then analyzed and reconstructed in 3D using Imaris 6.2 (Bitplane).

Patch Pipette Recording

During measurements, VNEA substrates were bathed in a solution containing [in mM]: NaCl [119], KCl [5], HEPES [20], $CaCl_2$ [2], $MgCl_2$ [2], glucose [30], and glycine [0.001]. The pH of the solution was 7.3 and the osmolarity was 330 mosM (adjusted with sucrose). Patch pipettes were pulled to have resistances of 2 ~ 10 MΩ and then backfilled with a solution containing [in mM]: potassium gluconate [130], KCl [10], $MgCl_2$ [5], EGTA [0.6], HEPES [5], $CaCl_2$ [0.06], Mg-ATP [2], GTP [0.2], leupeptine [0.2], phosphocreatine [20], and creatine phosphokinase [50 U/ml] with the pH at 7.2[126]. For certain experiments, high-purity calcein (Invitrogen) was added (1 part in 5000) into the intracellular recording solution to enable fluorescence imaging of the patched cell. All recordings were made at room temperature with a Multiclamp 700B (Molecular Devices). Current-clamp recordings of HEK293 cells were performed with a holding current of 0 pA. During neuronal measurements, the holding current was adjusted to bring the neuron to a resting membrane potential near -70 mV for stimulation and recording experiments, and -40 mV for PSP identification. The pipette capacitance was corrected electronically. All acquisitions were performed using the pCLAMP 10 software (Molecular Devices) and analyzed and plotted using Clampfit 10 (Molecular Devices) and Matlab (Mathworks).

Protocols for VNEA stimulation and recording

For VNEA stimulation and recording experiments, the devices were mounted in a custom-built aluminum enclosure designed to provide both electrical connection to the VNEA pads and electromagnetic shielding. The connection between the VNEA and

stimulation/measurement electronics was achieved using conductive elastomeric connectors (ZEBRA, Fuji-poly) and a custom-built printed circuit board.

Neuronal stimulation was achieved using a 32-channel analog output module (National Instruments PXI-6723) and control software written in LabView (National Instruments). During VNEA stimulation, capacitive electronic cross-talk between the patch pipette and VNEA was removed by subtracting the characteristic transients. Current-clamp measurements were performed using a custom-built current-clamp circuit with stability on the order of 10 pA and compliance values between +/-10 V and +/- 5nA. Currents were controlled using our analog output module, and recorded voltages were amplified using AM Systems Model 1800 (gain: 100×, bandwidth: 1 Hz - 20 kHz). Both pre- and post-amplified voltages were collected and digitized. Capacitively-coupled measurements were recorded directly with the AM Systems amplifier, and digitally filtered to remove 120Hz line noise. To preserve the simultaneity of the pipette and VNEA measurements, all signals were recorded and digitized simultaneously using the pCLAMP 10 software and a 16-channel analog data acquisition system (Axon Digidata 1322A, Molecular Devices).

Steady-state control of the membrane potential (as measured by the patch pipette (V_p)) could be achieved for several seconds by changing the offset voltage applied to the nanowires (V_{NW}) (Fig. 3.5).

PSP identification

To identify excitatory (EPSPs) and inhibitory PSPs (IPSPs), we patched a rat cortical neuron (14 DIV) in whole-cell current-clamp mode. Several representative EPSPs/IPSPs were manually identified and averaged to form a template (Fig. A.3b). Once a template was obtained, automatic

event detection was performed using Clampfit 10. Latencies were calculated as the interval between the rising edge of the stimulus and the peak of the PSP. Data was then compiled and plotted using Matlab.

A.5 Initial Results of High-throughput Study of Synapses and Network Dynamics *In Vitro*

The VNEA device enables parallel stimulation and measurement of mammalian neuronal activity. Voltage pulses applied to the VNE with respect to the reference electrode result in current being injected intracellularly, which in turn reliably excites action potentials (Fig. A.5a). Simultaneous whole-cell patch-clamp measurements show that the stimulation probability depends sigmoidally on the magnitude of the current injected through the nanowires (Fig. A.5b). Furthermore, in the current-clamp mode, the VNEA reliably records single-shot action potentials with a signal-to-noise ratio of 100:1 (Fig. A.5c). This signal-to-noise ratio can be improved to >1000:1 by averaging multiple waveforms obtained under identical experimental conditions. Having demonstrated these capabilities, we utilized our VNEA to modulate *in vitro* neuronal circuits (Fig. A.5d – g). In particular, we implemented paired VNE-patch pipette stimulations to modify synaptic strengths according to spike-timing-dependent plasticity rules. Briefly, stimulation of a presynaptic neuron on top of the VNE (cell A) results in an excitatory postsynaptic potential (PSP) in cell B as recorded using a patch pipette in a whole cell configuration (Fig. A.5d). To depress the synaptic strength, an action potential was evoked in cell B 40ms prior to VNE stimulation (Fig. A.5e, (i)). This paired stimulation was repeated 40 times every 1 s. To potentiate the synapse an action potential was evoked 40 ms after VNE stimulation and repeated as in the prior training protocol (Fig. A.5e, (i)). As expected from spike-timing-dependent plasticity rules, the synaptic strength, or average EPSP amplitude, decreases

following protocol (i – red) and recovers following protocol (ii – blue). In addition, bar chart of the average normalized EPSP amplitude show a 20% depression followed by 20% potentiation in response to the training protocols i and ii, respectively.

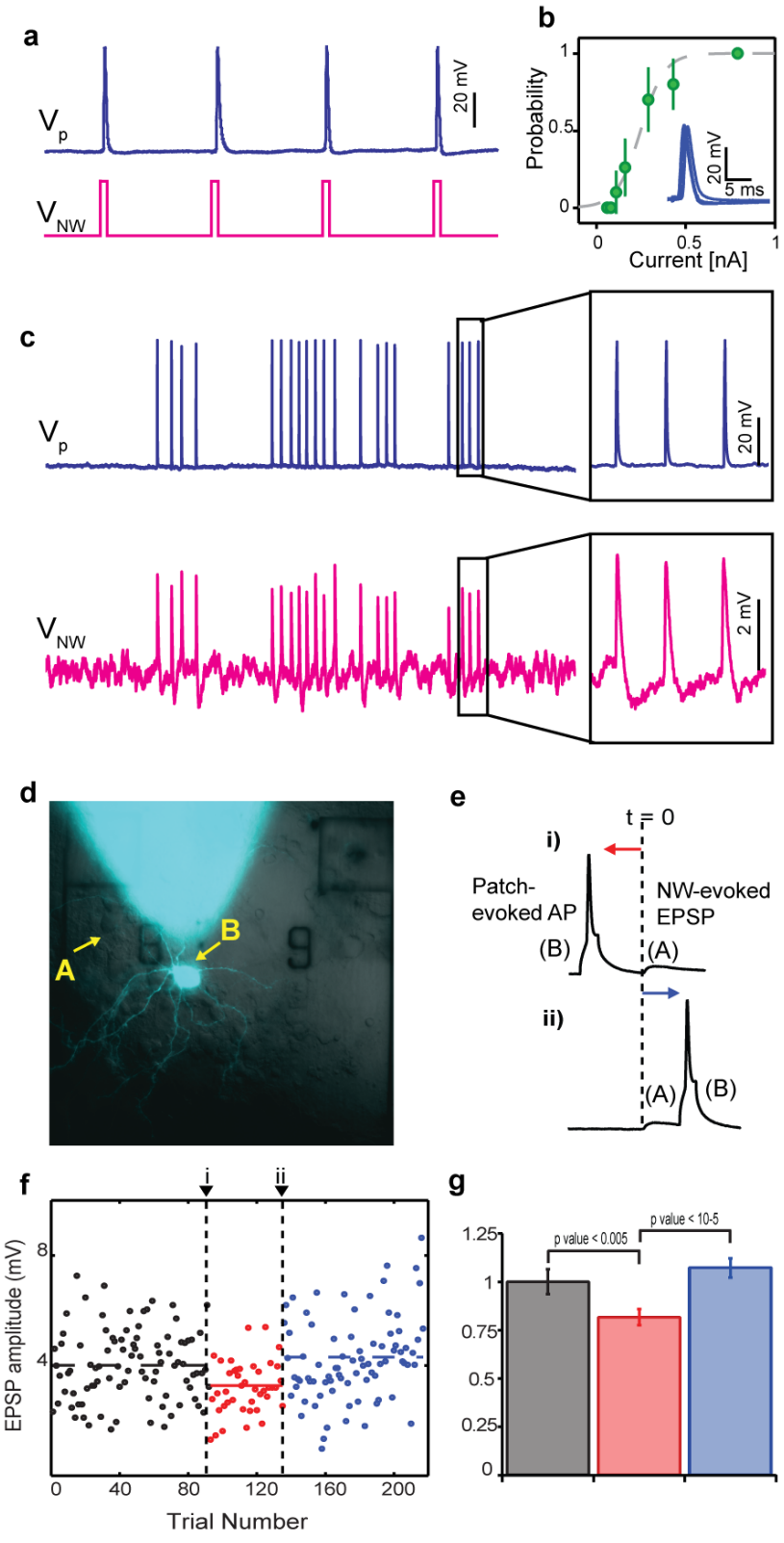

Figure A.5 High-throughput study of synapses and network dynamics *in vitro* a, Action potentials were reliably stimulated by voltage pulses applied to a VNE (magenta) and

Figure A.5 (Continued). recorded using a patch pipette (blue). **b,** Probability of action potential (AP) excitation plotted as a function of current injected by nanowires shows a sigmoidal dependence (dashed line), which is similar to AP excitation elicited by intracellular patch pipettes. Probabilities were calculated for 20 trials and plotted as a function of the stimulation current. Error bars represent 95% confidence intervals. Inset: five consecutive time-aligned action potentials stimulated by nanowire current injection show less than 1 ms jitter. **c,** The VNE can also measure action potentials (magenta) that were stimulated using a patch pipette (blue) . VNEA measurements show good agreement with those obtained simultaneously by a patch pipette. **d-g,** Paired VNE-patch pipette stimulation modify synaptic strengths according to spike-timing-dependent plasticity rules. **d,** Composite bright-field and fluorescence image of a cortical neuron patched and backfilled with calcein (13 DIV). **e,** Stimulation of a presynaptic neuron on top of the VNE (cell A) results in an excitatory postsynaptic potential (PSP) in cell B as recorded using a patch pipette in a whole cell configuration. To depress the synaptic strength, an action potential was evoked in cell B 40ms prior to VNE stimulation (i). This paired stimulation was repeated 40 times every 1 s. To potentiate the synapse an action potential was evoked 40 ms after VNE stimulation and repeated as in the prior training protocol (ii) **f,** As expected from spike-timing-dependent plasticity rules, the synaptic strength, or average EPSP amplitude (horizontal dashed lines), decreases following protocol (i - red) and recovers following protocol (ii - blue). **g,** Bar chart of the average normalized EPSP amplitude showing a 20% depression followed by 20% potentiation in response to the training protocols i and ii, respectively.

A.6 MATERIALS

REAGENTS

- E18 hippocampus and cortex without the subventricular region (BrainBits, cat. no. HPCtx)
- Dental wax (Gumbrand, cat. no. 724RQD)
- TrypLE Express (Gibco, cat. no. 12604)
- 100% Ethanol (VWR)
- Refer Table 1 for media reagents

EQUIPMENT

- VNEA device with PDMS well
- Zebra Elastomeric Connector (Fujipoly, cat. no. S5002 8Z100)
- Custom-made PCB
- Custom-made aluminum enclosure
- Custom-made IC module
- Reference electrode, Ag/AgCl pellets (Warner Instruments, cat. no .64-1309)
- Connector pins (Warner Instruments, cat. no. 64-1326)
- Various cables, including rainbow and BNC cables (Warner Instruments)
- Shielded Connector Block, (BNC 2100, National Instruments, cat. no. 777643-01)
- Amplifier (AM systems, model 1800 2-channel microelectrode AC amplifier, cat. no. 700000)
- Data acquisition system (Axon Instruments/Molecular Devices, Digidata 1322A, with pCLAMP 10 software)
- DC power supply (Agilent Technologies, cat. no. E3617A)
- Upright microscope with water immersion objective (Olympus BX61WI, UMPlanFi 20×/0.5)
- Air table (Newport)
- Digital microscope camera (QImaging)
- Digital Voltmeter (Fluke, cat. no. IV-77-4)
- Control software (LabView)
- Desktop computer

NEURON CULTURE

Neuronal culture

- Plasma cleaner (Harrick Plasma, cat. no. PDC-32G)
- Convection oven (Yamato DX300)
- Shaker (VWR, cat. no. 89032-088)
- Water bath (VWR, cat. no. 97025-110)
- Alconox liquid detergent (VWR, cat. no. 89092-536)
- Laminar flow hood (Nuaire)
- Cell culture incubator (Thermo Scientific, cat. no. 3307-MAR)
- Bunsen burner (VWR, cat. no. 89038-530)
- Glass pipettes (VWR, cat. no. 53499-630)
- Extended length plastic pipette tips (Rainin cat. no. RT-l250XS)
- Scalpel (BD Bard-Parker no. 23 or 24, cat. no. 371223)
- 1.5 ml Microcentrifuge tubes (Eppendorf, cat. no. 022364111)
- 60 mm Petri dish (BD, cat. no. 354401)
- 15 mL conical-bottom centrifuge tube (BD cat. no. 352097)
- 10 mL syringe (BD cat. no. 309604)
- Spec-Wipe wipers (VWR cat. no. 21914-758)
- Acrodisc syringe filter (Pall Life Sciences cat. no. PN 4192)
- Hemocytometer (iN CYTO cat. no. DHC-N01-5)

PATCH CLAMPING (OPTIONAL)

- Micropipette puller (Sutter P series Flaming/Brown pipette puller; Sutter Instruments Model P-97)
- Borosilicate pipettes (Warner Instruments, 64-0790)
- Micromanipulators (Sutter Instruments, ROE-200)
- Current- and voltage-clamp head stage (Axon Instruments, CV-7B)
- Current- and voltage-clamp module (Axon Instruments, Multiclamp 700B)
- Data acquisition system (Axon Instruments/Molecular Devices, Digidata 1322A, with pCLAMP 10 software)
- Tygon tubing (US Plastics, cat. no. 57102))
- Connectors for tubing (Harvard Apparatus, cat. no. 721410)
- 1 mL syringes (VWR, cat. no. 53548-001)

A.7 PROCEDURE

Steps 1-5: Preparation of a VNEA device

1. To prepare a VNEA device for neuronal culture, clean the device in oxygen plasma (10 min, 50 W, 40 sccm O_2).
2. Sterilize the device in 100% ethanol for 30 minutes (min) and transfer it to the laminar flow hood. *Note: All procedures from this step on are to be conducted under sterile conditions.*

3. Rinse the VNEA device three times in double-distilled water (dd-water) and transfer it to a sterile 60-mm petri dish. Using a plastic pipette tip, carefully aspirate any remaining water. Allow the device to dry completely (~10 min).

4. Carefully add 300 μL of mixed poly-L-lysine solution to the PDMS wells, or as much as is needed to fill the wells without spilling over. Cover the dishes and incubate the device for two hours.

Critical step: The poly-L-lysine solution must not dry out during incubation.

5. Using a plastic pipette tip, aspirate the poly-L-lysine from the VNEA device. Rinse the PDMS well with dd-water, aspirate, and allow it to dry.

Critical step: Steps 1-3 can be completed a day before neuron plating. However, the poly-L-lysine treatment should be done on the same day as the neuronal culture.

Steps 6-17: Neuron dissociation, plating, and culture[119,165-167]

6. Half an hour prior to neuron dissociation and plating, pre-warm Culture Media + Glu to 37°C in a water bath (8 mL per VNEA device, plus 5-10 mL for the culture). Also, pre-warm a 50 mL aliquot of 9:1 Media.

7. Neurons used for plating are E18 rat combined hippocampal and cortical neurons (BrainBits, LLC). Store the neurons at 4°C until ready to use. Transfer the vial of neurons to the laminar flow hood, along with 50 mL cold Modified HBSS Solution, divided into 10 mL and 40 mL aliquots.

8. To the 10 mL aliquot of Modified HBSS Solution, add 100 μL of 100x Enzyme Solution, 200 units of papain, and 100 μL of DNAse I. Mix thoroughly and filter-sterilize. Set aside.

9. Carefully remove the media containing neurons from the vial and transfer to the lid of a 60-mL petri dish. If there are any large pieces, cut with a scalpel. Transfer the neurons to a 14-mL Falcon tube, add ~13 mL of Modified HBSS Solution (without enzymes), and allow neurons to settle to the bottom (1-2 min). Aspirate most of the media out of the Falcon tube and rinse the neurons with ~13 mL of Modified HBSS Solution (without enzymes). Repeat the settling and rinsing once more.

10. Aspirate the Modified HBSS Solution from the Falcon tube one final time and add the 10 mL aliquot of Modified HBSS Solution mixed with enzymes. Transfer the 14-mL tube containing the neurons to a tissue culture incubator set to 37□C and 5% CO_2. Loosen the cap of the Falcon tube to allow equilibration. Incubate for 30 min. **Critical step**: The incubation should not exceed 30 min. During the 30-min incubation, also transfer the pre-warmed Culture Media + Glu and 9:1 Media to the tissue culture incubator. Loosen the caps to allow equilibration.

11. Following the 30-min incubation, bring the Falcon tube containing neurons and the tubes of equilibrated Culture Media + Glu and 9:1 Media into the laminar flow hood. Carefully aspirate the media from the Falcon tube and rinse it with 9:1 Media. Allow the neurons to settle and repeat the rinse twice more.

12. Aspirate as much media as possible from the Falcon tube and re-suspend the neurons in 1 mL Culture Media + Glu. Using a small diameter pipette tip, gently pipette up and down six to ten times to re-suspend the neurons (until the neurons appear to be evenly dispersed). **Critical Step:** Do not over-pipette. This will result in reduced cell viability.

13. Using a hemacytometer, count the neurons and dilute the cell suspension to a concentration of 1 x 10^6 cells/mL. Plate 2.5 x 10^5 neurons per VNEA device. Incubate the device at 37°C for 30 min, allowing the neurons to settle on the surface. Return the Culture Media + Glu to the incubator for this time as well, leaving the cap loose.

14. After the 30-min incubation, very slowly and carefully, add 8 mL Culture Media + Glu to a 60-mm petri dish containing the VNEA device. The entire device should be submerged.

15. Culture the petri dish that contains the VNEA device with plated neurons for 6-14 days (until ready to record) at 37°C and 5% CO_2 to allow neuron maturation and synaptogenesis.

16. The day after plating, change out 30% of the media from the petri dish.

17. Continue to perform a 30% media swap every 3-4 days. After 7 days in vitro (DIV), start to use Culture Media - Glu.

Steps 18-29: Mounting the device (Fig. A.6)

18. Check neuron viability in an upright microscope to ensure that the neurons on the VNEA are healthy and that cells are resting on top of the electrodes.

19. Identify and note the pads with neurons residing on top of them (e.g., Fig. A.6b).

20. Carefully remove the device from the media dish and place it on a Spec-Wipe wiper. **Critical step:** The PDMS culture well should not dry out at any point.

21. Spray a clean wipe with dd-water and wipe the metal contact pads at the bottom of the VNEA device from top to bottom to remove any residual salt. Repeat as needed to achieve a clean surface. **Critical step**: Complete removal of salt residue is important to

prevent electrical shorting of the metal contact pads when they are connected to the control electronics.

22. Spray another wipe with 70% ethanol and further clean the metal contact pads by wiping top to bottom. **Critical step:** Be careful not to make contact to the media well with the alcohol wipe.

23. Mount the device in the holder. Align the metal contact pads to the PCB contacts, press the VNEA device flush to the PCB and clamp it in place. **Critical step:** Make sure the height of the VNEA chip matches the PCB. Height mismatches can lead to over- or under-compression of the zebra rubber and poor electrical contact. Pieces of scotch tape can be used to shim the VNEA chip to match the PCB height (Fig. A.6b).

24. Carefully position the zebra rubber on top of the device and PCB contacts (Fig. A.6c). Tighten the zebra rubber screws finger tight and use a digital multimeter (DMM) to measure the resistance between the two device layer contacts (S1 and S2) by probing the corresponding connectors at the bottom of the PCB (Fig. A.6c). Resistance should read ~100 kΩ. Then check the resistance between each VNE (metal contact pads 1 through 16) and the device layer (metal contact pads S1 or S2). The resistance between the contact pads and device layer should be large enough to overload the DMM (typically >50 MΩ). If the resistance between the VNE and the device layer is <50 MΩ it will not be possible to record signals using this electrode. **Critical step:** Zebra rubber is designed to operate at 5-25% compression. Over- or under-compression can lead to poor electrical contact. See **Troubleshooting**

25. Place a reference electrode in the PDMS well and secure it using dental wax. Make sure it is connected to the return port of the custom-made IC module.

26. Connect the I-out port from the IC module to the connector on the PCB that corresponds to a bare VNE (without neurons on top). This will be used to check proper electrical contact (be sure to select a VNE that you do not intend to use for an experiment).

27. Place the aluminum enclosure over the PCB and fasten with screws.

28. *Optional*: Carefully slide the enclosure under the microscope.

29. Double check that the electrical connections are still in place after moving the enclosure.

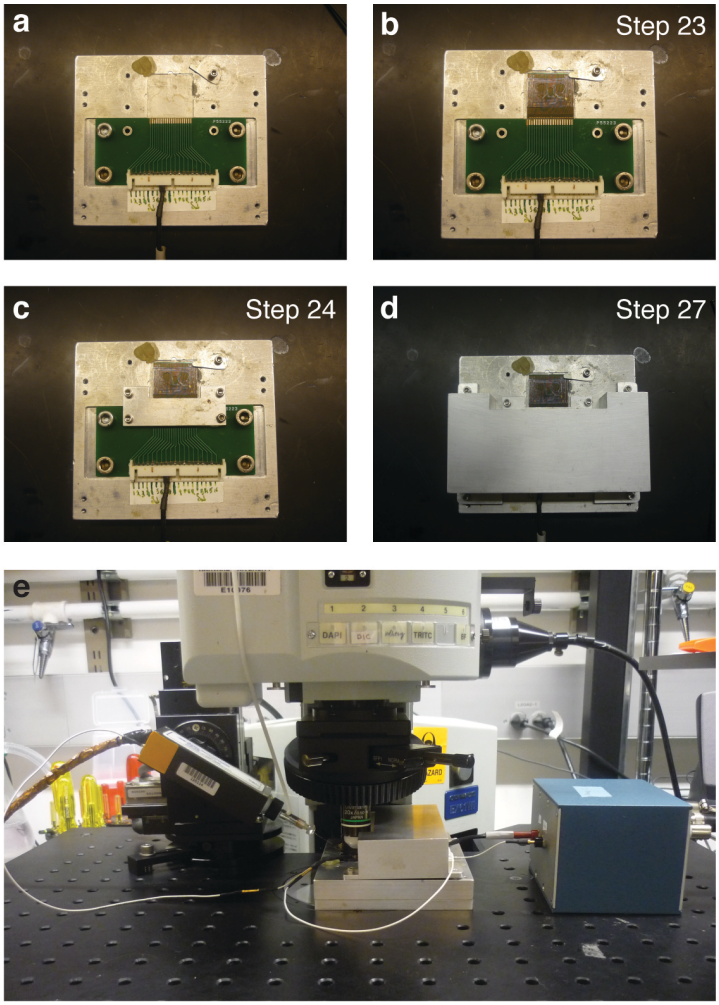

Figure A.6 | Mounting of the device. a, Top view of the aluminum enclosure base containing a printed circuit board (PCB) with one pad connected to the IC module. **b,** A VNEA

Figure A.6 (Continued). device mounted on the aluminum enclosure base with contact pads aligned to the contacts on the PCB and held in place by an aluminum clip. **c,** Zebra rubber (under the metal clamp) screwed in place to connect the device contact pads to the PCB pads. **d,** Aluminum enclosure top covering the PCB provides electromagnetic shielding. **e,** Side view of the aluminum enclosure with a VNEA positioned under an upright microscope (top). A reference electrode placed in the bath solution connects to both the IC module (right) and the patch-clamp head stage (left).

Steps 30-36: RC Time constant characterization

30. Measure the voltage-dependent RC time constant of a VNE that is not intended for neuronal measurement. This measurement is to confirm good electrical contact between the PCB and VNEA.

31. Using a voltage source, command the custom-made IC module to apply a 600 pA pulse through the VNE for 300 ms.

32. Increase or decrease the offset current by 200 pA. Wait 2-3 seconds for the electrode to stabilize, and stimulate again.

33. Repeat step 32 until holding at ±6 nA.

34. If traces show large voltage fluctuations (> 20 mV), repeat steps 31-33 to condition the VNE.

35. Due to the non-linear I-V relationship of electrochemical reactions at the nanowire tip, the VNE access resistance should decrease as the absolute value of the offset current increases. Thus, the voltage needed to drive the 1.5-nA current pulse (as well as the RC time constant) should decrease as the magnitude of the holding current increases (see Fig. A.6c). If the recorded waveforms do not follow this trend, try to record from another VNE. If the traces still do not show the expected trend, there is likely an electrical short, and you should fix this problem (Step 24).

36. *Note:* The same procedure can be used at the end of the experiment to extract the RC time constant of the individual electrode pads, as detailed in the introduction.

Steps 37-40: Stimulation via current injection with the VNE

37. *Optional:* Patch the neuron of interest in whole-cell mode for simultaneous measurement[60,160,161].

38. Permeabilize the cellular membrane to ensure nanowire intracellular access. This procedure can be performed by injecting a short current pulse through the nanowires (duration: 100 ms, magnitude: ± 1 nA to 3 nA). A brief drop in the membrane resistance will accompany this permeabilization procedure but will typically recover to the original value within a few seconds.

39. Stimulate the neuron by injecting a current pulse through the nanowires. Current pulses 10 ms in duration and 200-400 pA in magnitude can reliably excite action potentials (Fig. A.6d). Lower magnitude pulses can be used to shift the membrane potential without eliciting an action potential. Repeat as needed.

40. *Optional*: Monitor the neuron's response via the patch pipette. When this procedure is used, the experimental duration will be limited to the time that a stable patch clamp can be maintained. See **Troubleshooting**

41. *Optional*: To stimulate at multiple pads during a single experiment, use a ribbon connector to connect all of the outputs on the PCB directly to the analog out channels of a 16-channel data acquisition (DAQ) module.

Steps 41-43: Measurement of neuronal activity in the Faradaic mode

42. Alternatively, utilize the VNE to monitor the neuronal activity in current-clamp mode.

43. Set the VNE holding current to ±750pA. Lower/raise this holding current in increments of 100pA until the VNE begins to record a signal. Record the voltage trace using a data acquisition module of choice. **Critical step:** Lowering/raising the holding current reduces/increases the nonlinear VNE resistance. Special attention must be paid not to inject a large current into the cell (i.e. large holding current) in order to minimize cellular damage. **Timing**: The recording period in the Faradaic mode can last up to 10 min and is limited by electrochemical reactions at the electrode interface within the cell. This eventually produces swelling and breakdown of the cellular membrane.

44. At the end of the experiment, the approximate access resistance and capacitances of the VNE interface can be determined using steps 29-34.

Steps 44-45: Measurement of neuronal activity in the capacitive mode

45. To operate the device in the less invasive capacitive mode, connect an AC-coupled amplifier to the PCB connectors. **Critical step:** Take care in performing this step - changing the connection to the PCB from the custom-made IC module to the AC amplifiers may break the seal of a patch pipette.

46. The output of the AC-coupled amplifier can be digitized and recorded using a data acquisition module of choice. Recordings can last up to several hours and are typically limited by cell viability in ambient conditions.

Steps 46-52: Cleaning

47. At the conclusion of an experiment, rinse the device by first spraying dd-water from a squirt bottle to physically remove the cultured neurons and rinse out the salt solution. **Critical step:** Do not allow the device to dry before washing it with dd-water

48. Transfer the rinsed device to a petri dish and add enough TrypLE to cover the device. Place the petri dish on a shaker for 20 min.

49. Rinse with dd-water.

50. Prepare another petri dish with a soap-water solution. Transfer the device to an orbital shaker and shake it for 20 min.

51. Rinse with dd-water and transfer the device to a clean petri dish with dd-water. Keep it on a shaker for 30 min.

52. Blow-dry with a nitrogen gun.

53. Store in an oven at 60°C to allow any solvents absorbed in PDMS to dry out.

A.8 TIMING

Steps 1-5: Preparation of VNEA devices - 4 h.

Steps 6-17: Cell dissociation, plating, and culture - 2 h, 6 to 14 days incubation time.

Steps 18-29: Mounting the device - 10 to 30 min.

Steps 30-36: RC time constant characterization - 15 min.

Steps 37-40: Stimulation via current injection - 1 to several hours.

Steps 41-43: Measurement of neuronal activity (Faradaic mode) - 1 to 10 min.

Steps 44-45: Measurement of neuronal activity (capacitive mode) - 1 to several hours.

Steps 46-52: Cleaning - 1 h 30 min.

A.9 TROUBLESHOOTING

Troubleshooting advice can be found in Table A.2.

Table A.1. Media and Recording solutions

Medium	Components	Final Concentration	Source
Modified HBSS Solution	10x HBSS, no Calcium, no Magnesium	99%	Life Technologies, cat. no. 14170-112
	1 M HEPES	10 mM	Life Technologies, cat. no. 15630-080
	Notes: pH to 7.3 and filter-sterilize (0.2 μm). Aliquot into sterile 50 mL tubes. Store at 4°C.		
9:1 Media	9 parts Modified HBSS Solution	90%	
	1 part FBS Qualified One Shot	10%	Life Technologies, cat. no. 10437-077
	Notes: Filter-sterilize (0.2 μm) and aliquot into 50 mL tubes. Store at 4°C.		
100x Enzyme Solution	L-cysteine	20 mg/mL	Sigma-Aldrich, cat. no. C7352
	EDTA	50 mM	Sigma-Aldrich, cat. no. EDS-100G
	CaCl2	150 mM	EMD Millipore, cat. no. 3000-500GM
	Notes: Store at 4°C.		
Papain	Papain	200 units/mL	Sigma-Aldrich, cat. no. 76218
	Notes: Store at -20°C.		
DNase I	Dnase I	500 units/mL	Life Technologies, cat. no. 18047-019
	Notes: Store at -20°C.		

Table A.1
(Continued)

Culture Media + Glu	Neurobasal Medium	98%	Life Technologies, cat. no. 21103-049
	B-27 Serum-Free Supplement (50x)	2%	Life Technologies, cat. no. 17504-044
	200 mM L-Glutamine	0.5 mM	Life Technologies, cat. no. 25030-081
	L-Glutamic acid	25 uM	Sigma-Aldrich, cat. no. 49449
	Notes: Filter-sterilize (0.2 µm) and aliquot into 50 mL tubes. Store at 4°C.		
Culture Media - Glu	Neurobasal Medium	98%	Life Technologies, cat. no. 21103-049
	B-27 Serum-Free Supplement (50x)	2%	Life Technologies, cat. no. 17504-044
	200 mM L-Glutamine	0.5 mM	Life Technologies, cat. no. 25030-081
	Notes: Filter-sterilize (0.2 µm) and aliquot into 50 mL tubes. Store at 4°C.		
Mixed Poly-L-Lysine Solution	poly-L-lysine solution, mol. wt. 70,000-150,000	50%	Sigma-Aldrich, cat. no. P4707
	poly-L-lysine solution, mol. wt. 150,000-300,000	50%	Sigma-Aldrich, cat. no. P4832
	Notes: Filter-sterilize (0.2 µm) and store at 4°C.		
Intracellular Recording Solution	Potassium-D-Gluconate, 99%	136.5 mM	Alfa Aesar, cat. no. B25135
	Potassium Chloride	17.5 mM	Sigma-Aldrich, cat. no. P9333
	Sodium chloride, crystalline powder PDV, 99+%	9 mM	Alfa Aesar, cat. no. A12313
	Magnesium chloride hexahydrate	1 mM	Alfa Aesar, cat. no. 36226

Table A.1 (Continued)			
	HEPES	10 mM	Sigma-Aldrich, cat. no. H3375
	EGTA	0.2 mM	Sigma-Aldrich, cat. no. E4378
	Notes: pH to 7.2 and filter-sterilize (0.2 μm). Aliquot into sterile 50 mL tubes. Store at 4°C.		
Extracellular Recording Solution	Sodium chloride, crystalline powder PDV, 99+%	145 mM	Alfa Aesar, cat. no. A12313
	Potassium Chloride	3 mM	Sigma-Aldrich, cat. no. P9333
	HEPES	10 mM	Sigma-Aldrich, cat. no. H3375
	Calcium chloride dihydrate	3 mM	Alfa Aesar, cat. no. 33296
	D-(+)-Glucose	8 mM	Alfa Aesar, cat. no. A16828
	Magnesium chloride hexahydrate	2 mM	Alfa Aesar, cat. no. 36226
	Notes: pH to 7.3 and filter-sterilize (0.2 μm). Aliquot into sterile 50 mL tubes. Store at 4°C.		

Table A.2. Troubleshooting table

Step	Problem	Possible reason	Solution
24	The DMM overloads when measuring the resistance between the device and the PCB contacts.	• Poor contact between the zebra rubber and the device metal contact pads.	• Tighten the zebra rubber and measure the resistance again. Repeat as necessary until the resistance reads ~100kΩ.
24	VNE-device layer shorting: The DMM does not display a steady overload (> 50 MΩ) when measuring between a VNE and the device layer.	• Height misalignment between the VNEA and PCB or over compression of zebra rubber. • Media leaking from the PDMS well. • Salt residue on pads or zebra rubber.	• Try loosening the zebra rubber such that you still have contact between the two substrate-pads. Double check that you have aligned the heights properly. • Check for leaking media around the base of the PDMS by aspirating excess media and drying the sample. Next, refill the media and check for the re-wetting at the base of the PDMS well. If sample leaks through the PDMS, it will need to be resealed before performing an experiment. • Take sample out; look for signs of solution on the zebra rubber (due to leaks that might have been hard to see). Carefully clean the contacts and zebra rubber again with ethanol and try again.
40	Action potentials can't be stimulated	• Low amplitude current pulse	• Increase the amplitude of the current pulse in steps of 100pA. The exact threshold for stimulation can vary between cells and electrodes.

REFERENCES

1 Yang, C., Zhong, Z. & Lieber, C. M. Encoding electronic properties by synthesis of axial modulation-doped silicon nanowires. *Science* **310**, 1304-1307, doi:10.1126/science.1118798 (2005).

2 Lu, W. & Lieber, C. M. Nanoelectronics from the bottom up. *Nature materials* **6**, 841-850, doi:10.1038/nmat2028 (2007).

3 Li, Y., Tan, B. & Wu, Y. Mesoporous Co3O4 nanowire arrays for lithium ion batteries with high capacity and rate capability. *Nano letters* **8**, 265-270, doi:10.1021/nl0725906 (2008).

4 Huang, J. Y. *et al.* In situ observation of the electrochemical lithiation of a single SnO(2) nanowire electrode. *Science* **330**, 1515-1520, doi:10.1126/science.1195628 (2010).

5 Cui, L. F., Ruffo, R., Chan, C. K., Peng, H. & Cui, Y. Crystalline-amorphous core-shell silicon nanowires for high capacity and high current battery electrodes. *Nano letters* **9**, 491-495, doi:10.1021/nl8036323 (2009).

6 Wang, J., Gudiksen, M. S., Duan, X., Cui, Y. & Lieber, C. M. Highly polarized photoluminescence and photodetection from single indium phosphide nanowires. *Science* **293**, 1455-1457, doi:10.1126/science.1062340 (2001).

7 Qian, F. *et al.* Multi-quantum-well nanowire heterostructures for wavelength-controlled lasers. *Nature materials* **7**, 701-706, doi:10.1038/nmat2253 (2008).

8 Huang, M. H. *et al.* Room-temperature ultraviolet nanowire nanolasers. *Science* **292**, 1897-1899, doi:10.1126/science.1060367 (2001).

9 Gudiksen, M. S., Lauhon, L. J., Wang, J., Smith, D. C. & Lieber, C. M. Growth of nanowire superlattice structures for nanoscale photonics and electronics. *Nature* **415**, 617-620, doi:10.1038/415617a (2002).

10 Xie, C., Lin, Z., Hanson, L., Cui, Y. & Cui, B. Intracellular recording of action potentials by nanopillar electroporation. *Nature nanotechnology* **7**, 185-190, doi:10.1038/nnano.2012.8 (2012).

11 Tian, B. *et al.* Three-Dimensional, Flexible Nanoscale Field-Effect Transistors as Localized Bioprobes. *Science* **329**, 830-834 (2010).

12 Qing, Q. *et al.* Free-standing kinked nanowire transistor probes for targeted intracellular recording in three dimensions. *Nature nanotechnology* **9**, 142-147, doi:10.1038/nnano.2013.273 (2014).

13 Jiang, Z., Qing, Q., Xie, P., Gao, R. & Lieber, C. M. Kinked p-n junction nanowire probes for high spatial resolution sensing and intracellular recording. *Nano letters* **12**, 1711-1716, doi:10.1021/nl300256r (2012).

14 Cui, Y., Wei, Q., Park, H. & Lieber, C. M. Nanowire nanosensors for highly sensitive and selective detection of biological and chemical species. *Science* **293**, 1289-1292, doi:10.1126/science.1062711 (2001).

15 Yang, C., Zhong, Z. H. & Lieber, C. M. Encoding electronic properties by synthesis of axial modulation-doped silicon nanowires. *Science* **310**, 1304-1307, doi:Doi 10.1126/Science.1118798 (2005).

16 Yan, H. *et al.* Programmable nanowire circuits for nanoprocessors. *Nature* **470**, 240-244, doi:Doi 10.1038/Nature09749 (2011).

17 Gudiksen, M. S., Lauhon, L. J., Wang, J., Smith, D. C. & Lieber, C. M. Growth of nanowire superlattice structures for nanoscale photonics and electronics. *Nature* **415**, 617-620, doi:Doi 10.1038/415617a (2002).

18 Cui, Y., Duan, X. F., Hu, J. T. & Lieber, C. M. Doping and electrical transport in silicon nanowires. *J Phys Chem B* **104**, 5213-5216, doi:Doi 10.1021/Jp0009305 (2000).

19 Tian, B. *et al.* Coaxial silicon nanowires as solar cells and nanoelectronic power sources. *Nature* **449**, 885-889, doi:10.1038/nature06181 (2007).

20 Kempa, T. J., Day, R. W., Kim, S. K., Park, H. G. & Lieber, C. M. Semiconductor nanowires: a platform for exploring limits and concepts for nano-enabled solar cells. *Energ Environ Sci* **6**, 719-733, doi:Doi 10.1039/C3ee24182c (2013).

21 Lieber, C. M. Semiconductor nanowires: A platform for nanoscience and nanotechnology. *Mrs Bull* **36**, 1052-1063, doi:Doi 10.1557/Mrs.2011.269 (2011).

22 Cui, Y., Wei, Q. Q., Park, H. K. & Lieber, C. M. Nanowire nanosensors for highly sensitive and selective detection of biological and chemical species. *Science* **293**, 1289-1292, doi:Doi 10.1126/Science.1062711 (2001).

23 Cohen-Karni, T., Timko, B. P., Weiss, L. E. & Lieber, C. M. Flexible electrical recording from cells using nanowire transistor arrays. *P Natl Acad Sci USA* **106**, 7309-7313, doi:Doi 10.1073/Pnas.0902752106 (2009).

24 Gao, R. X. *et al.* Outside Looking In: Nanotube Transistor Intracellular Sensors. *Nano letters* **12**, 3329-3333, doi:Doi 10.1021/Nl301623p (2012).

25 Tian, B. Z. & Lieber, C. M. Synthetic Nanoelectronic Probes for Biological Cells and Tissues. *Annu Rev Anal Chem* **6**, 31-51, doi:Doi 10.1146/Annurev-Anchem-062012-092623 (2013).

26 Xie, C., Lin, Z. L., Hanson, L., Cui, Y. & Cui, B. X. Intracellular recording of action potentials by nanopillar electroporation. *Nature Nanotechnology* **7**, 185-190, doi:Doi 10.1038/Nnano.2012.8 (2012).

27 Xie, P., Xiong, Q. H., Fang, Y., Qing, Q. & Lieber, C. M. Local electrical potential detection of DNA by nanowire-nanopore sensors. *Nature nanotechnology* **7**, 119-125, doi:Doi 10.1038/Nnano.2011.217 (2012).

28 Yao, J. *et al.* Nanowire nanocomputer as a finite-state machine. *P Natl Acad Sci USA* **111**, 2431-2435, doi:Doi 10.1073/Pnas.1323818111 (2014).

29 Hallstrom, W. *et al.* Gallium phosphide nanowires as a substrate for cultured neurons. *Nano letters* **7**, 2960-2965, doi:Doi 10.1021/Nl070728e (2007).

30 Jiang, K. *et al.* Medicinal Surface Modification of Silicon Nanowires: Impact on Calcification and Stromal Cell Proliferation. *Acs Appl Mater Inter* **1**, 266-269, doi:Doi 10.1021/Am800219r (2009).

31 Kim, W., Ng, J. K., Kunitake, M. E., Conklin, B. R. & Yang, P. D. Interfacing silicon nanowires with mammalian cells. *J Am Chem Soc* **129**, 7228-+, doi:Doi 10.1021/Ja071456k (2007).

32 Qi, S. J., Yi, C. Q., Ji, S. L., Fong, C. C. & Yang, M. S. Cell Adhesion and Spreading Behavior on Vertically Aligned Silicon Nanowire Arrays. *Acs Appl Mater Inter* **1**, 30-34, doi:Doi 10.1021/Am800027d (2009).

33 Turner, A. M. P. *et al.* Attachment of astroglial cells to microfabricated pillar arrays of different geometries. *J Biomed Mater Res* **51**, 430-441, doi:Doi 10.1002/1097-4636(20000905)51:3<430::Aid-Jbm18>3.0.Co;2-C (2000).

34 Couto, L. B. & High, K. A. Viral vector-mediated RNA interference. *Curr Opin Pharmacol* **10**, 534-542, doi:Doi 10.1016/J.Coph.2010.06.007 (2010).

35 Filion, M. C. & Phillips, N. C. Toxicity and immunomodulatory activity of liposomal vectors formulated with cationic lipids toward immune effector cells. *Biochimica et biophysica acta* **1329**, 345-356 (1997).

36 Gresch, O. *et al.* New non-viral method for gene transfer into primary cells. *Methods* **33**, 151-163, doi:Doi 10.1016/J.Ymeth.2003.11.009 (2004).

37 Guignet, E. G. & Meyer, T. Suspended-drop electroporation for high-throughput delivery of biomolecules into cells. *Nat Methods* **5**, 393-395, doi:Doi 10.1038/Nmeth.1201 (2008).

38 Judge, A. D. *et al.* Sequence-dependent stimulation of the mammalian innate immune response by synthetic siRNA. *Nat Biotechnol* **23**, 457-462, doi:Doi 10.1038/Nbt1081 (2005).

39 Novina, C. D. *et al.* siRNA-directed inhibition of HIV-1 infection. *Nat Med* **8**, 681-686, doi:Doi 10.1038/Nm725 (2002).

40 Shayakhmetov, D. M., Di Paolo, N. C. & Mossman, K. L. Recognition of Virus Infection and Innate Host Responses to Viral Gene Therapy Vectors. *Mol Ther* **18**, 1422-1429, doi:Doi 10.1038/Mt.2010.124 (2010).

41 Akil, H. *et al.* Medicine. The future of psychiatric research: genomes and neural circuits. *Science* **327**, 1580-1581, doi:10.1126/science.1188654 (2010).

42 Bock, D. D. *et al.* Network anatomy and in vivo physiology of visual cortical neurons. *Nature* **471**, 177-182 (2011).

43 Yizhar, O. *et al.* Neocortical excitation/inhibition balance in information processing and social dysfunction. *Nature* **477**, 171-178, doi:10.1038/nature10360 (2011).

44 Peterka, D. S., Takahashi, H. & Yuste, R. Imaging Voltage in Neurons. *Neuron* **69**, 9-21 (2011).

45 Kralj, J. M., Hochbaum, D. R., Douglass, A. D. & Cohen, A. E. Electrical spiking in Escherichia coli probed with a fluorescent voltage-indicating protein. *Science* **333**, 345-348, doi:10.1126/science.1204763 (2011).

46 Cohen, A. E. & Venkatachalam, V. Bringing bioelectricity to light. *Annual review of biophysics* **43**, 211-232, doi:10.1146/annurev-biophys-051013-022717 (2014).

47 Hochbaum, D. R. *et al.* All-optical electrophysiology in mammalian neurons using engineered microbial rhodopsins. *Nat Methods* **11**, 825-833, doi:10.1038/nmeth.3000 (2014).

48 Hou, J. H., Venkatachalam, V. & Cohen, A. E. Temporal dynamics of microbial rhodopsin fluorescence reports absolute membrane voltage. *Biophysical journal* **106**, 639-648, doi:10.1016/j.bpj.2013.11.4493 (2014).

49 Zou, P. *et al.* Bright and fast multicoloured voltage reporters via electrochromic FRET. *Nature communications* **5**, 4625, doi:10.1038/ncomms5625 (2014).

50 Zhang, F. *et al.* Optogenetic interrogation of neural circuits: technology for probing mammalian brain structures. *Nature Protocols* **5**, 439-456 (2010).

51 Helmstaedter, M., Briggman, K. L. & Denk, W. 3D structural imaging of the brain with photons and electrons. *Current opinion in neurobiology* **18**, 633-641, doi:10.1016/j.conb.2009.03.005 (2008).

52 Jain, V., Seung, H. S. & Turaga, S. C. Machines that learn to segment images: a crucial technology for connectomics. *Current opinion in neurobiology* **20**, 653-666, doi:Doi 10.1016/J.Conb.2010.07.004 (2010).

53 Richardson, J. J., Bjornmalm, M. & Caruso, F. Multilayer assembly. Technology-driven layer-by-layer assembly of nanofilms. *Science* **348**, aaa2491, doi:10.1126/science.aaa2491 (2015).

54 Hayworth, K. J. *et al.* Imaging ATUM ultrathin section libraries with WaferMapper: a multi-scale approach to EM reconstruction of neural circuits. *Frontiers in neural circuits* **8**, 68, doi:10.3389/fncir.2014.00068 (2014).

55 Cai, D., Cohen, K. B., Luo, T., Lichtman, J. W. & Sanes, J. R. Improved tools for the Brainbow toolbox. *Nat Methods* **10**, 540-547 (2013).

56 Lichtman, J. W., Livet, J. & Sanes, J. R. A technicolour approach to the connectome. *Nature reviews. Neuroscience* **9**, 417-422, doi:10.1038/nrn2391 (2008).

57 Tian, L. *et al.* Imaging neural activity in worms, flies and mice with improved GCaMP calcium indicators. *Nat Methods* **6**, 875-881, doi:10.1038/nmeth.1398 (2009).

58 Ghosh, K. K. *et al.* Miniaturized integration of a fluorescence microscope. *Nat Methods* **8**, 871-878, doi:10.1038/nmeth.1694 (2011).

59 Wilt, B. A. *et al.* Advances in light microscopy for neuroscience. *Annual review of neuroscience* **32**, 435-506, doi:10.1146/annurev.neuro.051508.135540 (2009).

60 Molleman, A. *Patch clamping*. (John Wiley and Sons, 2003).

61 Hebb, D. O., Martinez, J. L. & Glickman, S. E. The Organization of Behavior - a Neuropsychological Theory - Hebb,Do. *Contemp Psychol* **39**, 1018-1020 (1994).

62 Bliss, T. V. P. & Collingridge, G. L. A Synaptic Model of Memory - Long-Term Potentiation in the Hippocampus. *Nature* **361**, 31-39, doi:Doi 10.1038/361031a0 (1993).

63 Hamill, O. P., Marty, A., Neher, E., Sakmann, B. & Sigworth, F. J. Improved Patch-Clamp Techniques for High-Resolution Current Recording from Cells and Cell-Free Membrane Patches. *Pflug Arch Eur J Phy* **391**, 85-100, doi:Doi 10.1007/Bf00656997 (1981).

64 Pine, J. in *Advances in Network Electrophysiology* 3-23 (2006).

65 Rolston, J. D., Gross, R. E. & Potter, S. M. A low-cost multielectrode system for data acquisition enabling real-time closed-loop processing with rapid recovery from stimulation artifacts. *Frontiers in Neuroengineering* **2**, 12-12 (2009).

66 Sigworth, F. J. & Klemic, K. G. Microchip technology in ion-channel research. *IEEE Transactions on Nanobioscience* **4**, 121-127 (2005).

67 Lau, A. Y., Hung, P. J., Wu, A. R. & Lee, L. P. Open-access microfluidic patch-clamp array with raised lateral cell trapping sites. *Lab on a Chip* **6**, 1510-1515 (2006).

68 Li, X., Klemic, K. G., Reed, M. A. & Sigworth, F. J. Microfluidic System for Planar Patch Clamp Electrode Arrays. *Nano Lett* **6**, 815-819 (2006).

69 Anastassiou, C. A., Montgomery, S. M., Barahona, M., Buzsaki, G. & Koch, C. The Effect of Spatially Inhomogeneous Extracellular Electric Fields on Neurons. *J Neurosci* **30**, 1925-1936, doi:Doi 10.1523/Jneurosci.3635-09.2010 (2010).

70 Voelker, M. & Fromherz, P. Signal transmission from individual mammalian nerve cell to field-effect transistor. *Small* **1**, 206-210, doi:10.1002/smll.200400077 (2005).

71 Patolsky, F. *et al.* Detection, Stimulation, and Inhibition of Neuronal Signals with High-Density Nanowire Transistor Arrays. *Science* **313**, 1100-1104 (2006).

72 Duan, X. J. *et al.* Intracellular recordings of action potentials by an extracellular nanoscale field-effect transistor. *Nature nanotechnology* **7**, 174-179, doi:Doi 10.1038/Nnano.2011.223 (2012).

73 Gao, R. *et al.* Outside looking in: nanotube transistor intracellular sensors. *Nano letters* **12**, 3329-3333, doi:10.1021/nl301623p (2012).

74 Yuste, R. Circuit Neuroscience: The Road Ahead. *Frontiers in Neuroscience* **2**, 6-9 (2008).

75 Hai, A., Shappir, J. & Spira, M. E. In-cell recordings by extracellular microelectrodes. *Nat Meth* **7**, 200-202 (2010).

76 Hai, A., Shappir, J. & Spira, M. E. Long-Term, Multisite, Parallel, In-Cell Recording and Stimulation by an Array of Extracellular Microelectrodes. *J Neurophysiol* **104**, 559-568 (2010).

77 Fendyur, A. & Spira, M. E. Toward on-chip, in-cell recordings from cultured cardiomyocytes by arrays of gold mushroom-shaped microelectrodes. *Front Neuroeng* **5**, 21, doi:10.3389/fneng.2012.00021 (2012).

78 Chen, X., Kis, A., Zettl, A. & Bertozzi, C. R. A cell nanoinjector based on carbon nanotubes. *P Natl Acad Sci USA* **104**, 8218-8222, doi:DOI 10.1073/pnas.0700567104 (2007).

79 Kay, M. A., Glorioso, J. C. & Naldini, L. Viral vectors for gene therapy: the art of turning infectious agents into vehicles of therapeutics. *Nat Med* **7**, 33-40, doi:10.1038/83324 (2001).

80 McNaughton, B. R., Cronican, J. J., Thompson, D. B. & Liu, D. R. Mammalian cell penetration, siRNA transfection, and DNA transfection by supercharged proteins. *Proc Natl Acad Sci U S A* **106**, 6111-6116, doi:10.1073/pnas.0807883106 (2009).

81 Wadia, J. S. & Dowdy, S. F. Protein transduction technology. *Curr Opin Biotechnol* **13**, 52-56 (2002).

82 Sokolova, V. & Epple, M. Inorganic nanoparticles as carriers of nucleic acids into cells. *Angew Chem Int Edit* **47**, 1382-1395, doi:DOI 10.1002/anie.200703039 (2008).

83 Whitehead, K. A., Langer, R. & Anderson, D. G. Knocking down barriers: advances in siRNA delivery. *Nat Rev Drug Discov* **8**, 129-138, doi:10.1038/nrd2742 (2009).

84 Kim, W., Ng, J. K., Kunitake, M. E., Conklin, B. R. & Yang, P. Interfacing Silicon Nanowires with Mammalian Cells. *Journal of the American Chemical Society* **129**, 7228-7229 (2007).

85 Hallstrom, W. *et al.* Gallium phosphide nanowires as a substrate for cultured neurons. *Nano Lett* **7**, 2960-2965, doi:10.1021/nl070728e (2007).

86 Jiang, K. *et al.* Medicinal surface modification of silicon nanowires: impact on calcification and stromal cell proliferation. *ACS Appl Mater Interfaces* **1**, 266-269, doi:10.1021/am800219r (2009).

87 Qi, S., Yi, C., Ji, S., Fong, C. C. & Yang, M. Cell adhesion and spreading behavior on vertically aligned silicon nanowire arrays. *ACS Appl Mater Interfaces* **1**, 30-34, doi:10.1021/am800027d (2009).

88 Turner, A. M. *et al.* Attachment of astroglial cells to microfabricated pillar arrays of different geometries. *J Biomed Mater Res* **51**, 430-441 (2000).

89 Shalek, A. K. *et al.* Vertical silicon nanowires as a universal platform for delivering biomolecules into living cells. *Proceedings of the National Academy of Sciences* **107**, 1870-1875 (2010).

90 Shalek, A. K. *et al.* Vertical silicon nanowires as a universal platform for delivering biomolecules into living cells. *Proc Natl Acad Sci U S A* **107**, 1870-1875, doi:10.1073/pnas.0909350107 (2010).

91 Chevrier, N. *et al.* Systematic discovery of TLR signaling components delineates viral-sensing circuits. *Cell* **147**, 853-867, doi:10.1016/j.cell.2011.10.022 (2011).

92 Shalek, A. K. *et al.* Nanowire-mediated delivery enables functional interrogation of primary immune cells: application to the analysis of chronic lymphocytic leukemia. *Nano Lett* **12**, 6498-6504, doi:10.1021/nl3042917 (2012).

93 Wang, L. *et al.* Somatic mutation as a mechanism of Wnt/beta-catenin pathway activation in CLL. *Blood* **124**, 1089-1098, doi:10.1182/blood-2014-01-552067 (2014).

94 Yosef, N. *et al.* Dynamic regulatory network controlling TH17 cell differentiation. *Nature* **496**, 461-468, doi:10.1038/nature11981 (2013).

95 Na, Y. R. *et al.* Probing Enzymatic Activity inside Living Cells Using a Nanowire-Cell "Sandwich" Assay. *Nano Lett* **13**, 153-158, doi:DOI 10.1021/nl3037068 (2013).

96 Yosef, N. *et al.* Dynamic regulatory network controlling Th17 cell differentiation *Nature, accepted* (2013).

97 Zhu, J., Yamane, H. & Paul, W. E. Differentiation of Effector CD4 T Cell Populations *. *Annu. Rev. Immunol.* **28**, 445-489, doi:10.1146/annurev-immunol-030409-101212 (2010).

98 Bettelli, E. *et al.* Reciprocal developmental pathways for the generation of pathogenic effector TH17 and regulatory T cells. *Nature* **441**, 235-238 (2006).

99 Dardalhon, V. *et al.* Lentivirus-mediated gene transfer in primary T cells is enhanced by a central DNA flap. *Gene therapy* **8**, 190-198 (2001).

100 McManus, M. *et al.* Small interfering RNA-mediated gene silencing in T lymphocytes. *The Journal of Immunology* **169**, 5754 (2002).

101 Jones, S. A., Shim, S. H., He, J. & Zhuang, X. W. Fast, three-dimensional super-resolution imaging of live cells. *Nat Methods* **8**, 499-U496, doi:Doi 10.1038/Nmeth.1605 (2011).

102 Dankerl, M. *et al.* Diamond Transistor Array for Extracellular Recording From Electrogenic Cells. *Adv Funct Mater* **19**, 2915-2923, doi:DOI 10.1002/adfm.200900590 (2009).

103 Grotz, B. *et al.* Charge state manipulation of qubits in diamond. *Nature Communications* **3**, doi:ARTN 729 DOI 10.1038/ncomms1729 (2012).

104 Dankerl, M. *et al.* Hydrophobic Interaction and Charge Accumulation at the Diamond-Electrolyte Interface. *Physical Review Letters* **106**, doi:ARTN 196103 DOI 10.1103/PhysRevLett.106.196103 (2011).

105 Chakrapani, V. *et al.* Charge transfer equilibria between diamond and an aqueous oxygen electrochemical redox couple. *Science* **318**, 1424-1430, doi:DOI 10.1126/science.1148841 (2007).

106 Dolde, F. *et al.* Electric-field sensing using single diamond spins. *Nat Phys* **7**, 459-463, doi:Doi 10.1038/Nphys1969 (2011).

107 Schreyvogel, C., Wolfer, M., Kato, H., Schreck, M. & Nebel, C. E. Tuned NV emission by in-plane Al-Schottky junctions on hydrogen terminated diamond. *Sci Rep-Uk* **4**, doi:ARTN 3634 DOI 10.1038/srep03634 (2014).

108 Han, K. Y., Kim, S. K., Eggeling, C. & Hell, S. W. Metastable Dark States Enable Ground State Depletion Microscopy of Nitrogen Vacancy Centers in Diamond with Diffraction-Unlimited Resolution. *Nano Lett* **10**, 3199-3203, doi:DOI 10.1021/nl102156m (2010).

109 Voelker, M. & Fromherz, P. Signal Transmission from Individual Mammalian Nerve Cell to Field-Effect Transistor. *Small* **1**, 206-210 (2005).

110 Viventi, J. *et al.* A Conformal, Bio-Interfaced Class of Silicon Electronics for Mapping Cardiac Electrophysiology. *Science Translational Medicine* **2**, 24ra22-24ra22 (2010).

111 Eschermann, J. F. *et al.* Action potentials of HL-1 cells recorded with silicon nanowire transistors. *Appl Phys Lett* **95**, 083703-083703 (2009).

112 Wang, K., Fishman, H. A., Dai, H. & Harris, J. S. Neural Stimulation with a Carbon Nanotube Microelectrode Array. *Nano Lett* **6**, 2043-2048 (2006).

113 McKnight, T. E. *et al.* Resident Neuroelectrochemical Interfacing Using Carbon Nanofiber Arrays. *The Journal of Physical Chemistry B* **110**, 15317-15327 (2006).

114 Spira, M. E. & Hai, A. Multi-electrode array technologies for neuroscience and cardiology. *Nature Nanotechnology* **8**, 83-94, doi:10.1038/nnano.2012.265 (2013).

115 Nikolenko, V., Poskanzer, K. E. & Yuste, R. Two-photon photostimulation and imaging of neural circuits. *Nat Meth* **4**, 943-950 (2007).

116 Thomas, P. & Smart, T. G. HEK293 cell line: A vehicle for the expression of recombinant proteins. *Journal of Pharmacological and Toxicological Methods* **51**, 187-200 (2005).

117 Rols, M. P. & TeissiÃ©, J. Electropermeabilization of mammalian cells. Quantitative analysis of the phenomenon. *Biophysical Journal* **58**, 1089-1098 (1990).

118 Moulton. Studies of double layer capacitance and electron transfer at a gold electrode exposed to protein solutions. *Electrochimica Acta* **49**, 4223-4230 (2004).

119 Dichter, M. A. Rat cortical neurons in cell culture: culture methods, cell morphology, electrophysiology, and synapse formation. *Brain Research* **149**, 279-293 (1978).

120 Romijn, H. J., Mud, M. T., Habets, A. M. & Wolters, P. S. A quantitative electron microscopic study on synapse formation in dissociated fetal rat cerebral cortex in vitro. *Brain Research* **227**, 591-605 (1981).

121 Kole, M. H. P. & Stuart, G. J. Is action potential threshold lowest in the axon? *Nat Neurosci* **11**, 1253-1255 (2008).

122 Dan, Y. & Poo, M.-M. Spike Timing-Dependent Plasticity: From Synapse to Perception. *Physiological Reviews* **86**, 1033-1048 (2006).

123 Mason, A., Nicoll, A. & Stratford, K. Synaptic transmission between individual pyramidal neurons of the rat visual cortex in vitro. *The Journal of Neuroscience* **11**, 72-84 (1991).

124 Carmena, J. M. *et al.* Learning to control a brain-machine interface for reaching and grasping by primates. *PLoS biology* **1**, E42, doi:10.1371/journal.pbio.0000042 (2003).

125 Erickson, J., Tooker, A., Tai, Y. C. & Pine, J. Caged neuron MEA: A system for long-term investigation of cultured neural network connectivity. *Journal of Neuroscience Methods* **175**, 1-16 (2008).

126 Arancio, O., Kandel, E. R. & Hawkins, R. D. Activity-dependent long-term enhancement of transmitter release by presynaptic 3[prime],5[prime]-cyclic GMP in cultured hippocampal neurons. *Nature* **376**, 74-80 (1995).

127 Robinson, J. T. *et al.* Vertical nanowire electrode arrays as a scalable platform for intracellular interfacing to neuronal circuits. *Nature Nanotechnology* **7**, 180-184, doi:Doi 10.1038/Nnano.2011.249 (2012).

128 Eversmann, B. *et al.* A 128 × 128 CMOS biosensor array for extracellular recording of neural activity. *Ieee J Solid-St Circ* **38**, 2306-2317 (2003).

129 Hutzler, M. *et al.* High-resolution multitransistor array recording of electrical field potentials in cultured brain slices. *J Neurophysiol* **96**, 1638-1645, doi:10.1152/jn.00347.2006 (2006).

130 Frey, U., Egert, U., Heer, F., Hafizovic, S. & Hierlemann, A. Microelectronic system for high-resolution mapping of extracellular electric fields applied to brain slices. *Biosens Bioelectron* **24**, 2191-2198, doi:10.1016/j.bios.2008.11.028 (2009).

131 Nam, Y. & Wheeler, B. C. In vitro microelectrode array technology and neural recordings. *Crit Rev Biomed Eng* **39**, 45-61 (2011).

132 Huys, R. *et al.* Single-cell recording and stimulation with a 16k micro-nail electrode array integrated on a 0.18 mum CMOS chip. *Lab Chip* **12**, 1274-1280, doi:10.1039/c2lc21037a (2012).

133 Berdondini, L. *et al.* Active pixel sensor array for high spatio-temporal resolution electrophysiological recordings from single cell to large scale neuronal networks. *Lab Chip* **9**, 2644-2651, doi:10.1039/b907394a (2009).

134 Berdondini, L. *et al.* Extracellular recordings from locally dense microelectrode arrays coupled to dissociated cortical cultures. *J Neurosci Methods* **177**, 386-396, doi:10.1016/j.jneumeth.2008.10.032 (2009).

135 Robinson, J. T., Jorgolli, M. & Park, H. Nanowire electrodes for high-density stimulation and measurement of neural circuits. *Front Neural Circuit* **7**, doi:ARTN 38 DOI 10.3389/fncir.2013.00038 (2013).

136 Lei, N. *et al.* High-resolution extracellular stimulation of dispersed hippocampal culture with high-density CMOS multielectrode array based on non-Faradaic electrodes. *J Neural Eng* **8**, 044003, doi:10.1088/1741-2560/8/4/044003 (2011).

137 Imfeld, K. *et al.* Large-scale, high-resolution data acquisition system for extracellular recording of electrophysiological activity. *IEEE Trans Biomed Eng* **55**, 2064-2073, doi:10.1109/TBME.2008.919139 (2008).

138 Franks, W., Schenker, I., Schmutz, P. & Hierlemann, A. Impedance characterization and modeling of electrodes for biomedical applications. *IEEE Trans Biomed Eng* **52**, 1295-1302, doi:10.1109/TBME.2005.847523 (2005).

139 Nyquist, H. Thermal agitation of electric charge in conductors. *Phys Rev* **32**, 110-113, doi:DOI 10.1103/PhysRev.32.110 (1928).

140 Lin, Z. C., Xie, C., Osakada, Y., Cui, Y. & Cui, B. Iridium oxide nanotube electrodes for sensitive and prolonged intracellular measurement of action potentials. *Nat Commun* **5**, 3206, doi:10.1038/ncomms4206 (2014).

141 Bliss, T. V. & Collingridge, G. L. A synaptic model of memory: long-term potentiation in the hippocampus. *Nature* **361**, 31-39 (1993).

142 Malenka, R. C. & Nicoll, R. A. Long-term potentiation--a decade of progress? *Science (New York, N.Y.)* **285**, 1870-1874 (1999).

143 Milo, R. *et al.* Network Motifs: Simple Building Blocks of Complex Networks. *Science* **298**, 824-827 (2002).

144 Prill, R. J., Iglesias, P. A. & Levchenko, A. Dynamic Properties of Network Motifs Contribute to Biological Network Organization. *PLoS Biol* **3**, e343-e343 (2005).

145 Kashtan, N. & Alon, U. Spontaneous evolution of modularity and network motifs. *P Natl Acad Sci USA* **102**, 13773-13778 (2005).

146 Bi, G.-q. & Poo, M.-m. Distributed synaptic modification in neural networks induced by patterned stimulation. *Nature* **401**, 792-796 (1999).

147 Wise, R. A. Dopamine, learning and motivation. *Nat Rev Neurosci* **5**, 483-494 (2004).

148 Chklovskii, D. B. & Koulakov, A. A. MAPS IN THE BRAIN: What Can We Learn from Them? *Annual Review of Neuroscience* **27**, 369-392 (2004).

149 Dunlop, J., Bowlby, M., Peri, R., Vasilyev, D. & Arias, R. High-throughput electrophysiology: an emerging paradigm for ion-channel screening and physiology. *Nat Rev Drug Discov* **7**, 358-368, doi:10.1038/nrd2552 (2008).

150 Dunlop, J. *et al.* Ion channel screening. *Comb Chem High Throughput Screen* **11**, 514-522 (2008).

151 Dunlop, J., Peri, R., Terstappen, G. C. & Bowlby, M. Functional screening of alpha7 nicotinic receptor ligands. *Expert Opin Drug Discov* **3**, 623-628, doi:10.1517/17460441.3.6.623 (2008).

152 Quik, M. & Wonnacott, S. alpha6beta2* and alpha4beta2* nicotinic acetylcholine receptors as drug targets for Parkinson's disease. *Pharmacol Rev* **63**, 938-966, doi:10.1124/pr.110.003269 (2011).

153 Bagetta, V., Ghiglieri, V., Sgobio, C., Calabresi, P. & Picconi, B. Synaptic dysfunction in Parkinson's disease. *Biochem Soc Trans* **38**, 493-497, doi:10.1042/BST0380493 (2010).

154 Kreitzer, A. C. & Malenka, R. C. Endocannabinoid-mediated rescue of striatal LTD and motor deficits in Parkinson's disease models. *Nature* **445**, 643-647, doi:10.1038/nature05506 (2007).

155 Ahmed, I. *et al.* Glutamate NMDA receptor dysregulation in Parkinson's disease with dyskinesias. *Brain* **134**, 979-986, doi:10.1093/brain/awr028 (2011).

156 Cooper, O. *et al.* Pharmacological rescue of mitochondrial deficits in iPSC-derived neural cells from patients with familial Parkinson's disease. *Sci Transl Med* **4**, 141ra190, doi:10.1126/scitranslmed.3003985 (2012).

157 Arden, W. M. The International Technology Roadmap for Semiconductors - Perspectives and challenges for the next 15 years. *Current Opinion in Solid State & Materials Science* **6**, 371-377 (2002).

158 Tian, B. & Lieber, C. M. Synthetic Nanoelectronic Probes for Biological Cells and Tissues. *Annual Review of Analytical Chemistry* **6**, 31-51, doi:doi:10.1146/annurev-anchem-062012-092623 (2013).

159 Robinson, J. T., Jorgolli, M. & Park, H. Nanowire electrodes for high-density stimulation and measurement of neural circuits. *Frontiers in neural circuits* **7**, 38, doi:10.3389/fncir.2013.00038 (2013).

160 Cummins, T. R., Rush, A. M., Estacion, M., Dib-Hajj, S. D. & Waxman, S. G. Voltage-clamp and current-clamp recordings from mammalian DRG neurons. *Nature Protocols* **4**, 1103-1112, doi:10.1038/nprot.2009.91 (2009).

161 Hamill, O. P., Marty, A., Neher, E., Sakmann, B. & Sigworth, F. J. Improved patch-clamp techniques for high-resolution current recording from cells and cell-free membrane patches. *Pflügers Archiv European Journal of Physiology* **391**, 85-100 (1981).

162 Fenno, L., Yizhar, O. & Deisseroth, K. The development and application of optogenetics. *Annual review of neuroscience* **34**, 389-412, doi:10.1146/annurev-neuro-061010-113817 (2011).

163 Arikkath, J. & Reichardt, L. F. Cadherins and catenins at synapses: roles in synaptogenesis and synaptic plasticity. *Trends in neurosciences* **31**, 487-494, doi:10.1016/j.tins.2008.07.001 (2008).

164 Bagetta, G. *et al.* Neuropharmacology of the essential oil of bergamot. *Fitoterapia* **81**, 453-461, doi:10.1016/j.fitote.2010.01.013 (2010).

165 Beaudoin, G. M., 3rd *et al.* Culturing pyramidal neurons from the early postnatal mouse hippocampus and cortex. *Nature Protocols* **7**, 1741-1754, doi:10.1038/nprot.2012.099 (2012).

166 Kaech, S. & Banker, G. Culturing hippocampal neurons. *Nature Protocols* **1**, 2406-2415, doi:10.1038/nprot.2006.356 (2006).

167 Meberg, P. J. & Miller, M. W. Culturing hippocampal and cortical neurons. *Methods Cell Biol* **71**, 111-127 (2003).